PLASMONIC PROPERTIES OF GOLD AND SILVER NANOCRESCENTS FOR SURFACE ENHANCED SPECTROSCOPY APPLICATIONS

by

Cindy Taylor Cooper

A dissertation submitted to the faculty of
The University of Utah
in partial fulfillment of the requirements for the degree of

Doctor of Philosophy

Department of Chemistry

The University of Utah

December 2014

The University of Utah Graduate School

STATEMENT OF DISSERTATION APPROVAL

The dissertation of **Cindy Taylor Cooper**

has been approved by the following supervisory committee members:

Jennifer S. Shumaker-Parry	, Chair	**12/20/2013** Date Approved
Joel M. Harris	, Member	**12/20/2013** Date Approved
Marc D. Porter	, Member	**12/20/2013** Date Approved
Scott L. Anderson	, Member	**12/20/2013** Date Approved
Jordan M. Gerton	, Member	**12/20/2013** Date Approved

and by **Cynthia J. Burrows**, Chair of

the Department of **Chemistry**

and by David B. Kieda, Dean of The Graduate School.

ABSTRACT

The unique plasmonic properties of noble metal nanocrescents were investigated using optical spectroscopy techniques and correlated with tunable structural features. Multiple characteristics were observed that offer advantages for increased sensitivity and spatial resolution in common analytical methods which make the plasmonic nanocrescent an ideal surface enhancing substrate for a broad range of spectroscopy and microscopy techniques.

The localized surface plasmon resonance (LSPR) wavelengths of nanocrescents are highly tunable due to the asymmetry of the structure and versatility of the nanosphere template lithography fabrication technique. This method allows for simple procedural modifications which can be used to alter the physical structure and resulting plasmonic properties. For example, template organization led to nanocrescent arrays which exhibited previously unobserved plasmon resonance modes.

Four distinct polarization-dependent plasmon resonance modes were predicted for the nanocrescent using finite-difference time-domain calculations. The polarization anisotropy of the four modes was confirmed through experiments and each mode was selectively induced at a specific LSPR wavelength, indicating the possibility of enhancing spectroscopy signals within a targeted wavelength range using a simple manipulation of the incident radiation. This means that a single nanocrescent can be used to enhance the detection of infrared molecular vibrations or couple with the visible

excitation of a fluorescent molecule.

Two additional polarization-dependent modes were observed for aggregated and nonuniform structures. Aggregated template fabrication produced nanocrescent dimers, resulting in elongated nanocrescent structures with a low-energy resonance mode. The second unpredicted mode was observed at the visible/near-infrared boundary and was attributed to the distortion of structures fabricated from less spherical templates.

Adjustments to the fabrication procedure also allowed for extension of the predicted optical behavior into the mid-infrared spectral range. This property broadens the spectral tunability of the nanocrescent as well as the number of potential applications.

When combined, the high tunability, multimodality, polarization dependence, and persistence of plasmonic behavior into the mid-infrared make the nanocrescent a highly desirable substrate that can be used in numerous spectroscopy and microscopy techniques. Preliminary experiments for the incorporation of nanocrescents in nonlinear spectroscopy and microscopy applications are described and support the conclusion of a broadly applicable surface enhancing substrate.

For Justin, who has always believed in me more than I believed in myself.

“I wasn’t there for the weeds.”

~Henry Eyring

TABLE OF CONTENTS

ABSTRACT iii

LIST OF FIGURES ix

LIST OF TABLES xi

ACKNOWLEDGMENTS xii

Chapter Page

1 INTRODUCTION 1

1.1 Localized Surface Plasmon Resonance 1
1.2 Asymmetric Plasmonic Nanocrescent Fabrication 7
1.3 Polarization-Dependent Plasmon Resonance Modes 10
1.4 Nanocrescent Organization Effects on Plasmon Resonance Modes 11
1.5 Mid-IR Plasmon Resonance Modes 12
1.6 Plasmonic Nanocrescents as Surface-Enhanced Spectroscopy Substrates 13
1.7 References 15

2 ORGANIZATION AND FABRICATION OF NANOCRESCENTS USING A MODIFIED NANOSPHERE TEMPLATE LITHOGRAPHY PROCEDURE AND METHODS FOR CHARACTERIZATION OF THEIR OPTICAL AND STRUCTURAL PROPERTIES 18

2.1 Introduction 18
2.2 Experimental Procedures 19
2.3 Results and Discussion 28
2.4 Conclusion 31
2.5 References 32

3 POLARIZATION ANISOTROPY OF MULTIPLE LOCALIZED PLASMON RESONANCE MODES IN NOBLE METAL NANOCRESCENTS 34

3.1 Introduction 34
3.2 Experimental Procedures 36
3.3 Results and Discussion 38
3.4 Conclusion 53

3.5 References 54

4 OPTICAL PROPERTIES OF PLASMONIC NANOCRESCENT ARRAYS FABRICATED BY CONTROLLED PLASMA ETCHING OF POLYSTYRENE NANOSPHERE TEMPLATES 57

4.1 Introduction 57
4.2 Experimental Procedures and Discussion 59
4.3 Results and Discussion 70
4.4 Conclusion 80
4.5 References 82

5 LOCALIZED SURFACE PLASMON RESONANCES OF GOLD AND SILVER NANOCRESCENTS IN THE INFRARED SPECTRAL RANGE 85

5.1 Introduction 85
5.2 Experimental Procedures 88
5.3 Results and Discussion 89
5.4 Conclusion 101
5.5 References 104

6 CONCLUSION AND FUTURE WORK 108

6.1 Conclusion 108
6.2 Future Work 109

LIST OF FIGURES

1.1 Localized surface plasmon resonance and electric near field enhancement and localization 2

1.2 Tip-enhanced Raman spectroscopy and microscopy utilizing plasmonic effects of near field enhancement and localization 4

1.3 LSPR wavelength dependence on structural size of plasmonic nanocrescents 6

1.4 Comparison of top-down fabrication and bottom-up synthetic techniques for plasmonic nanoparticle production 8

2.1 Schematic of self-assembly of hexagonal close packing of template nanospheres and size reduction via oxygen plasma etching (top) 24

2.2 Schematic of nanosphere template lithography fabrication procedure 25

2.3 Nanocrescents fabricated using nanosphere template lithography with various compositions, sizes, and substrates 29

3.1 Application of plasmonic nanocrescent near field enhancement effects to nonlinear optical techniques 37

3.2 SEM images of 445 nm diameter AuNCs 39

3.3 Calculated and experimental polarized extinction spectra demonstrating selective induction of long and short axis plasmon resonance modes 41

3.4 Calculated near field enhancement, I/I_0, maps for polarization-dependent plasmon resonance modes of 445 nm diameter template AuNC 42

3.5 Selective induction of polarization-dependent plasmon resonance modes over a broad size range 45

3.6 Polarization anisotropy of 445 nm diameter AuNCs 49

3.7 Polarization dependence of nonlinear microscopy imaging techniques utilizing surface enhancement effects of AuNCs 52

4.1 Effects of solvent concentration and dilution factor on self-assembly of hexagonal close packing of polystyrene nanospheres 61

4.2 Schematic of nanosphere template size reduction and array fabrication 63

4.3 SEM images of hexagonally close packed polystyrene nanosphere templates demonstrating similar size (A, B) or interparticle distance (B, C) after oxygen plasma etching 63

4.4 Etch rates of polystyrene nanospheres 65

4.5 Nanosphere deformation resulting from long etch lengths 67

4.6 Comparison of Raman spectra for 3 μm polystyrene nanospheres etched for varying lengths of time 69

4.7 Optical and structural properties of isolated (A/E), aggregated (B/F), and arrayed (C/G, D/H) gold nanocrescents 71

5.1 Experimental design for surface-enhanced sum frequency generation (SFG) spectroscopy 90

5.2 Calculated and experimental extinction spectra of large diameter AuNCs 91

5.3 Unpolarized FTIR extinction spectra of large diameter AuNCs and AgNCs 95

5.4 Relationship of plasmon resonance wavelength and nanocrescent diameter 97

5.5 Extinction spectra and scanning electron microscopy images of large diameter AgNCs and AuNCs 99

5.6 Plasmonic enhancement of mid-infrared sum frequency generation signal 102

LIST OF TABLES

1.1 Comparison of Plasmonic Nanostructure Production Techniques 9

2.1 Sizes and Specifications of Polystyrene Nanosphere Templates.....20

3.1 Theoretical and Experimental Values for Wavelengths of Distinct Plasmon Resonance Modes 46

4.1 Comparison of Isolated and Arrayed AuNC Optical Properties.....77

5.1 LSPR Wavelengths of Long and Short Axis Dipole Resonance Modes of Large Diameter Gold and Silver Nanocrescents 98

ACKNOWLEDGMENTS

First and foremost, I would like to acknowledge my research advisor, Prof. Jennifer Shumaker-Parry for her guidance, understanding, and encouragement. She has been an exceptional mentor for which I am tremendously grateful. I would also like to thank my dissertation committee members, Prof. Joel Harris, Prof. Marc Porter, Prof. Scott Anderson, and Prof. Jordan Gerton, for excellent advice and for being so engaged.

I would also like to acknowledge collaborators who have assisted me in this research: Hiroaki Maekawa and Prof. Nien-Hui Ge at the University of California- Irvine who did the heavy lifting in the nonlinear microscopy and spectroscopy experiments, Miguel Rodriguez and Prof. Steve Blair at the University of Utah for being willing and able to take on a complex simulation task, and Matt DeLong at the University of Utah for exceptional advice and stimulating discussions. A collective recognition should be extended to the large number of people involved in the Chemistry at the Space-Time Limit (CaSTL) Center funded by the National Science Foundation for additional insight and friendship. I am grateful for former and current fellow group members who have also assisted me throughout these investigations. Thank you Rostislav, Cara, Mark, and Cady.

Finally, I would like to thank my family, and especially my husband, for their continued love and support.

CHAPTER 1

INTRODUCTION

1.1 Localized Surface Plasmon Resonance

In order to improve and expand existing optical analytical techniques we need higher sensitivity and spatial resolution with increased control over the manipulation of light on the nanoscale.[1] Our continually advancing ability to overcome the diffraction limit of light, to control and manipulate electromagnetic waves on a nanometer length scale, has led to great advances in spectroscopy and imaging techniques including scanning near-field optical microscopy (SNOM)[2] and surface enhanced Raman and infrared absorption spectroscopies (SERS and SEIRA, respectively),[3-6] but there is still room for improvement. Many of these techniques utilize the field enhancement effects of localized surface plasmon resonances (LSPR). The field of plasmonics merges photonics and electronics, combining the two in such a way that electrons can be controlled with light and electric near fields can be manipulated using far field light sources.

Localized surface plasmon resonance is the coherent oscillation of conduction band electrons induced by electromagnetic radiation.[7] More specifically, LSPR is the perturbation of free electrons at the metal/dielectric interface by the electric field component of light incident on a nanostructure (Fig. 1.1A). In order for LSPR to occur, the dimensions of the structure must be much smaller than the wavelength of incident light and the composition must be metallic (the dielectric constant must possess negative

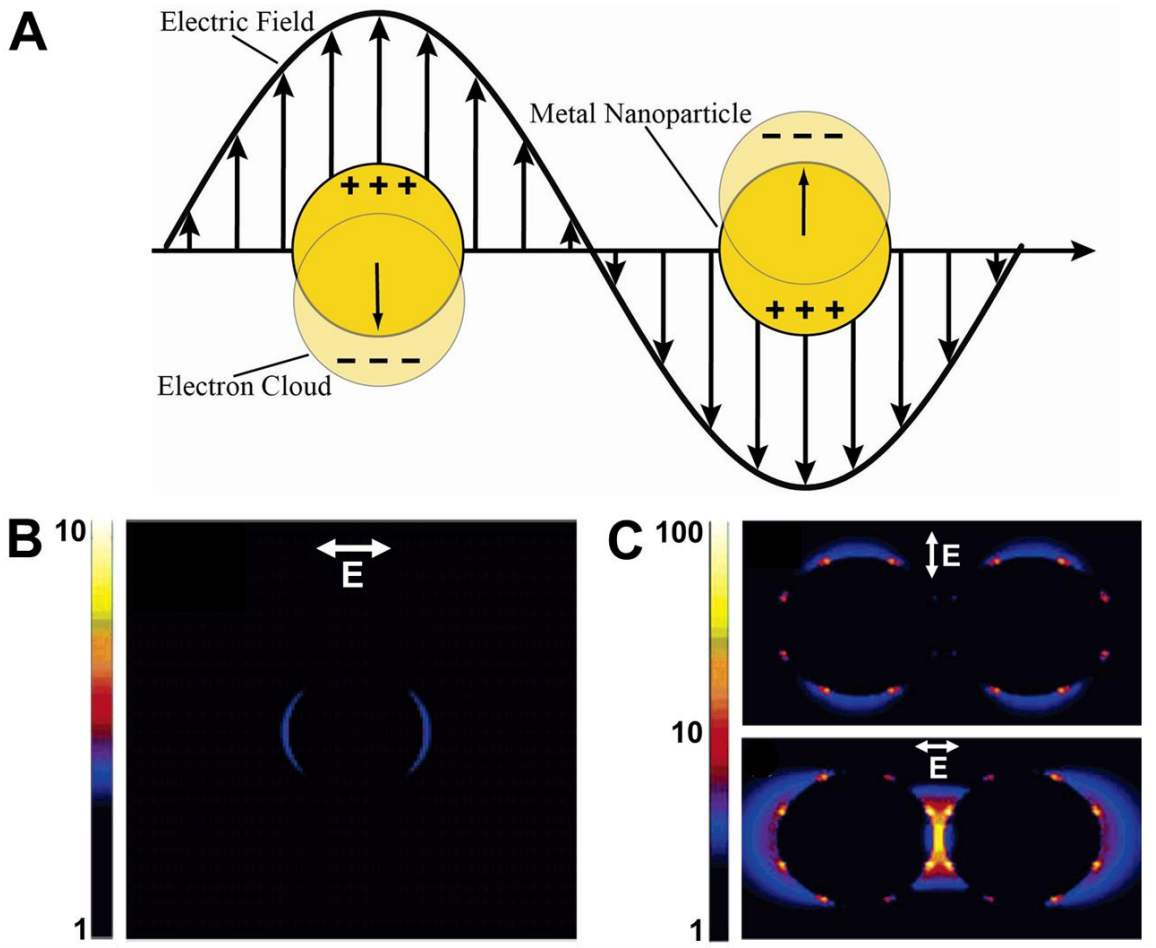

Figure 1.1. Localized surface plasmon resonance and electric near field enhancement and localization. A) Schematic diagram depicting perturbation of surface conduction band electrons within metallic nanoparticles by electric field component of incident light. B, C) Calculated near field enhancement of a single gold nanosphere (B) and gold nanosphere dimers (C) with radii of 30 nm. Polarization of electric field (E) indicated by white arrows. The lower simulation in C illustrates a hot spot localized within the junction of two plasmonic nanoparticles.
Modified from Talley, C. E.; Jackson, J. B.; Oubre, C.; Grady, N. K.; Hollars, C. W.; Lane, S. M.; Huser, T. R.; Nordlander, P.; Halas, N. J.

real and small, positive imaginary components). Because of the oscillating nature of light, the perturbed electrons undergo a collective motion, effectively creating localized areas of separated charge that oscillate as the wave of electromagnetic radiation passes over the nanostructure. These localized areas of high electron density, called "hot spots," result in a super-confinement of free electrons within structural features of nanoscale dimensions and large electric potential differences that effectively focus incident energy from a far field source to nanoscale probe volumes of evanescently decaying electric fields (Fig. 1.1B and C).[8]

LSPR hot spots can be used to increase both the sensitivity and spatial resolution of spectroscopy and microscopy techniques (Fig. 1.2). Signals from analyte molecules located within the small probe volume are intensified, increasing signal to noise ratios and decreasing limits of detection. Plasmonic nanostructures with a variety of shapes have been used to increase signals in surface enhanced Raman, fluorescence, and infrared spectroscopies.[8-12] They have also been utilized as nanofocusing light antennas where the reduction of the probe volume to nanoscale dimensions helps overcome the light diffraction barrier for high spatial resolution in characterization techniques such as tip-enhanced Raman spectroscopy (TERS)[13, 14] and nonlinear laser-induced scanning tunneling microscopy (NLL-STM).[15] In many applications both advantages are utilized where the reduced probe volume pushes the spatial limits of the resolution while the field confinement enhances spectroscopy signals to obtain local chemical information (Fig. 1.2).

The ideal surface enhancing plasmonic substrate for increased sensitivity and spatial resolution is a tunable, high enhancement factor, multimodal plasmonic

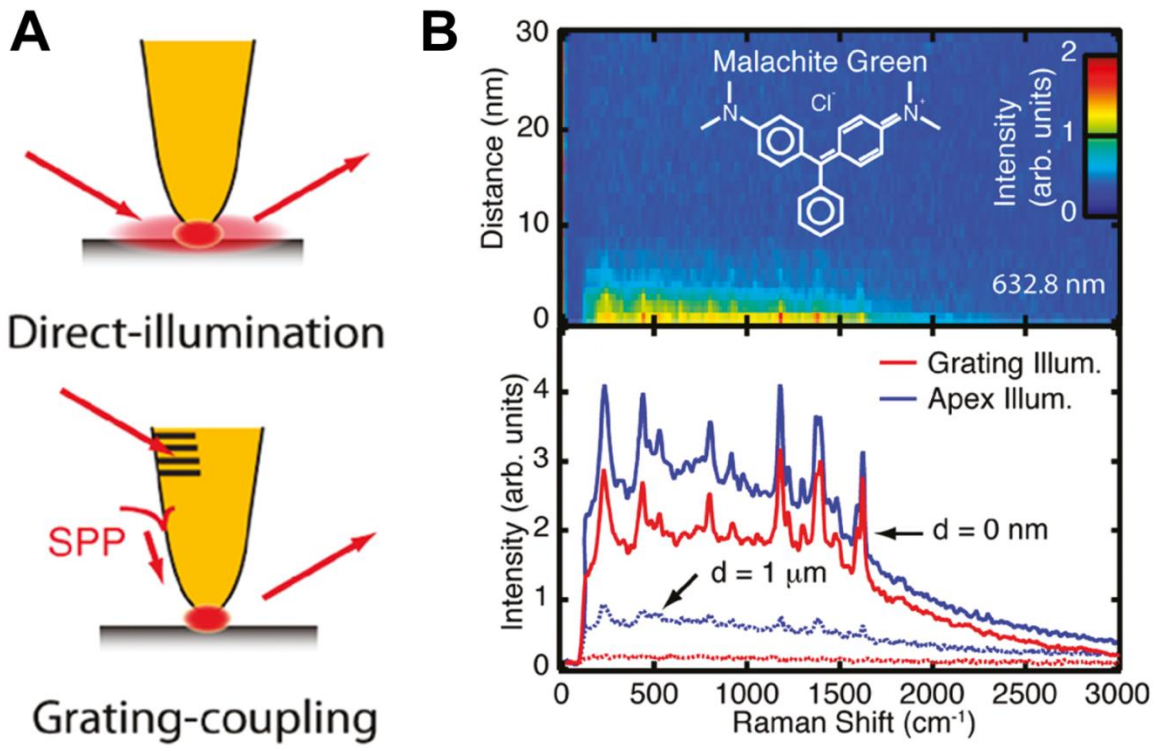

Figure 1.2. Tip-enhanced Raman spectroscopy and microscopy utilizing plasmonic effects of near field enhancement and localization. A) Illustration of direct illumination and grating-coupled tip-enhanced focusing. B) Tip-sample distance dependence of TERS signal of Malachite Green dye molecule on a gold surface with λ_{exc} = 632.8 nm (top). Comparison of TERS spectra with tip in contact with surface (solid line) and retracted by ~1 μm (dotted line) for grating-coupled TERS (red) and direct apex (blue) illumination (bottom). This spectral comparison shows the increased sensitivity (signal to noise ratio) and spatial resolution advantages of plasmonic enhancement.
Modified from Berweger, S.; Atkin, J. M.; Olmon, R. L.; Raschke, M. B.

nanostructure with broad spectral range that can be used in several applications. The ability to tune the LSPR wavelengths of a nanostructure allows for adjustment of the signal enhancement to the spectral region of interest. This can be accomplished by tuning the resonance wavelength of the plasmonic nanoparticle to either the excitation wavelength or a targeted molecular vibration frequency where either the incident intensity or emitted signal is strengthened by the intensified electric near field. The LSPR wavelengths of most plasmonic nanostructures can be tuned by simply adjusting the size of the structure (Fig. 1.3),[16-18] but asymmetric plasmonic nanostructures hold the most promise for application as surface enhancing substrates for a variety of analytical techniques. These structures typically have sharp tips or corners which have demonstrated the highest hot spot enhancement factors and generally support two or more individual plasmon resonance modes that are induced at distinct wavelengths.[1, 19, 20] The distinct plasmon resonance modes result in unique spatial distribution of the enhanced near fields that become more complex as the asymmetry of the structure increases.

The difficulties associated with utilizing plasmonic nanostructures for surface enhancement do not stem from generating the enhanced electric fields, but from controlling them. The reproducibility and structural uniformity of the nanoparticle production method plays a very important role in the amount of control that can be exerted over the electric near field. If the orientation of asymmetric structures is consistent, then the near field distribution can be controlled using basic polarization of incident light.[21] This is a simple way to selectively induce a single plasmon resonance mode at a desired wavelength and control electric near fields with far field manipulation. Polarization-based near field manipulation improves spatial resolution by predictably

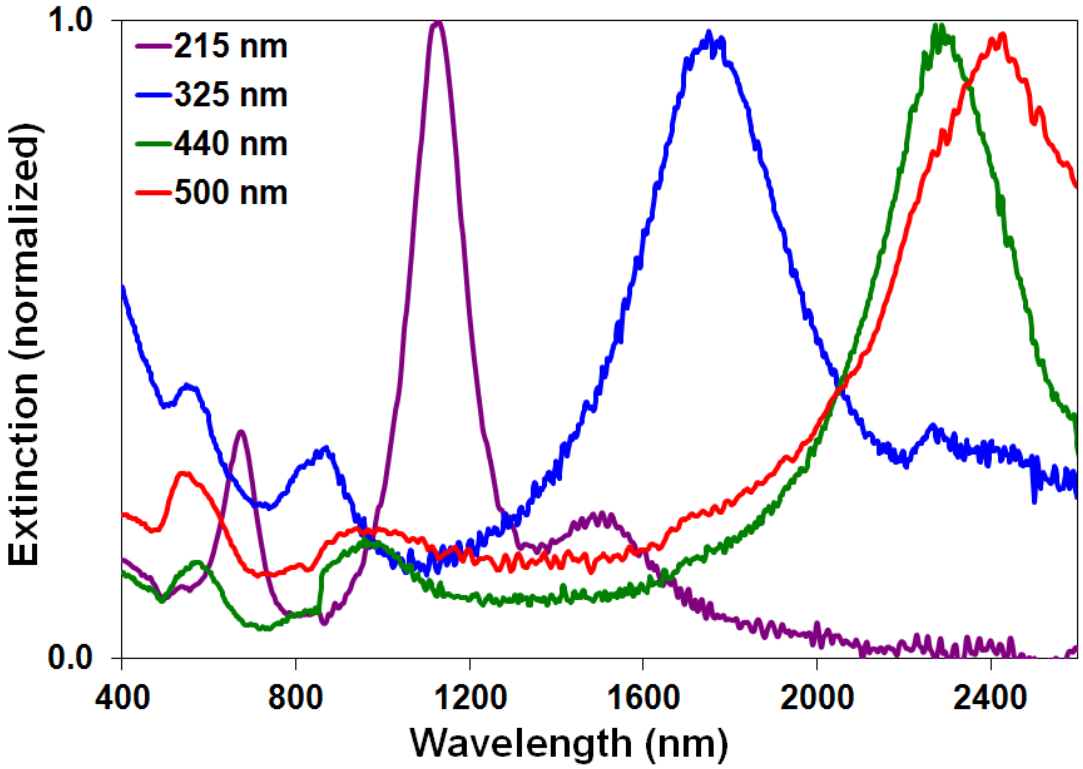

Figure 1.3. LSPR wavelength dependence on structural size of plasmonic nanocrescents. Spectral peaks are red-shifted with increasing diameter (dimensions listed in legend).

controlling probe volumes and also provides a means to determine the physical locations of analytes with respect to plasmonic structures.[22]

1.2 Asymmetric Plasmonic Nanocrescent Fabrication

Plasmonic nanostructures can be produced using several methods that can be separated into synthetic and fabrication techniques. The advantages and disadvantages of the two methodologies are compared in Figure 1.4 and Table 1.1. While synthetic procedures offer high throughput and low cost, they can be time consuming and sensitive to idealized reaction conditions. Certain simple shapes such as nanospheres,[23] nanocubes,[24, 25] and nanorods[26-28] can be made reproducibly while more complex shapes such as nanostars[29] and nanoplates[30, 31] have variable size and structural features. This is unfortunate as these asymmetric and many-edged shapes typically have higher enhancement factors. Fabrication techniques provide a way to produce uniform shapes with consistency and the ability to organize arrays. Top-down techniques such as electron beam lithography can be used to fabricate nearly any imaginable nanostructure, but can be extremely time consuming as well as costly.[32]

Nanosphere template lithography (NTL) combines the advantages of both bottom-up and top-down techniques.[33] This method utilizes individual nanospheres as fabrication templates which increases the output, comparable to synthetic procedures, and maintains the structural uniformity of fabrication methods while decreasing the time requirement and cost. The steps of the simple NTL procedure are template deposition, thin metal film deposition, plasma etch, and template removal. This method was employed to fabricate asymmetric plasmonic nanocrescent (NC) structures over a broad size range (100 nm to 3 μm) from both gold and silver metals on several substrate materials including glass,

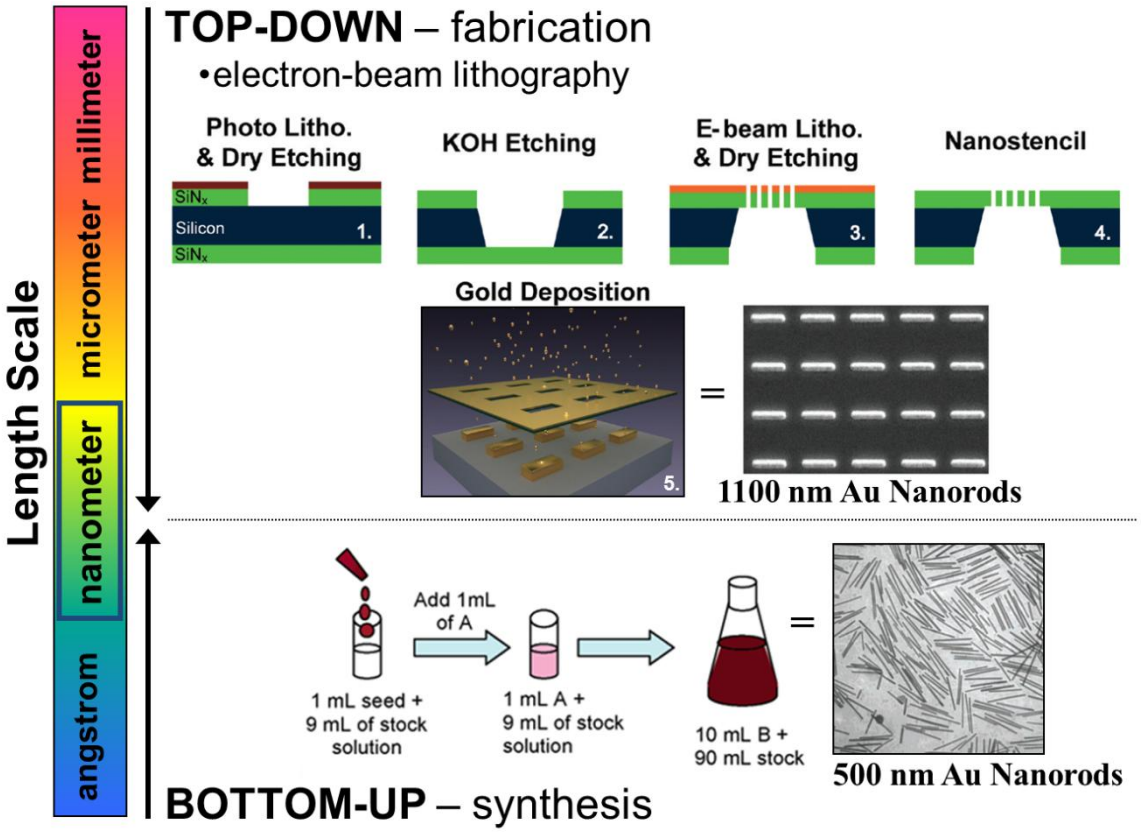

Figure 1.4. Comparison of top-down fabrication and bottom-up synthetic techniques for plasmonic nanoparticle production.
Modified from Aksu, S.; Yanik, A. A.; Adato, R.; Artar, A.; Huang, M.; Altug, H. and from Murphy, C. J.; Sau, T. K.; Gole, A. M.; Orendorff, C. J.; Gao, J.; Gou, L.; Hunyadi, S. E.; Li, T.

Table 1.1. Comparison of Plasmonic Nanostructure Production Techniques

Technique	Advantages	Disadvantages
Fabrication	• Clean surfaces • Variety of materials • Organizational control • Uniformity • Reproducibility	• Expensive • Low throughput • Time consuming • Larger structural dimensions
Synthesis	• Atomic/molecular scale control • Inexpensive • Scalable production • Mimics biological systems	• Limited shapes & sizes • Heterogeneous • Challenging assembly • Prefunctionalized surfaces

silicon, and CaF_2. The nanocrescents fabricated using this technique have similar shape, size, and orientation and their surface density can be controlled through the templating process. Multiple structural features of the nanocrescent including diameter, thickness, backbone width, tip sharpness, and gap angle can also be adjusted during the lithographic process.[34] These physical aspects can be used to tune the wavelength at which LSPR occurs. Further details about the NTL fabrication technique are discussed in Chapter 2.

1.3 Polarization-Dependent Plasmon Resonance Modes

The uniform orientation of the final fabricated nanocrescent structures is very important as it allows for polarization selective induction of specific plasmon resonance modes. Because of their asymmetric structure, plasmonic NCs are multimodal, exhibiting four distinct plasmon resonance modes.[21] Each of the four modes has a unique corresponding near field distribution and occurs over a unique wavelength range. With unpolarized illumination, each plasmon resonance mode can be induced simultaneously at their proper resonance wavelength, over a visible to infrared spectral range. By controlling the polarization of light incident on the NCs, an individual resonance mode can be selectively excited, resulting in signal enhancement over a preferred range and a specifically desired electric near field distribution. Polarization of the incident electric field across the long axis (LA) of the nanocrescent induces either a dipole or quadrupole resonance mode depending on the excitation wavelength. This polarization orientation can thus be used to induce signal enhancement in either the near- or mid-infrared range. Excitation of the dipole mode results in electric near field localization on the tips of the NC while the quadrupole mode exhibits a more delocalized distribution. Excitation across the short axis (SA) of the NC results in a dipole resonance mode at a wavelength range

between the LA dipole and LA quadrupole. This mode also has a unique near field spatial distribution along the backbone and two tips of the structure. A final dipole mode is weakly induced with polarized electric field across both the long and short axes that oscillates perpendicular to all previously described modes and is called the out-of-plane (OOP) dipole. The anisotropy of the NC allows for near field behavior to be controlled using simple far field manipulation and has additional applications in directing analyte molecules and initiating photochemical reactions. Further discussion of this optical behavior is covered in Chapter 3.

1.4 Nanocrescent Organization Effects on Plasmon Resonance Modes

Two additional polarization-dependent resonance peaks appeared in the extinction spectra of nanocrescents fabricated from unique templates. A new peak was observed in the near-infrared region after organization of the nanocrescents into arrays and another appeared deep into the mid-infrared region when aggregation occurred. Initially, the nanosphere templates were organized in order to investigate interparticle distance effects on the spatial distribution of the near field. By close packing and etching (i.e., shrinking) the polystyrene nanosphere templates, rather than random dispersion across the substrate surface, hexagonal arrays of nanocrescents were produced.[35] Manipulating the length of the etching process provides control over both the final template diameter (and consequently, final nanocrescent diameter) and interparticle distance. Unusual effects of the etching process were observed such as nanosphere deformation at long etch times resulting in “spiky beads.” The less-spherical templates produced nonideal nanocrescents that still demonstrated polarization dependent optical behavior. These distorted structures

exhibited a new spectral peak on the visible/near-infrared boundary with SA polarization that represents a previously unobserved resonance mode, most likely a SA quadrupole. This new peak does not appear in the extinction spectra for every nanocrescent array and is therefore a result of the structural defects. A second additional plasmon resonance peak was observed in the mid-infrared for structures fabricated from aggregated templates. This peak is induced with LA polarization and is not the result of plasmonic coupling, but a new dipole resonance across two physically connected nanocrescents. Further insight and details of the organization and observation of these new resonance modes are described in Chapter 4.

1.5 Mid-IR Plasmon Resonance Modes

The polarization anisotropy of the nanocrescent can be combined with its structural tunability to selectively induce LSPR over a visible to infrared range in a single structure. The large majority of plasmonic metal nanostructures have resonance wavelengths in the visible to near-infrared spectral range which, in general, can be lengthened or red-shifted by simply increasing the size of the nanostructure.[16-18] However, LSPR is a nanoscale phenomenon and this resonance wavelength red-shifting is limited for certain shapes as they begin to exhibit bulk material properties at larger sizes. The important factor in maintaining the nanoscale LSPR behavior is the aspect ratio, a feature that is more easily controlled in asymmetric structures. For example, all dimensions of a symmetric nanosphere are increased simultaneously and the aspect ratio is fairly constant. In contrast, the diameter of a nanocrescent can be greatly increased while maintaining nanometer dimensions in the thickness, backbone width, or tip radius. This increases the aspect ratio of the structure and preserves the nanoscale behavior at very large sizes.

There are few plasmonic nanostructures with infrared resonances and the most notable is the nanorod. Like the nanocrescent, the nanorod also exhibits polarization dependence as well as plasmonic resonance modes in the infrared spectral range. The similarities between the two structures are not unexpected as the nanocrescent can be considered a tapered, bent nanorod. These adjustments to the physical form of the structure provide additional features that can be used to tune the LSPR wavelength and introduce more complex electron oscillations. The electron oscillations and near field spatial distributions corresponding to the long and short axis resonance modes described earlier can still be selectively induced in nanocrescents with diameters up to 3 μm and the anisotropic behavior is predicted to continue for even larger sizes. The observation of these far-infrared plasmon resonances is currently limited by the optical range of the substrate material, but polarization dependent spectral peaks have been observed from 500 nm up to 8 μm. The extinction spectra demonstrating the mid-IR LSPR behavior are discussed in Chapter 5.

1.6 Plasmonic Nanocrescents as Surface-Enhanced Spectroscopy Substrates

The unique characteristics of the plasmonic nanocrescent all contribute to increasing the sensitivity and spatial resolution of chemical detection and imaging. The enhancement effects of the confined and intensified electric near fields greatly increase signal to noise ratios, allowing for lower detection limits. The extension of LSPR modes into the infrared spectral range is very important for observation of chemical reactions as the indicators for molecular changes are alterations in vibrational mode frequencies that occur at long wavelengths. The ability of the nanocrescent to support plasmonic

resonances in this region will play a central role in reaction detection by enhancing signals from extremely low analyte concentrations. The polarization anisotropy of the structure is also integral to spectroscopic analysis as specific molecular vibration frequencies can be selectively excited and the specific locations of probe volumes provide knowledge of analyte molecule location. By controlling the polarization orientation and wavelength of the incident electric field, the analyte signal will not only be enhanced, but the physical location of the molecule can be determined within a small probe volume. Organization of the nanocrescent arrays has a great effect on tuning these polarization-dependent advantages, specifically by greatly increasing the range of available template diameters and, subsequently, achievable LSPR wavelengths. The beneficial characteristics of plasmonic nanocrescents as surface enhanced spectroscopy substrates will be discussed throughout with reference to the nanocrescent as an ideal substrate for vibrationally resonant-sum frequency generation (VR-SFG) spectroscopy.

1.7 References

1. Alvarez-Puebla, R.; Liz-Marzán, L. M.; García de Abajo, F. J. Light Concentration at the Nanometer Scale. *J. Phys. Chem. Lett.* **2010,** *1,* 2428-2434.

2. Rang, M.; Jones, A.; Zhou, F.; Li, Z.-Y.; Wiley, B.; Xia, Y.; Raschke, M. Optical Near-Field Mapping of Plasmonic Nanoprisms. *Nano Lett.* **2008,** *8,* 3357-3363.

3. Jeanmaire, D. L.; Van Duyne, R. P., Surface Raman Spectroelectrochemistry: Part I. Heterocyclic, Aromatic, and Aliphatic Amines Adsorbed on the Anodized Silver Electrode. *J. Electroanal. Chem.* **1977,** *84,* 1-20.

4. Le Ru, E. C.; Meyer, M.; Etchegoin, P. G. Proof of Single-Molecule Sensitivity in Surface Enhanced Raman Scattering (SERS) by Means of a Two-Analyte Technique. *J. Phys. Chem. B.* **2006,** *110,* 1944-1948.

5. Le, F.; Brandl, D. W.; Urzhumov, Y. A.; Wang, H.; Kundu, J.; Halas, N. J.; Aizpurua, J.; Nordlander, P. Metallic Nanoparticle Arrays: A Common Substrate for Both Surface-Enhanced Raman Scattering and Surface-Enhanced Infrared Absorption. *ACS Nano.* **2008,** *2,* 707-718.

6. Banik, M.; Nag, A.; El-Khoury, P. Z.; Rodriguez Perez, A.; Guarrotxena, N.; Bazan, G. C.; Apkarian, V. A. Surface-Enhanced Raman Scattering of a Single Nanodumbbell: Dibenzyldithio-Linked Silver Nanospheres. *J. Phys. Chem. C.* **2012,** *116,* 10415-10423.

7. Willets, K. A.; Van Duyne, R. P. Localized Surface Plasmon Resonance Spectroscopy and Sensing. *Ann. Rev. Phys. Chem.* **2007,** *58,* 267-297.

8. Talley, C. E.; Jackson, J. B.; Oubre, C.; Grady, N. K.; Hollars, C. W.; Lane, S. M.; Huser, T. R.; Nordlander, P.; Halas, N. J. Surface-Enhanced Raman Scattering from Individual Au Nanoparticles and Nanoparticle Dimer Substrates. *Nano Lett.* **2005,** *5,* 1569-1574.

9. Aroca, R. F.; Alvarez-Puebla, R. A.; Pieczonka, N.; Sanchez-Cortez, S.; Garcia-Ramos, J. V. Surface-Enhanced Raman Scattering on Colloidal nanostructures. *Adv. Colloid Interface Sci.* **2005,** *116,* 45-61.

10. Aouani, H.; Rahmani, M.; Šípová, H.; Torres, V.; Hegnerová, K.; Beruete, M.; Homola, J.; Hong, M.; Navarro-Cía, M.; Maier, S. A. Plasmonic Nanoantennas for Multispectral Surface-Enhanced Spectroscopies. *J. Phys. Chem. C.* **2013,** *117,* 18620-18626.

11. Johansson, P.; Xu, H.; Käll, M. Surface-Enhanced Raman Scattering and Fluorescence Near Metal Nanoparticles. *Phys. Rev. B.* **2005,** *72,* 035427.

12. Zhang, Z.; Imae, T. Study of Surface-Enhanced Infrared Spectroscopy: 2. Large Enhancement Achieved through Metal-Molecule-Metal Sandwich Configurations. *J. Colloid Interface Sci.* **2001,** *233,* 107-111.

13. Berweger, S.; Atkin, J. M.; Olmon, R. L.; Raschke, M. B. Adiabatic Tip-Plasmon Focusing for Nano-Raman Spectroscopy. *J. Phys. Chem. Lett.* **2010,** *1,* 3427-3432.

14. Sonntag, M. D.; Klingsporn, J. M.; Garibay, L. K.; Roberts, J. M.; Dieringer, J. A.; Seideman, T.; Scheidt, K. A.; Jensen, L.; Schatz, G. C.; Van Duyne, R. P. Single-Molecule Tip-Enhanced Raman Spectroscopy. *J. Phys. Chem. C.* **2012,** *116,* 478-483.

15. Dey, S.; Mirell, D.; Rodriguez Perez, A.; Lee, J.; Apkarian, V. A. Nonlinear Femtosecond Laser Induced Scanning Tunneling Microscopy. *J. Chem. Phys.* **2013,** *138,* 154202.

16. Haynes, C. L.; Van Duyne, R. P. Nanosphere Lithography: A Versatile Nanofabrication Tool for Studies of Size-Dependent Nanoparticle Optics. *J. Phys. Chem. B.* **2001,** *105,* 5599-5611.

17. Hanarp, P.; Käll, M.; Sutherland, D. S. Optical Properties of Short Range Ordered Arrays of Nanometer Gold Disks Prepared by Colloidal Lithography. *J. Phys. Chem. B.* **2003,** *107,* 5768-5772.

18. Bukasov, R.; Shumaker-Parry, J. S. Highly Tunable Infrared Extinction Properties of Gold Nanocrescents. *Nano Lett.* **2007,** *7,* 1113-1118.

19. Hao, F.; Nehl, C. L.; Hafner, J. H.; Nordlander, P. Plasmon Resonances of a Gold Nanostar. *Nano Lett.* **2007,** *7,* 729-732.

20. Bukasov, R.; Ali, T. A.; Nordlander, P.; Shumaker-Parry, J. S. Probing the Plasmonic Near-Field of Gold Nanocrescent Antennas. *ACS Nano.* **2010,** *4,* 6639-6650.

21. Cooper, C. T.; Rodriguez, M.; Blair, S.; Shumaker-Parry, J. S. Polarization Anisotropy of Multiple Localized Plasmon Resonance Modes in Noble Metal Nanocrescents. *J. Phys. Chem. C.* **2014,** *118,* 1167-1173.

22. Titus, E. J.; Weber, M. L.; Stranahan, S. M.; Willets, K. A. Super-Resolution SERS Imaging Beyond the Single-Molecule Limit: An Isotope-Edited Approach. *Nano Lett.* **2012,** *12,* 5103-5110.

23. Barrow, S. J.; Funston, A. M.; Gomez, D. E.; Davis, T. J.; Mulvaney, P. Surface Plasmon Resonances in Strongly Coupled Gold Nanosphere Chains from Monomer to Hexamer. *Nano Lett.* **2011,** *11,* 4180-4187.

24. Im, S. H.; Lee, Y. T.; Wiley, B.; Xia, Y. Large-Scale Synthesis of Silver Nanocubes: The Role of HCl in Promoting Cube Perfection and Monodispersity. *Angew. Chem. Int. Ed.* **2005,** *44,* 2154-2157.

25. Deeb, C.; Zhou, X.; Miller, R.; Gray, S. K.; Marguet, S.; Plain, J.; Wiederrecht, G. P.; Bachelot, R. Mapping the Electromagnetic Near-Field Enhancements of Gold Nanocubes. *J. Phys. Chem. C.* **2012,** *116,* 24374-24740.

26. Jana, N. R.; Gearheart, L.; Murphy, C. J. Wet Chemical Synthesis of High Aspect Ratio Cylindrical Gold Nanorods. *J. Phys. Chem. B.* **2001,** *105,* 4065-4067.

27. Jana, N. R.; Gearheart, L.; Murphy, C. J. Wet Chemical Synthesis of Silver Nanorods and Nanowires of Controllable Aspect Ratio. *Chem. Commun.* **2001**, *7,* 617-618.

28. Murphy, C. J.; Sau, T. K.; Gole, A. M.; Orendorff, C. J.; Gao, J.; Gou, L.; Hunyadi, S. E.; Li, T. Anisotropic Metal Nanoparticles: Synthesis, Assembly, and Optical Applications. *J. Phys. Chem. B.* **2005,** *109,* 13857-13870.

29. Nehl, C. L.; Liao, H.; Hafner, J. H. Optical Properties of Star-Shaped Gold Nanoparticles. *Nano Lett.* **2006,** *6,* 683-688.

30. Taub, N.; Krichevski, O.; Markovich, G. Growth of Gold Nanorods on Surfaces. *J. Phys. Chem. B.* **2003,** *107,* 11579-11582.

31. Wei, Z.; Mieszawska, A. J.; Zamborini, F. P. Synthesis and Manipulation of High Aspect Ratio Gold Nanorods Grown Directly on Surfaces. *Langmuir.* **2004,** *20,* 4322-4326.

32. Aksu, S.; Yanik, A. A.; Adato, R.; Artar, A.; Huang, M.; Altug, H. High-Throughput Nanofabrication of Infrared Plasmonic Nanoantenna Arrays for Vibrational Nanospectroscopy. *Nano Lett.* **2010,** *10,* 2511-2518.

33. Hulteen, J. C.; Treichel, D. A.; Smith, M. T.; Duval, M. L.; Jensen, T. R.; Van Duyne, R. P. Nanosphere Lithography: Size-Tunable Silver Nanoparticle and Surface Cluster Arrays. *J. Phys. Chem. B.* **1999,** *103,* 3854-3863.

34. Shumaker-Parry, J. S.; Rochholz, H.; Kreiter, M. Fabrication of Crescent-Shaped Optical Antennas. *Adv. Mater.* **2005,** *17,* 2131-2134.

35. Haginoya, C.; Ishibashi, M.; Koike, K. Nanostructure Array Fabrication with a Size-Controllable Natural Lithography. *Appl. Phys. Lett.* **1997,** *71,* 2934-2936.

CHAPTER 2

ORGANIZATION AND FABRICATION OF NANOCRESCENTS USING A MODIFIED NANOSPHERE TEMPLATE LITHOGRAPHY PROCEDURE AND METHODS FOR CHARACTERIZATION OF THEIR OPTICAL AND STRUCTURAL PROPERTIES

2.1 Introduction

Plasmonic nanostructures fabricated using the nanosphere template lithography (NTL) method benefit from the combined advantages of both bottom-up and top-down techniques.[1-3] By using individual nanospheres as fabrication templates, the number of structures that can be fabricated in a period of time comparable to synthetic procedures is greatly increased and is further augmented by the scalability of this top-down procedure. The templating procedure also reduces the high time requirement of most fabrication methods by eliminating the stencil development step(s).[4, 5]

Organization of template nanospheres is a relatively simple process and provides the control over final nanostructure arrangement that is expected from fabrication.[6] This property can be exploited to increase the density of structures on a substrate which increases the probability of enhancing analyte signals and more efficiently focuses incident light to nanoscale probe volumes. The ability to produce an ordered arrangement

and control spacing between structures also provides a way to investigate interparticle interactions, such as plasmon coupling, which can be challenging to control.[3, 7, 8]

As a top-down technique, NTL produces fabricated structures which are highly uniform and reproducible with consistent shape, size, and orientation. The ability to modify fabrication parameters provides direct control over structural features that can be used to tune the plasmon resonance wavelength of the nanostructures. These modifications were used to fabricate gold and silver nanocrescent antennas over a broad size and spectral range where the myriad benefits of this procedure were exploited to yield high throughput of consistent structures.[9]

2.2 Experimental Procedures

2.2.1 Materials

BK7 glass microscope slides and soda lime staining jars were purchased from Ted Pella Inc. (Redding, CA). Silicon wafer and CaF_2 disk substrates were purchased from Silicon, Inc. (Boise, ID) and OptoCity (Raleigh, NC), respectively. Concentrated H_2SO_4 and NH_4OH (30% wt.) were purchased from EMD Chemicals. Concentrated HCl and H_2O_2 (30% wt.) were purchased from Sigma-Aldrich. Absolute ethanol (200 proof) was obtained from Pharmco-Aaper, $NaHCO_3$ from Macron Chemicals, and RBS-35 concentrated detergent from Thermo-Scientific. Polystyrene template nanospheres (~2.6% w/v in water) were purchased from Polysciences, Inc. (Warrington, PA) (Table 2.1). Gold and silver pellets (99.999%) were obtained from K. J. Lesker (Clairton, PA). All water used was purified to 18 MΩ using a NANOpureDiamond system from Barnstead.

Table 2.1. Sizes and Specifications of Polystyrene Nanosphere Templates

Size (nm)	σ (nm)	Conc. (% w/v)
119.2	6.9	2.6
200.8	9.7	2.6
356	14	2.6
410	2.3	1.0
456	14.6	2.6
505	8	2.59
771	25	2.62
1025	10	2.62
1925	42	2.6
3004	85	2.6
4518	152	2.62
5940	123	2.56

2.2.2 Substrate Preparation

BK7 glass slides were cut into 25 mm x 25 mm square substrates using a diamond-tipped pen and cleaned using one of two procedures. The first procedure involved immersing the glass squares in piranha solution (3:1 volume ratio of H_2SO_4:30% H_2O_2) in a staining jar. (WARNING: piranha solution is very corrosive as well as exothermic and must be handled with extreme caution. It reacts violently with organic materials and should not be stored in closed containers.) After 30 min., the corrosive piranha solution was decanted and neutralized with $NaHCO_3$. The glass substrates were rinsed repeatedly (minimum of three times) with nanopure water and then sonicated for 1 hour at 50°C in a solution of 5:1:1 volume ratio H_2O:NH_4OH:H_2O_2. After sonication, the substrates were again rinsed copiously with nanopure water and either used immediately or stored in nanopure water. The second procedure is simpler and uses less hazardous chemicals. After cutting, substrates were placed in staining jars and immersed in 20% v/v RBS-35 detergent solution diluted with water heated to 50°C. The substrates were then sonicated at 50°C for 5 min. The detergent solution and multiple subsequent rinsings with nanopure water were removed by suction with the substrates being rinsed until detergent bubbles stopped forming. A new solution of 1:1 v/v ethanol: HCl was added and allowed to react for 30 min. Several water rinses were repeated with all solutions removed by suction and the substrates were dried overnight in a 60°C oven. The glass substrates were cooled to room temperature in a closed container before immediate use or stored under nitrogen in sealed containers.

Silicon wafers were also cut to size using a diamond-tipped pen and the resulting square substrates, as well as all CaF_2 disk substrates, were cleaned using a Jelight model

352 UV-Ozone cleaner for 10 min on each side.

2.2.3 Template Preparation

Templates for isolated nanocrescents were made by diluting stock solutions of polystyrene nanospheres to 0.13% w/v (1:20 dilution) with ethanol. The low nanosphere concentration prevented template aggregation while the ethanol increased surface wetting and the solvent evaporation rate. Two methods were used to disperse template nanospheres across the surface of the substrate for isolated nanocrescent fabrication. The first method, drop casting, involved depositing 50 μL of the dilute template solution on a clean, dry substrate, rotating/tilting the substrate to wet as much surface as possible, and then quickly evaporating the solvent under a gentle flow of nitrogen. For the second method of spin casting, a clean, dry substrate was placed in a spin coater and, after a steady spinning rate of 700 rpm was reached, 50 μL of the dilute template solution was deposited. The speed was then maintained for 25 s while solvent evaporated. Both casting methods result in high surface coverage of isolated nanosphere templates.

Hexagonally close packed (HCP) templates were prepared by diluting stock nanosphere solutions to ~0.5% w/v (1:5 dilution) for small diameter templates (<1000 nm) or ~0.65% w/v (1:4 dilution) for large diameter templates (>1000 nm) with the final volume of the dilute solution containing equal parts water and ethanol. For example, for a large diameter template solution with final dilution volume of 1 mL, 250 μL of stock solution in water was diluted with an additional 250 μL of water and 500 μL of ethanol. A 50 μL aliquot of the diluted template solution was then deposited on a cleaned glass, silicon, or CaF_2 substrate that was rotated and tilted to wet as much surface as possible. The substrate was then laid flat, allowing the nanospheres to self-assemble into a

hexagonally close-packed monolayer while the solvent evaporated under ambient conditions. These solution conditions resulted in large area coverage of HCP nanosphere template arrays.

In order to increase interparticle spacing and make the HCP templates useful for nanofabrication, the diameters of the polystyrene nanospheres were reduced via reactive ion etching (RIE) using oxygen plasma (Fig. 2.1).[10] The fabrication procedure using the templates includes an angled metal deposition step that requires spacing between the template nanospheres. An increased interparticle distance was achieved by size reduction of the polystyrene templates. The etching was accomplished by placing substrates with close-packed nanospheres in an Oxford PlasmaLab 80+ Reactive Ion Etch (RIE) instrument (Yatton, Bristol, UK). Oxygen plasma was then initiated at a flow rate of 10 sccm. Two different power settings, 100 W and 75 W, were utilized. The nanosphere templates were etched over a broad range of time lengths at both power settings to investigate the dependence of the etch rate on power. The RIE shrinking process can be used to control the interparticle distance and final diameter of the template nanospheres while maintaining an ordered template arrangement.

2.2.4 Nanocrescent Fabrication

Both types of templates (isolated and arrayed) were used for nanocrescent fabrication using a modified nanosphere template lithography (NTL) procedure (Fig. 2.2). Substrates covered by either disperse or etched HCP polystyrene templates were attached to 40° angled mounts and fixed on a custom holder in the chamber of a Denton SJ20C E-Beam Evaporator (Denton Vacuum, Moorestown, NJ). Gold or silver metal was then evaporated at an average rate of 2.0 Å/s under high vacuum resulting in the angled

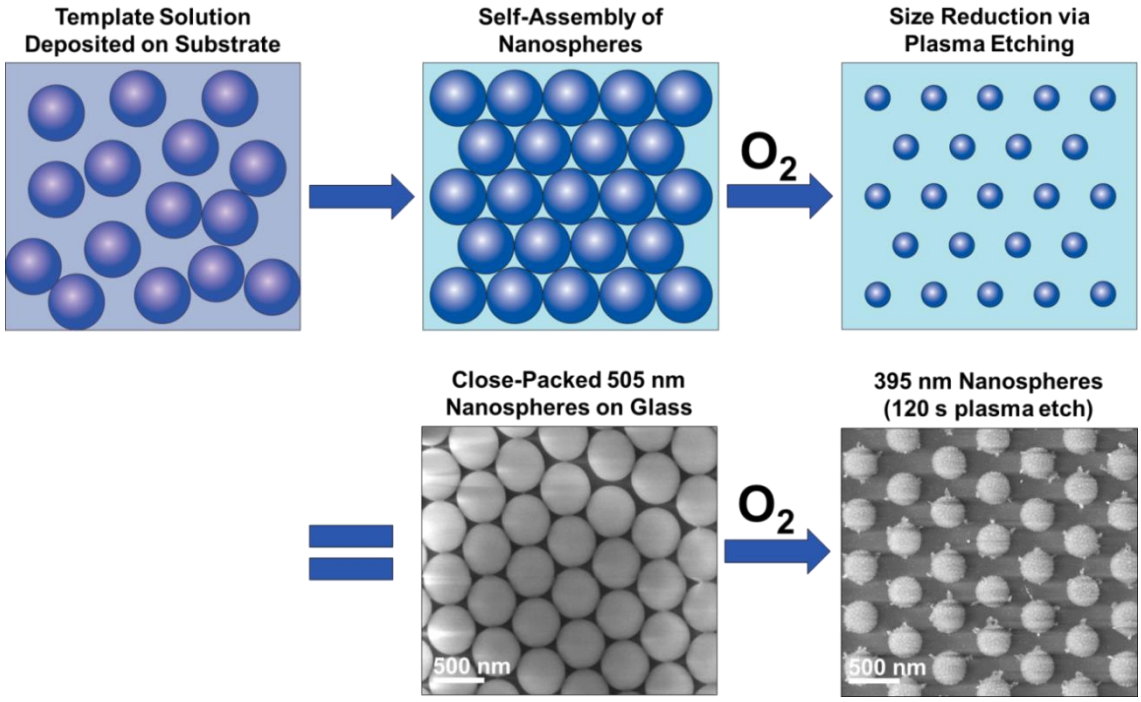

Figure 2.1. Schematic of self-assembly of hexagonal close packing of template nanospheres and size reduction via oxygen plasma etching (top). Scanning electron micrographs demonstrate shrinking of 505 nm nanospheres to 395 nm with a 120 s plasma etch at 100 W power (bottom).

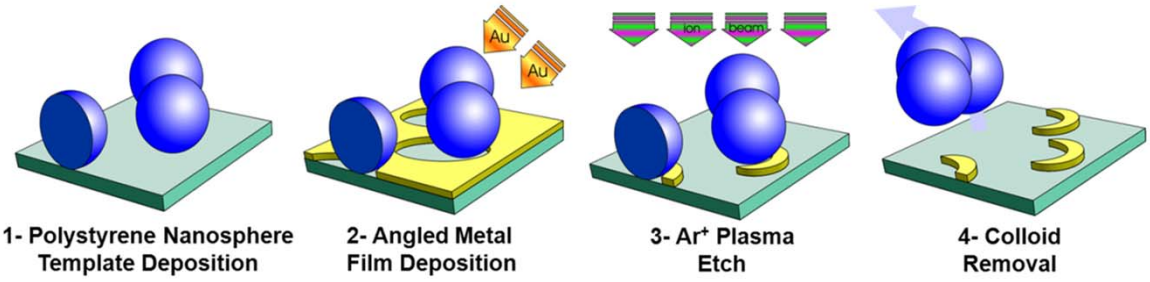

Figure 2.2. Schematic of nanosphere template lithography fabrication procedure. Modified from Reference 9.

deposition of a 50 nm thin film. Following metal deposition, the substrates were placed in an Oxford PlasmaLab 80+ RIE system (Oxford Instruments, UK) where most of the metal film was etched away normal to the surface using Ar^+ plasma at a power of 100 W and flow rate of 10 sccm. The combination of the angled metal deposition and perpendicular Ar^+ plasma etching on the nanosphere templates produces crescent-shaped structures. The fabricated samples were stored under nitrogen in air-tight containers.

2.2.5 Characterization of Optical and Structural Properties

The localized surface plasmon resonance properties of both gold and silver nanocrescents were analyzed via their optical responses obtained using a Perkin Elmer Lambda 750 UV/Vis/NIR spectrophotometer (Waltham, MA) over a wavelength range of 400-3200 nm and a Perkin Elmer Spectrum 100 FT-IR (Waltham, MA) over a range of 2500-10500 nm. The beam for the UV/Vis/NIR has a 12 mm x 4.5 mm elliptical spot size while the FT-IR has a 10.5 mm diameter circular beam for probe areas of 1.7×10^8 μm^2 and 3.5×10^8 μm^2, respectively. An initial probe scan of each sample using unpolarized light in the Lambda 750 was performed first to determine the maximum wavelengths (λ_{max}) of the two strongest dipole resonance modes of the nanocrescent. Two polarization spectra for each sample were then obtained while varying the polarization angle from 10° to 330° using a polarizer crystal (Perkin Elmer #B0505284) and each determined λ_{max} as a constant wavelength. These polarization scans result in sinusoidal spectra with maxima at the angles of selective excitation for the individual resonance modes. The angles determined from the maxima of the polarization spectra were used to acquire full extinction spectroscopy scans at a constant angle over a wavelength range of 400-3200 nm. With the incident light polarized at the predetermined angles, two extinction spectra

were obtained for each sample with distinct, selectively induced plasmon resonance modes.

A similar process was repeated using the Spectrum 100 FT-IR instrument for samples with resonance wavelengths outside the range of the Lambda 750. An initial unpolarized spectrum was obtained which was then normalized and combined with the UV/Vis/NIR spectrum using Microsoft Excel to characterize the multiple plasmon resonance bands over a broad wavelength range. The two sinusoidal, constant wavelength, polarization spectra were generally not obtained on the FT-IR because the angles of selective excitation were already known from the UV/Vis/NIR analysis and were used to acquire polarized scans. For these polarization studies in the infrared, a KRS-5 crystal polarizer was implemented in the Spectrum 100 FT-IR over a wavelength range of 2500-10500nm. Several examples of UV/Vis/NIR and FT-IR spectra obtained for gold and silver nanocrescents with a broad range of physical parameters will be presented and discussed in Chapters 3-5.

Physical characterization of the nanocrescents was achieved using scanning electron microscopy (SEM) analysis with an FEI NovaNano 630 SEM under low vacuum using a Helix detector in immersion mode. The same instrument was used to obtain images of the isolated and arrayed nanosphere templates, both before and after etching. The ImageJ image analysis program available from the National Institutes of Health (NIH) was used to measure final template and nanocrescent diameters as well as interparticle distances in the SEM images.

2.2.6 Theoretical Calculations

Extinction spectra and electric near field distribution simulations were calculated using finite-difference time-domain (FDTD) methods. The values were computed using FDTD Solutions software from Lumerical Solutions, Inc. with a mesh resolution of 2 nm in all directions of a three-dimensional setup. The refractive indices used for gold, silver, and glass were fitted material properties to Palik values while the values for CaF_2 were obtained from the OptoCity manufacturer. Model structures were generated using dimensions measured from fabricated nanocrescents and included a 5 μm thick glass or CaF_2 substrate. However, electric fields localized at the nanocrescent surface are expected to decay rapidly and the substrate thickness was consequently reduced to approximately 1.5 μm by perfectly matched layer (PML) boundaries which act to absorb and prevent reflection of incident fields. The nanocrescent model was enclosed by six two-dimensional power flow monitors to determine the absorption cross section with six additional power flow monitors enclosing the source to ascertain the scattering cross section. The extinction spectra were then calculated as the sum of the absorption and scattering cross sections using a wideband source from 800 nm to 2600 nm for smaller diameter nanocrescents ($\leq$ 500 nm) and 800 nm to 9000 nm for larger diameter nanocrescents ($\geq$ 500 nm). MATLAB computer software was used to generate the near field images.

2.3 Results and Discussion

Nanosphere template lithography was used to fabricate gold and silver nanocrescents over a broad size range on several substrate materials (Fig. 2.3). The method is simple, involving four steps: template deposition, angled metal film deposition,

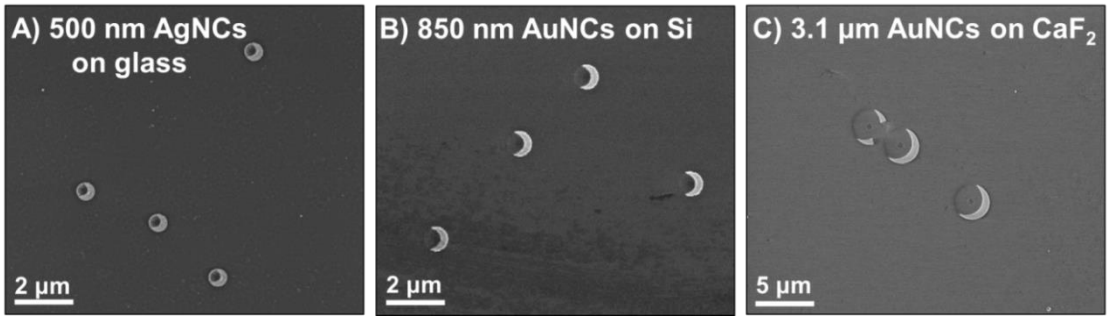

Figure 2.3. Nanocrescents fabricated using nanosphere template lithography with various compositions, sizes, and substrates. A) Five hundred nm diameter silver nanocrescents (AgNCs) on BK7 glass, B) 850 nm diameter gold nanocrescents (AuNCs) on a silicon wafer, and C) 3.1 µm diameter AuNCs on CaF_2. All samples shown were fabricated from untreated (i.e., unetched), disperse polystyrene nanospheres and demonstrate the versatility of the fabrication technique.

plasma etch, and colloid removal (Fig. 2.2). The versatility of this fabrication technique allows for direct control over several structural features of the nanocrescent. The final nanocrescent diameter was adjusted by the size of the template nanosphere which, in some cases, was controlled by oxygen plasma shrinking.[10, 11] This control via simple modification to the procedure provided a dynamic range of nanosphere sizes for fabrication, including sizes not commercially available. The thickness of the nanocrescents was controlled by the thickness of the deposited metal film. The angle of metal deposition can be used to control the width of the nanocrescent backbone and radius of tip curvature for a specific template size.[12] Rotation of the substrate followed by a second film deposition can also be utilized to adjust the nanocrescent tips, specifically their proximity or tip-gap. For ease of comparison, all nanocrescent structures discussed throughout this work were fabricated at a metal deposition angle of 40° without rotation and have an open-tip configuration (i.e., a tip-gap of 90°). Any variance in backbone widths and tip radii will be an effect of the different template diameters used.

A small debris trail is often observed between the tips of smaller diameter nanocrescents (Fig. 2.3A). This is caused by the re-deposition of insignificant (<10 nm) metal particles underneath the template nanospheres during the etching process. Both theoretical and experimental results have shown that these particles are negligible and have no effect on the optical properties of nanocrescents.

Nanocrescents fabricated using the NTL procedure were characterized for their structural and optical properties.[12, 13] The plasmon resonance wavelengths of the various size nanocrescents were measured using UV-Vis-NIR and FT-IR spectroscopy over a 400-10500 nm wavelength range. Differences observed in the spectra, such as the

presence, location (λ_{max}), and width of peaks (Fig. 1.3), were compared to calculated spectra and correlated with physical properties revealed in scanning electron micrographs (Fig. 2.3) to form conclusions about the plasmonic behavior of nanocrescent structures.

2.4 Conclusion

Gold and silver nanocrescents with tunable structural features were fabricated using nanosphere template lithography. The addition of a template etching step extended the available range of nanosphere diameters. The NTL procedure provides a straightforward approach to control nanostructure features and the modification of physical parameters such as the diameter, backbone width, and tip radius was used to tune the resonance wavelength of the plasmonic nanocrescent over a visible to infrared spectral range.

2.5 References

1. Hulteen, J. C.; Treichel, D. A.; Smith, M. T.; Duval, M. L.; Jensen, T. R.; Van Duyne, R. P. Nanosphere Lithography: Size-Tunable Silver Nanoparticle and Surface Cluster Arrays. *J. Phys. Chem. B.* **1999,** *103,* 3854-3863.

2. Haynes, C. L.; Van Duyne, R. P. Nanosphere Lithography: A Versatile Nanofabrication Tool for Studies of Size-Dependent Nanoparticle Optics. *J. Phys. Chem. .B* **2001,** *105,* 5599-5611.

3. Haynes, C. L.; McFarland, A. D.; Smith, M. T.; Hulteen, J. C.; Van Duyne, R. P. Angle-Resolved Nanosphere Lithography: Manipulation of Nanoparticle Size, Shape, and Interparticle Spacing. *J. Phys. Chem. B.* **2002,** *106,* 1898-1902.

4. Jiang, P. Large-Scale Fabrication of Periodic Nanostructured Materials by Using Hexagonal Non-Close-Packed Colloidal Crystals as Templates. *Langmuir.* **2006,** *22,* 3955-3958.

5. Saavedra, H.; Mullen, T. J.; Zhang, P.; Dewey, D.; Claridge, S.; Weiss, P. Hybrid Strategies in Nanolithography. *Rep. Prog. Phys.* **2010,** *73,* 036501.

6. Schweikart, A.; Pazos-Perez, N.; Alvarez-Puebla, R. A.; Fery, A. Controlling Inter-Nanoparticle Coupling by Wrinkle-Assisted Assembly. *Soft Matter.* **2011,** *7,* 4093-4100.

7. Kinnan, M. K.; Chumanov, G. Plasmon Coupling in Two-Dimensional Arrays of Silver Nanoparticles: II. Effect of the Particle Size and Interparticle Distance *J. Phys. Chem. C.* **2010,** *114,* 7496-7501.

8. Zhao, L.; Kelly, K. L.; Schatz, G. C. The Extinction Spectra of Silver Nanoparticle Arrays: Influence of Array Structure on Plasmon Resonance Wavelength and Width. *J. Phys. Chem. B.* **2003,** *107,* 7343-7350.

9. Shumaker-Parry, J. S.; Rochholz, H.; Kreiter, M. Fabrication of Crescent-Shaped Optical Antennas. *Adv. Mater.* **2005,** *17,* 2131-2134.

10. Haginoya, C.; Ishibashi, M.; Koike, K. Nanostructure Array Fabrication with a Size-Controllable Natural Lithography. *Appl. Phys. Lett.* **1997,** *71,* 2934-2936.

11. Cooper, C. T.; Gore, C. T.; Shumaker-Parry, J. S. Plasmonic Nanocrescent Arrays Fabricated by Controlled Plasma Etching of Polystyrene Nanosphere Templates. (Submitted).

12. Bukasov, R.; Shumaker-Parry, J. S. Highly Tunable Infrared Extinction Properties of Gold Nanocrescents. *Nano Lett.* **2007,** *7,* 1113-1118.

13. Cooper, C. T.; Rodriguez, M.; Blair, S.; Shumaker-Parry, J. S. Polarization Anisotropy of Multiple Localized Plasmon Resonance Modes in Noble Metal Nanocrescents. *J. Phys. Chem. C.* **2014,** *118,* 1167-1173.

CHAPTER 3

POLARIZATION ANISOTROPY OF MULTIPLE LOCALIZED PLASMON RESONANCE MODES IN NOBLE METAL NANOCRESCENTS*

3.1 Introduction

Manipulating light in a controlled manner has led to advances in spatial resolution beyond the diffraction limit for imaging and spectroscopy techniques. One approach to this nanofocusing uses localized surface plasmon resonances (LSPR) in noble metal nanostructures which confine local fields to nanoscale probe volumes.[1] This reduction in probe volume has been used to push the spatial limits of the resolution of characterization techniques like surface or tip enhanced Raman spectroscopy (SERS and TERS, respectively)[1-3] and nonlinear laser-induced scanning tunneling microscopy (NLL-STM)[4] while the local field confinement enhances signals for vibrational spectroscopy to obtain local chemical information.

A key factor in pushing the limits of spatial resolution and maximizing signal enhancements is the architecture of the plasmonic nanostructures. Great efforts have been made in designing, optimizing and characterizing a wide variety of metallic nanoparticles through both synthetic (bottom-up) and fabrication (top-down) techniques. Some of the more common shapes of plasmonic nanostructures include colloidal spheres,[5] rods[6, 7] and cubes[8, 9] as well as fabricated disks,[10] rings[11] and triangles.[12, 13] As the shapes of these

*Reproduced with permission from *J. Phys. Chem. C.* **2014,** *118,* 1167-1173.

structures become more complex, the resulting plasmon resonance modes and electromagnetic field distributions increase in complexity as well.[14-16]

Recent studies have utilized the dependence of the optical response of asymmetric plasmonic nanostructures on the polarization of incident light to better understand the correlation between induced plasmon modes and optical near field distributions as well as how to exploit and control surface enhancement effects. Previous investigations have used polarization controlled illumination to map the location and distribution of enhanced near fields via photopolymerization,[9] correlate SERS signal intensity with theoretically predicted regions of high electric field enhancement or "hot spots,"[17-19] determine the orientation of particles or ligand molecules,[20, 21] and better understand the electromagnetic effect of signal enhancement.[22]

The anisotropic characteristic of asymmetric nanostructures has another advantage that has not been fully explored, namely the opportunity to control the spatial distribution of optical near field enhancements through polarization of incident light. Hot spots are formed by the spatial confinement of electrons to small structural regions, effectively focusing incident energy from a far field source to nanoscale probe volumes. Manipulation of the near field in this manner could improve spatial resolution by predictably and controllably limiting probe volumes as well as make it possible to determine the physical locations of analytes with respect to plasmonic structures, control light-matter interactions, and initiate photochemical reactions in specific locations.[9]

Here, I present investigations of the polarization anisotropy of noble metal nanocrescents using extinction spectroscopy. Simulations of the electric near field behavior of plasmonic gold and silver nanocrescent structures (AuNC and AgNC,

respectively) predict unique field enhancement distributions based on the induced plasmon resonance mode.[23] I demonstrate the controlled induction of several plasmon resonance modes and their optical responses to polarized light. These modes are well resolved spectrally and occur within distinct wavelength ranges. The anisotropy of the structure allows the modes to be turned on or off or, in the case of broadband excitation, the independent excitation of a single mode at a specific wavelength based on polarization controlled illumination. Calculations predict the generation of hot spots at unique locations on the nanocrescent corresponding to each plasmon mode, indicating the potential for near field manipulation by controlling the polarization of incident light. Preliminary results for utilizing polarization-controlled plasmonic enhancement effects in nonlinear processes are discussed.

3.2 Experimental Procedures

3.2.1 Nonlinear Microscopy: Two-Photon Fluorescence and Second Harmonic Generation

Gold nanocrescents were used as surface enhancing substrates to increase the efficiency of two nonlinear optical processes, two-photon fluorescence (2PF) and second harmonic generation (SHG). The schematic for the microscope setup as well as spectral and structural characterization of the nanocrescent are shown in Figure 3.1. Templates with diameters of 130 nm were used to fabricate 214 nm diameter nanocrescents with a short axis LSPR wavelength of 800 nm, matching the emission wavelength of the femtosecond near-infrared laser. It was predicted that enhanced electric near field intensities resulting from the induced short axis dipole resonance mode would improve both nonlinear processes, allowing for a higher rate of input photon combination and

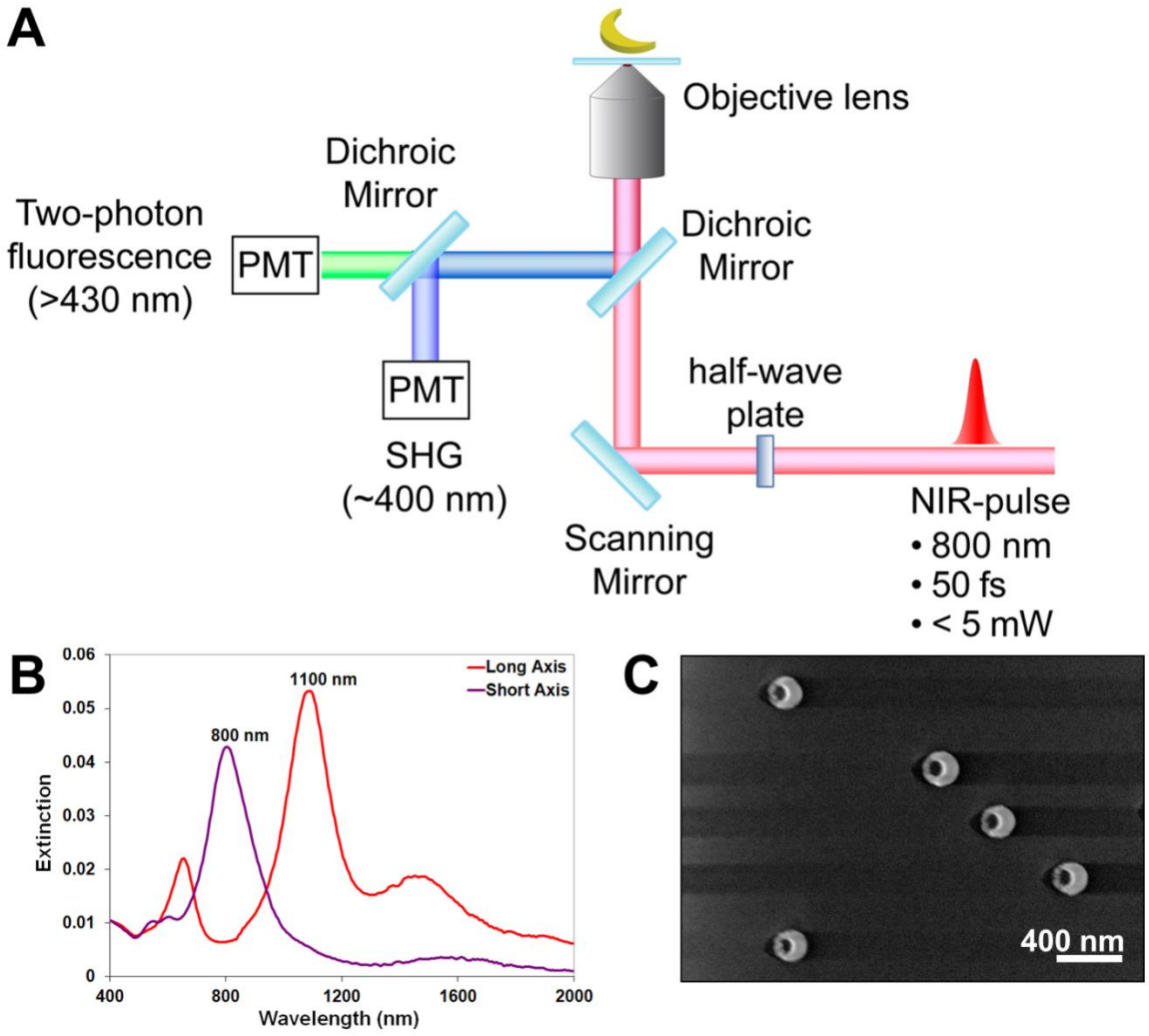

Figure 3.1. Application of plasmonic nanocrescent near field enhancement effects to nonlinear optical techniques. A) Experimental setup for nonlinear two-photon fluorescence (2PF) and second harmonic generation (SHG) microscopy. B) Polarized extinction spectra for 215 nm diameter gold nanocrescents. The short axis polarized spectrum (purple) is on resonance with the near-infrared laser at 800 nm. C) Scanning electron micrograph of nanocrescents used in nonlinear microscopy experiment.

increased output photon intensity at higher energies. The orthogonal plasmon resonance mode had a λ_{max} = 1100 nm, which was off resonance and would theoretically not enhance either nonlinear process.

The gold nanocrescent substrate was illuminated in reflection mode using a 0.65 NA objective lens with 50 fs pulses at low power (<5 mW). With short axis polarization, the resonance and laser wavelengths overlapped in order for an increase in electric field intensity to occur. The use of a low initial power ensured that 2PF and SHG would not occur independently, without the field enhancing effects of the plasmonic nanocrescent. Pixel intensities at the same location in 2PF and SHG microscopy images obtained for both short and long axis polarized excitation were compared to determine if a dependence on incident light polarization existed and could be used to control the nonlinear processes. The images were also analyzed to determine if the enhanced nanocrescent near fields were strong enough to initiate the generation of higher energy photons.

3.3 Results and Discussion

3.3.1 Asymmetric Nanocrescent Structure

The drop casting technique and modified nanosphere template lithography (NTL) procedure were used to fabricate nanocrescents where each nanosphere was utilized as an individual template to produce isolated nanostructures with controllable and uniform size, shape, and orientation (Fig. 3.2). Several parameters of the fabrication technique can be systematically changed to control nanocrescent thickness, tip sharpness, tip gap angle, direction, and other structural characteristics.[24, 25] This uniformity allows the optical properties, including multiple polarization-dependent LSPR modes, of the nanocrescent to be probed in ensemble measurements. For this study, I focused on open-structure

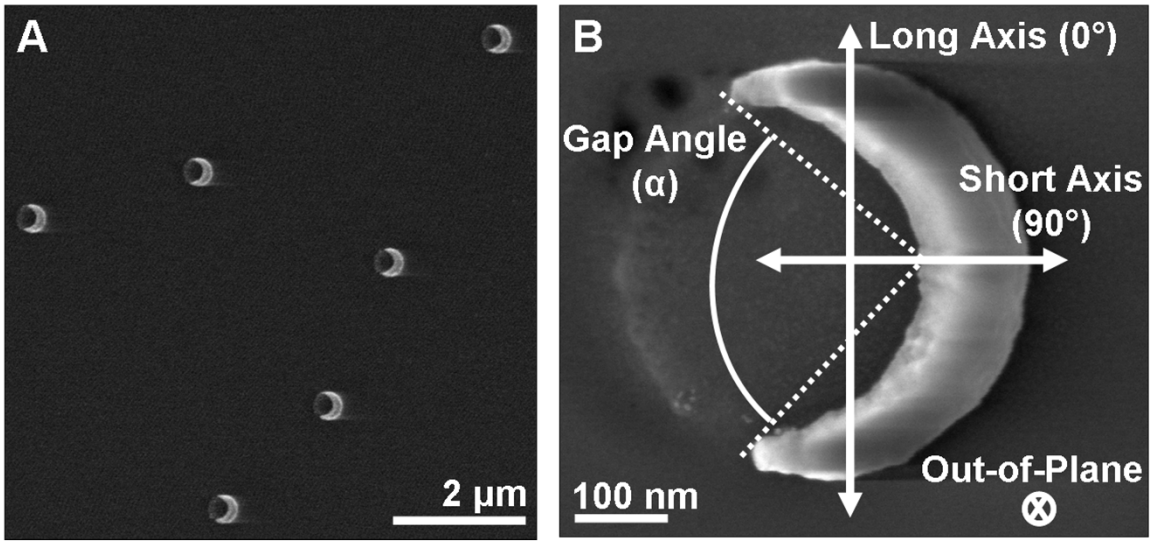

Figure 3.2. SEM images of 445 nm diameter AuNCs. A) Disperse structures show the uniformity of size, shape, and orientation resulting from NTL fabrication. B) Illustration of the direction of electric field polarization with respect to nanocrescent axes for selective excitation of individual plasmon resonance modes.
Modified from Reference 28.

nanocrescents with relatively large tip gap angles ($\alpha \approx 90^{\circ}$, Fig. 3.2B) and diameters over a range of 100-500 nm. The asymmetry of these open nanocrescents gives rise to multiple distinct LSPR modes which can be induced in the same structure. The wavelengths of these resonance modes were determined using simple extinction spectroscopy and studied for polarization dependent behavior.

3.3.2 Optical Properties of Polarization-Dependent Plasmon Resonance Modes

Typical extinction spectra for open-tip gold or silver nanocrescents illuminated with unpolarized light exhibit multiple distinct plasmon resonance modes as four unique peaks (Fig. 3.3B and D). Each of these peaks represents a resonance mode corresponding to a distinct directional oscillation of electrons associated with the polarization of the electric field of the incident light with respect to the orientation of the nanostructure. The plasmon resonance modes occur over a specific range of wavelengths which can be tuned by altering physical aspects of the nanostructure.[24] Polarizing the incident light along specific axes of the nanocrescent (defined in Fig. 3.2B) allows for selective excitation of particular resonance modes. Spectral peaks corresponding to the individual modes, termed the long axis dipole (LA-D), short axis dipole (SA-D), long axis quadrupole (LA-Q), and out-of-plane dipole (OOP-D), are labeled in the spectra of Figure 3.3. Simulations of the near field enhancement resulting from the unique electron oscillations for the three former resonance modes (LA-D, SA-D, and LA-Q), are shown in Figure 3.4.

The two long axis (LA) resonance modes can be selectively induced when light is polarized along the long axis of the nanocrescent (0°, Fig. 3.2B). Incident light polarized in this manner induces either a dipole or quadrupole plasmon resonance mode depending

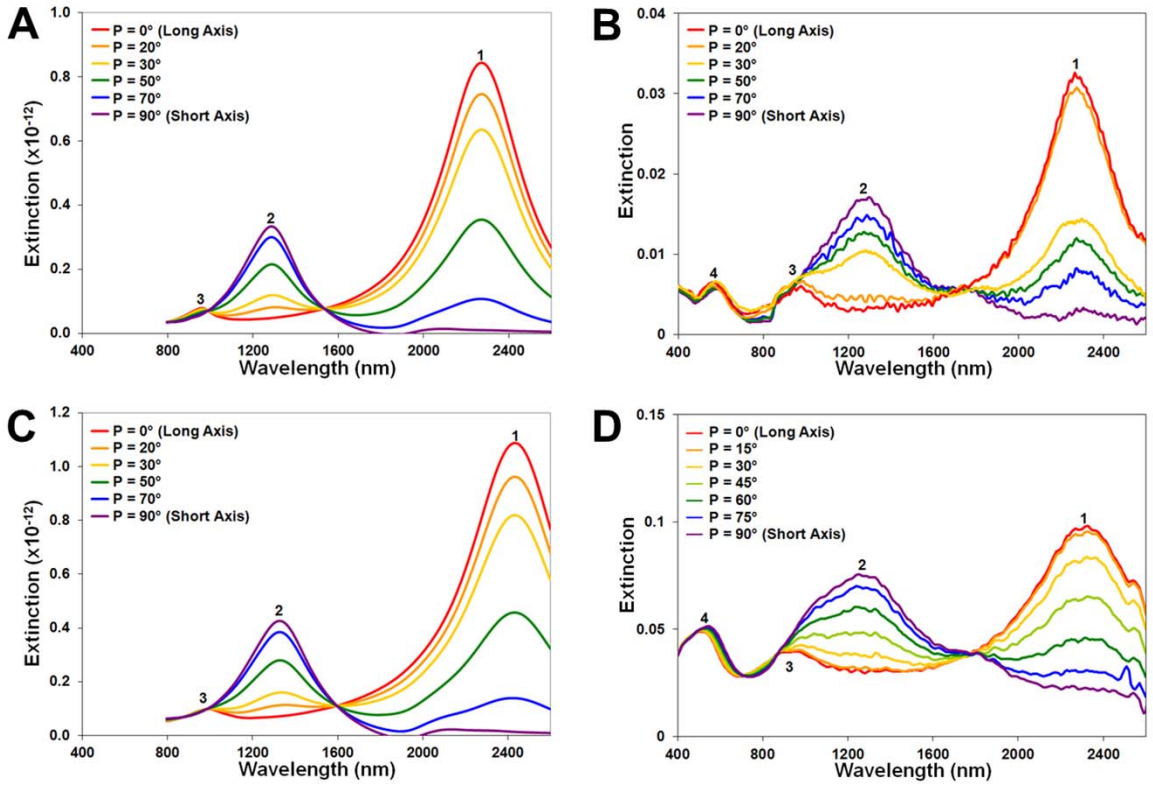

Figure 3.3. Calculated and experimental polarized extinction spectra demonstrating selective induction of long and short axis plasmon resonance modes. Samples are 445 nm diameter AuNCs (A, B) and AgNCs (C, D). Differences in extinction values (y-axis) are due to single nanocrescent simulations for the calculated spectra (A, C) while the experimental data (B, D) are from ensemble measurements. The varying polarization angles (P) demonstrate selective excitation, co-excitation, or nonexcitation of resonances at specific angles. Peak labels correspond to unique resonance modes described in text: 1- long axis dipole, 2- short axis dipole, 3- long axis quadrupole, 4- out-of-plane dipole. Long and short axis resonance modes are selectively excited at 0° and 90° (red and purple spectra), respectively.
Modified from Reference 28.

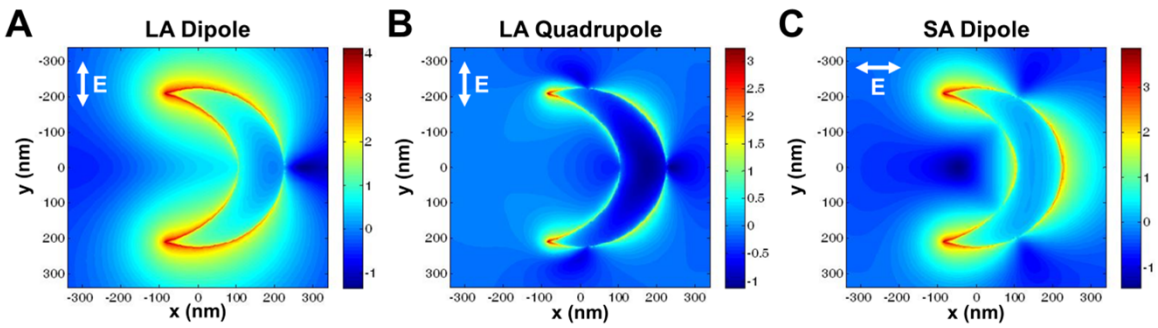

Figure 3.4. Calculated near field enhancement, I/I_0, maps for polarization-dependent resonance modes of 445 nm diameter template AuNC. A) Long axis dipole, B) long axis quadrupole, and C) short axis dipole. Electric field polarization, E, indicated by arrows. Intensity scale is logarithmic.
Modified from Reference 28.

on the wavelength. Excitation of the LA-D occurs in the near-infrared to infrared wavelength range (1000-3000 nm) and results in an oscillation of electrons between the two symmetric halves of the nanocrescent structure. This resonance occurs at the lowest energy wavelength for any of the nanocrescent resonance modes but has the highest calculated electric field enhancement (I/I_0), localized at the tips, resulting from the high spatial confinement of electrons to the smallest region of the nanocrescent (Fig. 3.4A). The LA-Q couples less strongly with incident light than the dipolar mode, resulting in a much weaker spectral peak and lower calculated field enhancement. This higher order resonance mode involves four distinct regions of charge separation, the oscillation of which results in four spatially localized regions of near field enhancement (Fig. 3.4B). This plasmon resonance mode is present as a distinct peak in all LA polarized spectra for gold and silver nanocrescents within a spectral range of approximately 600-1200 nm.

When the electric field polarization is orthogonal to LA excitation (90°, Fig. 3.2B), the short axis (SA) dipole resonance mode is induced. Oscillations of electrons in this mode alternate between the nanocrescent tips and backbone (Fig. 3.4C). This direction of oscillation leads to a more delocalized near field distribution for SA polarization and a lower calculated field enhancement factor than the stronger LA-D. This is attributed to the decreased spatial confinement of electrons for this mode leading to a lower local electric potential difference. The resulting SA-D spectral peak observed between the wavelengths of 700 nm and 2200 nm is also lower in amplitude than the LA-D at respective maximum excitation angles, indicating relatively strong, but not the most efficient coupling with incident light. No higher order resonances were observed for this polarization in the open-tip nanocrescents.

The out-of-plane resonance mode, a weak dipole that oscillates perpendicular to the plane of the nanocrescent, is observed for both LA and SA polarization in the visible range (Fig. 3.3B and D). The presence of this peak in all spectra is attributed to the non-collimated light source. With light incident from many angles, the dipole for this resonance mode is weakly induced, coupling less strongly with incident light than the in-plane dipole modes. This mode is largely independent of incident polarization (Fig. 3.5D) and is not included in the simulated spectra.

The selective excitation of the three LA and SA modes is demonstrated in Figure 3.3 for both Au and Ag nanocrescents. The changes in peak amplitude indicate the transition from distinct excitation to simultaneous excitation to nonexcitation of the individual resonance modes as the incident polarization angle is rotated with respect to the structure. The polarization dependence is observed in both calculated and experimental spectra. Here, AuNCs fabricated from 356 nm diameter templates with final diameters of 445 nm serve as a representative example (Fig. 3.3A and B). At 0°, the LA resonance mode was selectively induced and the corresponding spectra (red) have two distinct peaks in the near-infrared region. The high amplitude peaks at 2275 nm (theoretical, Fig. 3.3A) and 2278 nm (experimental, Fig. 3.3B) correspond to the LA-D and are in excellent agreement for the wavelength of this plasmon mode (Table 3.1). The smaller peaks at 950 nm and 962 nm (theoretical and experimental, respectively) represent the quadrupole and again show excellent agreement between calculated and measured resonance wavelength values for the plasmon mode. Both of these peaks diminish in amplitude as the polarization angle of the incident light is increased from 0° to 90°. It can be seen that at 50°, approximately halfway between the maximum

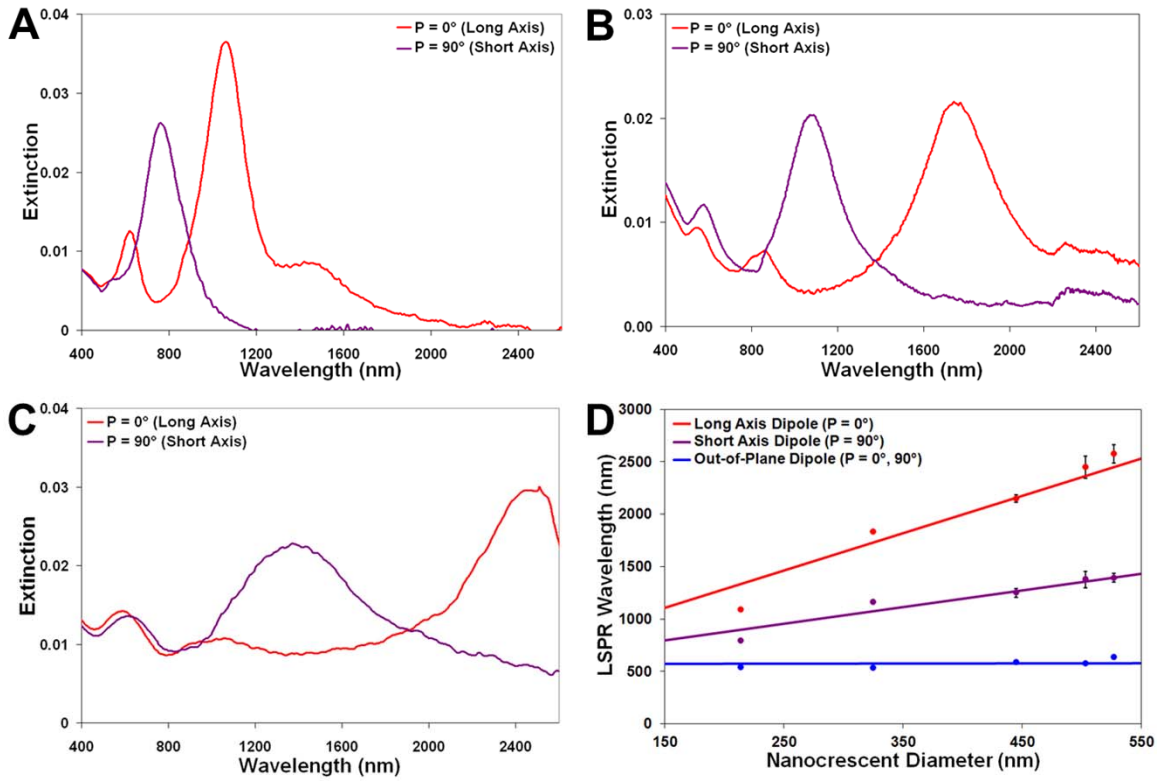

Figure 3.5. Selective induction of polarization-dependent plasmon resonance modes over a broad size range. Extinction spectra of AuNCs with diameters of A) 215 nm, B) 325 nm, and C) 530 nm show selective excitation of long and short axis resonance modes at 0° (red) and 90° (purple), respectively. D) Dependence of average resonance wavelength of AuNCs on nanocrescent diameter.
Modified from Reference 28.

Table 3.1. Theoretical and Experimental Values for Wavelengths of Distinct Plasmon Resonance Modes

	AuNC (445 nm diameter)			**AgNC (445 nm diameter)**		
Resonance Mode	Theory	Experiment	$\Delta_{th\text{-}exp}$*	Theory	Experiment	$\Delta_{th\text{-}exp}$*
LA-Dipole	2275 nm	2278 nm	3 nm	2427 nm	2330 nm	97 nm
LA-Quadrupole	950 nm	962 nm	12 nm	988 nm	950 nm	38 nm
SA-Dipole	1295 nm	1284 nm	11 nm	1333 nm	1250 nm	83 nm

*Difference between theoretical (th) and experimental (exp) resonance wavelengths (absolute values).
Modified from Reference 28.

excitation angles, both the LA and SA resonance modes were simultaneously induced and all three polarization dependent plasmon mode peaks are present in the spectra, although at decreased amplitudes. At 90°, perpendicular to LA excitation, the SA resonance mode was selectively excited (purple spectra). The peaks at 2275 nm and 950 nm previously observed in the LA polarized spectra are not observed at this polarization angle and the new peaks at 1295 nm (theoretical, Fig. 3.3A) and 1284 nm (experimental, Fig. 3.3B) correspond to a SA dipolar oscillation.

A similar, polarization-based selective induction of distinct plasmon resonance modes was observed for the AgNCs (Fig. 3.3C and D). The calculated values for the LA-D, LA-Q, and SA-D have slightly greater differences from the experimental values than the AuNC sample due to a less perfect fit for the refractive index values used for silver, but are all within 100 nm of the measured values (Table 3.1). The optical response pattern described was observed in additional gold and silver nanocrescent samples over a broad size range. Extinction spectra for AuNCs with diameters of 215 nm, 325 nm, and 530 nm show the polarization-controlled induction of the LA and SA plasmon resonance modes in both smaller and larger diameter nanocrescents (Fig. 3.5A-C). A plot of the average wavelength for the three dipolar plasmon resonance modes (LA-D, SA-D, and OOP-D) demonstrates the persistence of the anisotropic behavior of the long and short axis modes over a visible to near-infrared spectral range, polarization independence of the out-of-plane mode, and a linear trend in resonance wavelength with respect to nanocrescent diameter (Fig. 3.5D). This study shows that three separate plasmon modes (LA-D, LA-Q, and SA-D) at different resonance wavelengths can be selectively induced in the nanocrescent structure by controlling the wavelength and polarization of incident

light.

3.3.3 Quantitative Assessment of Polarization Anisotropy Values

A polar plot of the normalized extinction intensities of the long and short axis dipole resonance modes quantitatively illustrates the polarization dependence of the plasmonic nanocrescent (Fig. 3.6A). Extinction spectra were obtained for 445 nm diameter AuNCs at incident polarization angles from 0-360° and constant wavelength. For 2278 nm, the resonance wavelength of the LA-D mode, the plot shows maxima at 0° and 180°, indicating that selective induction of this mode should occur at either of the two directionally equivalent angles. The polar plot for 1284 nm, the maximum wavelength of the SA-D mode, shows maxima at 90° and 270°. These are the angles of maximum excitation for the SA-D mode and are orthogonal to those for the LA-D resonance mode. This plot demonstrates the selective induction of two distinct plasmon resonance modes with different resonance wavelengths by controlling the polarization angle of incident light, a manipulation of near field behavior through far field control.

I analyzed the relative optical response of the LA and SA dipole modes for 445 nm diameter AuNCs (Fig. 3.2) in order to provide further quantitative assessment of the polarization anisotropy of the NC structure. For this analysis, I modified the equations described by Wang *et al.* and Ha *et al.* that compare calculated and experimental anisotropy values.[26, 27] Wang *et al.* have shown that the polarization anisotropy, *A*, is proportional to the fourth power of the cosine (for LA polarization) or sine (for SA polarization) of any angle, θ, using the equation:[26]

$$A_{LA} = \frac{\cos^4(\theta) - \sin^4(\theta)}{\cos^4(\theta) + \sin^4(\theta)}. \quad (1)$$

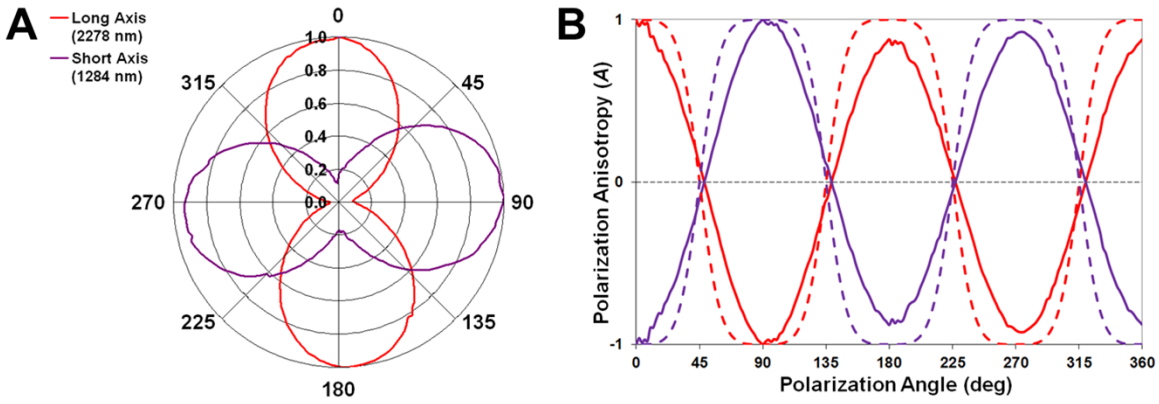

Figure 3.6. Polarization anisotropy of 445 nm diameter AuNCs. A) Polar plot of normalized extinction values for the LA-D (red) and SA-D (purple) resonance modes demonstrating anisotropy. B) Experimental (solid) and calculated (dashed) polarization anisotropy values (*A*) for LA-D (red) and SA-D (purple) resonances of same AuNC sample.
Modified from Reference 28.

To calculate theoretical A_{SA} values, the functions of sine and cosine are transposed. For true polarization direction dependence, $A = 1$. This equation gives the polarization angles at which selective excitation of a specific resonance mode should occur. To calculate polarization anisotropy using experimental data for the nanocrescent structure, eqn. 1 is modified to:[27]

$$A_{LA} = \frac{I_{LA} - I_{SA}}{I_{LA} + I_{SA}}, \tag{2}$$

where A_{LA} is the anisotropy of the long axis mode and I_{LA} and I_{SA} are the normalized intensities of the LA-D and SA-D resonance extinction values, respectively, at a common angle. The values are transposed to calculate the anisotropy of the short axis mode, A_{SA}. Again, for selective excitation of a specific resonance mode, A should be equal to 1 at the maximum excitation angle for that mode.

I used only the LA-D and SA-D resonance mode extinction values, remaining consistent with the axes defined in Figure 3.2B, to demonstrate the anticorrelation of these two modes at orthogonal polarization angles. Results for eqn. 1 show that selective induction should occur at 0° for the LA-D resonance mode and 90° for the SA-D resonance mode, corroborating what was predicted by simulation. Calculations using measured and normalized extinction values at 2278 nm (LA-D) and 1284 nm (SA-D) in eqn. 2 do, in fact, yield values of 1 at 0° and 90° for A_{LA} and A_{SA}, respectively (Fig. 3.6B). These calculated values support what was observed in the polar plot, that when incident light at the appropriate wavelength is polarized along the long axis of the nanocrescent the LA-D is selectively excited while the SA-D is not. Rotation of the polarization of the electric field across the short axis will not induce the SA-D because

the incident wavelength does not match the wavelength of that resonance mode. The anisotropy of the structure has been exploited to independently excite a single mode at a specific wavelength based on polarization controlled illumination.

3.3.4 Polarization Dependence of Nonlinear Microscopy

The polarization dependence of the nanocrescent can be further demonstrated using the nonlinear optical imaging processes of two-photon fluorescence (2PF) and second harmonic generation (SHG). In 2PF, two photons are absorbed, each with half the energy required for electronic excitation, whose combined energy can produce an excited state that emits radiation as the electron relaxes back to the ground state or fluoresces. SHG is similar in that the energy of the two photons is combined to generate a single output photon with twice the energy of the initial incident photons. Nonlinear processes are inherently weak and require high intensity laser light but the high intensity constraint of these processes can be overcome by utilizing the field enhancement of a plasmon resonance tuned to the excitation wavelength of the laser.

Gold nanocrescents with diameters of 215 nm support long and short axis dipole resonance modes with wavelengths of ~1100 nm and ~800 nm, respectively. The wavelength of the SA-D resonance mode overlaps that of the excitation wavelength of the Ti-sapphire laser used in the experimental setup (Fig. 3.1A) while the LA-D does not. Therefore, incident electric field polarization across the short axis can be used to enhance the two nonlinear processes while polarization across the long axis will not. Microscopy images of the AuNCs demonstrate that this is so (Fig. 3.7). The fluorescence and SHG intensities emitted by short axis polarization excitation are much greater than that of long axis polarization. These data provide additional evidence for the predicted anisotropic

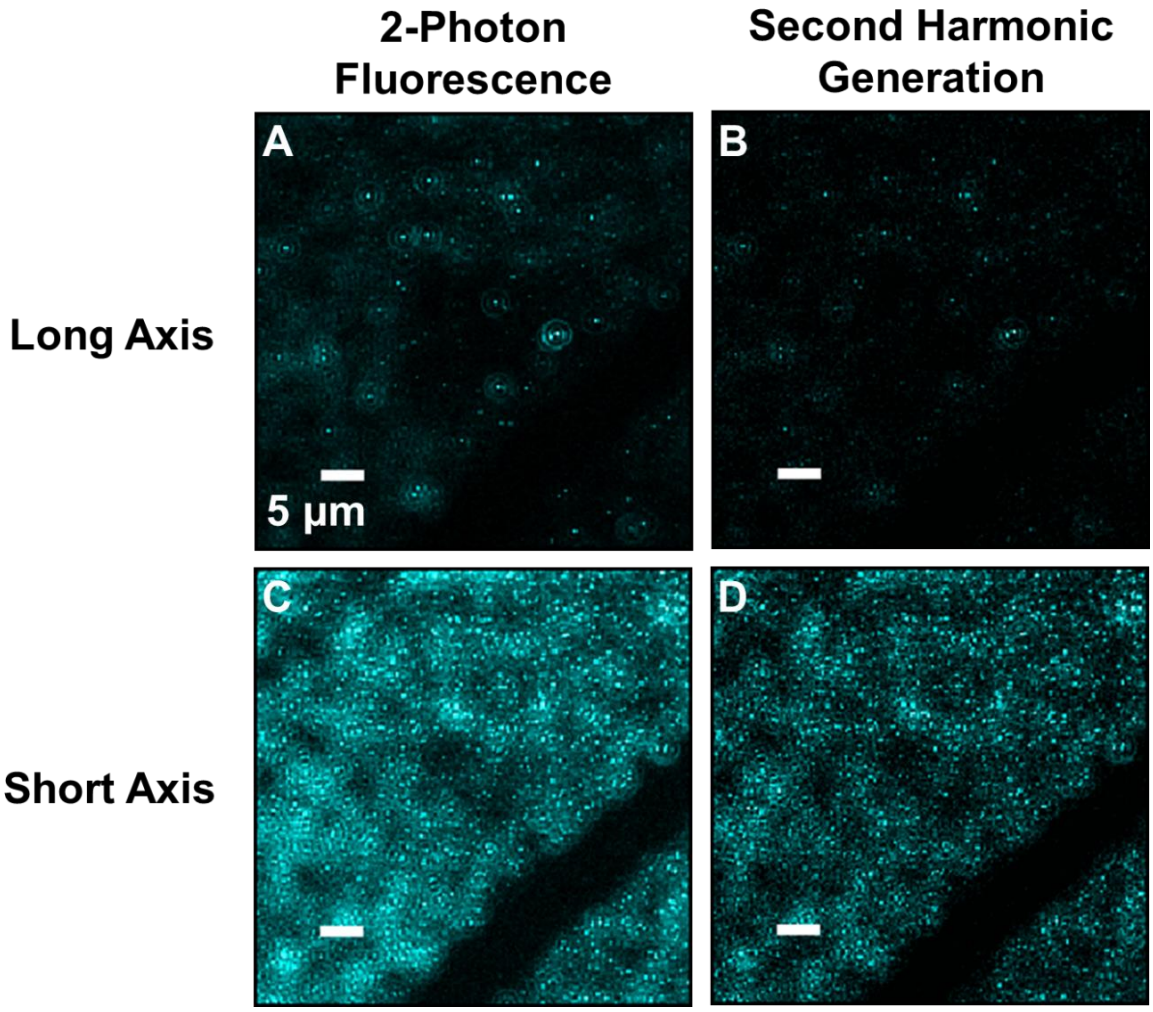

Figure 3.7. Polarization dependence of nonlinear microscopy imaging techniques utilizing surface enhancement effects of AuNCs. Long axis (A, B) and short axis (C, D) polarized excitation of two-photon fluorescence (A, C) and second harmonic generation (B, D). Both nonlinear processes demonstrate greater efficiency with overlapping wavelength of short axis resonance mode and excitation laser at 800 nm. Scale bars = 5 µm.

optical behavior of the asymmetric nanocrescent and indicate that the enhancement factor of the structure is large enough for use in nonlinear spectroscopy applications.

3.4 Conclusion

Multiple, polarization-dependent resonance modes can be excited in NCs that are well defined, reproducible, occur over a visible to near-infrared spectral range, and demonstrate polarization control over near field behavior. The anisotropy of the nanocrescent plasmon resonance modes has been observed in polarized extinction spectra as well as second harmonic generation and two-photon fluorescence imaging. Selective induction of the distinct modes can be achieved using specific wavelengths and electric field polarization of incident light, leading to unique patterns of near field enhancement resulting from the electron oscillations. Identifying and controlling the locations of hot spots could increase the effectiveness of plasmonic substrates in surface enhanced spectroscopic and microscopic techniques by directing analyte molecules to areas of highest field enhancement, initiating chemical reactions at precise surface locations, or tracking hot spot-bound reaction mechanisms as they occur. This polarization dependent control can also be applied to nonlinear optical techniques such as sum frequency generation by selectively enhancing either of the two incoming photons to increase the efficiency of output photon generation.

3.5 References

1. Alvarez-Puebla, R.; Liz-Marzán, L. M.; García de Abajo, F. J. Light Concentration at the Nanometer Scale. *J. Phys. Chem. Lett.* **2010,** *1,* 2428-2434.

2. Banik, M.; Nag, A.; El-Khoury, P. Z.; Rodriguez Perez, A.; Guarrotxena, N.; Bazan, G. C.; Apkarian, V. A. Surface-Enhanced Raman Scattering of a Single Nanodumbbell: Dibenzyldithio-Linked Silver Nanospheres. *J. Phys. Chem. C.* **2012,** *116,* 10415-10423.

3. Berweger, S.; Atkin, J. M.; Olmon, R. L.; Raschke, M. B. Adiabatic Tip-Plasmon Focusing for Nano-Raman Spectroscopy. *J. Phys. Chem. Lett.* **2010,** *1,* 3427-3432.

4. Dey, S.; Mirell, D.; Rodriguez Perez, A.; Lee, J.; Apkarian, V. A. Nonlinear Femtosecond Laser Induced Scanning Tunneling Microscopy. *J. Chem. Phys.* **2013,** *138,* 154202.

5. Barrow, S. J.; Funston, A. M.; Gomez, D. E.; Davis, T. J.; Mulvaney, P. Surface Plasmon Resonances in Strongly Coupled Gold Nanosphere Chains from Monomer to Hexamer. *Nano Lett.* **2011,** *11,* 4180-4187.

6. Jana, N. R.; Gearheart, L.; Murphy, C. J. Wet Chemical Synthesis of High Aspect Ratio Cylindrical Gold Nanorods. *J. Phys. Chem. B.* **2001,** *105,* 4065-4067.

7. Jana, N. R.; Gearheart, L.; Murphy, C. J. Wet Chemical Synthesis of Silver Nanorods and Nanowires of Controllable Aspect Ratio. *Chem. Commun.* **2001,** *7,* 617-618.

8. Im, S. H.; Lee, Y. T.; Wiley, B.; Xia, Y. Large-Scale Synthesis of Silver Nanocubes: The Role of HCl in Promoting Cube Perfection and Monodispersity. *Angew. Chem. Int. Ed.* **2005,** *44,* 2154-2157.

9. Deeb, C.; Zhou, X.; Miller, R.; Gray, S. K.; Marguet, S.; Plain, J.; Wiederrecht, G. P.; Bachelot, R. Mapping the Electromagnetic Near-Field Enhancements of Gold Nanocubes. *J. Phys. Chem. C.* **2012,** *116,* 24374-24740.

10. Hanarp, P.; Käll, M.; Sutherland, D. S. Optical Properties of Short Range Ordered Arrays of Nanometer Gold Disks Prepared by Colloidal Lithography. *J. Phys. Chem. B.* **2003,** *107,* 5768-5772.

11. Aizpurua, J.; Hanarp, P.; Sutherland, D. S.; Käll, M.; Bryant, G. W.; García de Abajo, F. J. Optical Properties of Gold Nanorings. *Phys. Rev. Lett.* **2003,** *90,* 057401.

12. Hulteen, J. C.; Treichel, D. A.; Smith, M. T.; Duval, M. L.; Jensen, T. R.; Van Duyne, R. P. Nanosphere Lithography: Size-Tunable Silver Nanoparticle and

Surface Cluster Arrays. *J. Phys. Chem. B.* **1999,** *103*, 3854-3863.

13. Haes, A. J.; Zhao, J.; Zou, S.; Own, C. S.; Marks, L. D.; Schatz, G. C.; Van Duyne, R. P. Solution-Phase, Triangular Ag Nanotriangles Fabricated by Nanosphere Lithography. *J. Phys. Chem. B.* **2005,** *109*, 11158-11162.

14. Hao, F.; Nehl, C. L.; Hafner, J. H.; Nordlander, P. Plasmon Resonances of a Gold Nanostar. *Nano Lett.* **2007,** *7*, 729-732.

15. Li, M.; Cushing, S., K.; Zhang, J.; Lankford, J.; Aguilar, Z. P.; Ma, D.; Wu, N. Shape-Dependent Surface-Enhanced Raman Scattering in Gold-Raman-Probe-Silica Sandwiched Nanoparticles for Biocompatible Applications. *Nanotechnology.* **2012,** *23*, 115501.

16. Bochenkov, V. E.; Sutherland, D. S. From Rings to Crescents: A Novel Fabrication Technique Uncovers the Transition Details. *Nano Lett.* **2013,** *13*, 1216-1220.

17. McLellan, J. M.; Li, Z.-Y.; Siekkinen, A. R.; Xia, Y. The SERS Activity of a Supported Ag Nanocube Strongly Depends on Its Orientation Relative to Laser Polarization. *Nano Lett.* **2007,** *7*, 1013-1017.

18. Tao, A. R.; Yang, P. Polarized Surface-Enhanced Raman Spectroscopy on Coupled Metallic Nanowires. *J. Phys. Rev. B.* **2005,** *109*, 15687-15690.

19. Zhao, Y.-P.; Chaney, S. B.; Shanmukh, S.; Dluhy, R. A. Polarized Surface Enhanced Raman and Absorbance Spectra of Aligned Silver Nanorod Arrays. *J. Phys. Chem. B.* **2006,** *110*, 3153-3157.

20. Koen, K. A.; Weber, M. L.; Mayer, K. M.; Fernandez, E.; Willets, K. A. Spectrally-Resolved Polarization Anisotropy of Single Plasmonic Nanoparticles Excited by Total Internal Reflection. *J. Phys. Chem. C.* **2012,** *116*, 16198-16206.

21. Ambjörnsson, T.; Mukhopadhyay, G.; Apell, S. P.; Käll, M. Resonant Coupling Between Localized Plasmons and Anisotropic Molecular Coatings in Ellipsoidal Metal Nanoparticles. *Phys. Rev. B.* **2006,** *73*, 085412.

22. Yoshida, K. -I.; Itoh, T.; Tamaru, H.; Biju, V.; Ishikawa, M.; Ozaki, Y. Quantitative Evaluation of Electromagnetic Enhancement in Surface-Enhanced Resonance Raman Scattering from Plasmonic Properties and Morphologies of Individual Ag Nanostructures. *Phys. Rev. B.* **2010,** *81*, 115406.

23. Bukasov, R.; Ali, T. A.; Nordlander, P.; Shumaker-Parry, J. S. Probing the Plasmonic Near-Field of Gold Nanocrescent Antennas. *ACS Nano.* **2010,** *4*, 6639-6650.

24. Bukasov, R.; Shumaker-Parry, J. S. Highly Tunable Infrared Extinction Properties of Gold Nanocrescents. *Nano Lett.* **2007,** *7,* 1113-1118.

25. Shumaker-Parry, J. S.; Rochholz, H.; Kreiter, M. Fabrication of Crescent-Shaped Optical Antennas. *Adv. Mater.* **2005,** *17,* 2131-2134.

26. Wang, G.; Sun, W.; Luo, Y.; Fang, N. Resolving Rotational Motions of Nano-Objects in Engineered Environments and Live Cells with Gold Nanorods and Differential Interference Contrast Microscopy. *J. Am. Chem. Soc.* **2010,** *132,* 16417-16422.

27. Ha, J. W.; Sun, W.; Wang, G.; Fang, N. Differential Interference Contrast Polarization Anisotropy for Tracking Rotational Dynamics of Gold Nanorods. *Chem. Commun.* **2011,** *47,* 7743-7745.

28. Cooper, C. T.; Rodriguez, M.; Blair, S.; Shumaker-Parry, J. S. Polarization Anisotropy of Multiple Localized Plasmon Resonance Modes in Noble Metal Nanocrescents. *J. Phys. Chem. C.* **2014,** *118,* 1167-1173.

CHAPTER 4

OPTICAL PROPERTIES OF PLASMONIC NANOCRESCENT ARRAYS FABRICATED BY CONTROLLED PLASMA ETCHING OF POLYSTYRENE NANOSPHERE TEMPLATES

4.1 Introduction

The unique optical near fields resulting from localized surface plasmon resonance (LSPR) in metallic nanostructures provide many benefits to spectroscopy and microscopy techniques. Not only do these enhanced near fields amplify spectroscopic signals, but they provide a way to control probe volumes and increase the spatial resolution and specificity of surface enhanced analytical techniques.[1-4] The organization of individual plasmonic particles into well-ordered arrangements is one way to potentially maximize these benefits of near field enhancement.[2-6] Higher densities of plasmonic nanostructures on a surface focus a greater portion of incident light to nanoscale probe volumes and greatly increase the probability of enhancing analyte signals.

Methods of nanoparticle organization vary depending on the initial method of structure formation (i.e., synthesis or fabrication) and add a new dimension to the tuning of optical properties and near-field distributions through control over structural features. Several approaches to the organization of colloidal nanoparticles have utilized selective chemistries for more efficient "hot spot" formation.[2, 6-12] These techniques take advantage

of specific (e.g., DNA hybridization) and spatially localized chemical reactions to induce dimerization and larger clustering of plasmonic nanostructures in a precise manner. While successful, controlling multiple reaction conditions is challenging and these techniques can be difficult to scale up. Fabrication-based approaches to plasmonic nanostructure organization are more easily scaled up for controlled spacing of a large number of nanostructures compared to current synthetic techniques, but can be more time consuming.[5, 13, 14] Top-down methods generally require additional steps to produce ordered nanostructure arrays; however, the process provides easier control over final nanostructure size and interparticle distances (i.e., the spacing between neighboring nanostructures).[14-19] For both synthetic and fabricated methods of formation, organized arrays introduce new particle interactions that need to be taken into consideration.[20-24] Decreasing interparticle distances can shift the plasmonic resonance wavelength or alter the distribution of near fields on the nanostructure surface and methods for investigating these effects need to be developed alongside organizational techniques.

Here, I demonstrate the fabrication of plasmonic arrays by adding a short plasma etching step to nanosphere template lithography (NTL), a simple, high-throughput approach for plasmonic nanostructure fabrication.[14, 24-26] Although focus is on the fabrication of nanocrescent arrays, this method could be used to prepare ordered arrangements of nanostructures with different shapes. I describe a simple method for the hexagonal close packing of polystyrene nanosphere templates which are shrunk via exposure to oxygen plasma.[27, 28] Etching of the polystyrene nanospheres allows for the fabrication of ordered nanostructure arrays by maintaining the positions and arrangement of the templates on the substrate while increasing the final interparticle distance without

adding significant time to the fabrication process.[28] I observed interesting changes in the physical properties of the polystyrene nanospheres resulting from oxygen plasma etching and discuss the consequential impact on the structural and optical properties of fabricated plasmonic nanostructures.

The shrinking technique can be used on templates with different initial diameters to fabricate plasmonic nanostructures with the same final size and different interparticle distances or vice versa to probe interparticle coupling and other optical responses of arrayed nanostructures. I present initial characterization of the optical properties of gold nanocrescent arrays and compare the plasmonic response to isolated and aggregated nanocrescents. Variations in the LSPR optical response of the different sample template types give insight into particle and electric field interactions. Peak shifting effects resulting from slight differences in size are well-known and omitted from this comparison.

4.2 Experimental Procedures and Discussion

4.2.1 Organization of Array Nanosphere Templates

A simple, two-step hexagonal close packing (HCP) technique was used to organize polystyrene template nanospheres on several different substrate surfaces. In the first step of the process, stock solutions of nanospheres in water were diluted to ~0.5% w/v with equal parts ethanol and water. Aliquots of 50 μL were then deposited on clean glass, CaF_2, or silicon substrates. The ethanol diluent provides excellent surface wetting for a majority of surfaces, resulting in higher surface coverage of close-packed nanospheres, and water helps control the rate of solvent evaporation, allowing sufficient time for the polystyrene nanospheres to self-assemble. By using equal volumes in the final dilution,

the entire surface of the substrates was wetted and utilized for templating and the solution evaporated at a rate that produced hexagonally close-packed monolayers of templates with high surface coverage (Fig. 4.1B).

When the ratio of ethanol: water was unequal or a dilution factor other than 1:5 was used, the resulting close packing was negatively affected (Fig. 4.1). When the solution percentage of water was either low (25%, Fig. 4.1A) or high (100%, Fig. 4.1D) multilayers of template nanospheres were produced as a result of fast solvent evaporation or partial surface wetting, respectively. These effects can be seen in the disorganization and multilayers of nanospheres in Figure 4.1A (low water concentration) and the stacked layers and low surface coverage in Figure 4.1D (high water concentration). The production of multilayers also occurred when the dilution factor was low (1:3, Fig. 4.1E), resulting in high nanosphere concentrations (~0.9% w/v) that formed multiple stacked layers with moderately organized nanospheres on the bottom and increasingly disorganized templates in the top layers. High water percentages (75%, Fig. 4.1C) and dilution factors (1:7, Fig. 4.1F) were also less ideal as they resulted in inadequate surface wetting or low nanosphere concentrations (~0.4% w/v), respectively. The SEM images reveal that these conditions resulted in monolayer patches rather than large areas of uniform coverage.

It was determined that a dilution factor of 1:5 (~0.5% w/v) with approximately equal concentrations of ethanol and water (Fig. 4.1B) produced the highest surface coverage of close-packed monolayers on all three experimental substrates. These optimal conditions resulted in an increased template density by a factor of ~100, from 0.036 nanospheres/μm^2 for isolated 505 nm templates to 3.9 nanospheres/μm^2 for arrayed

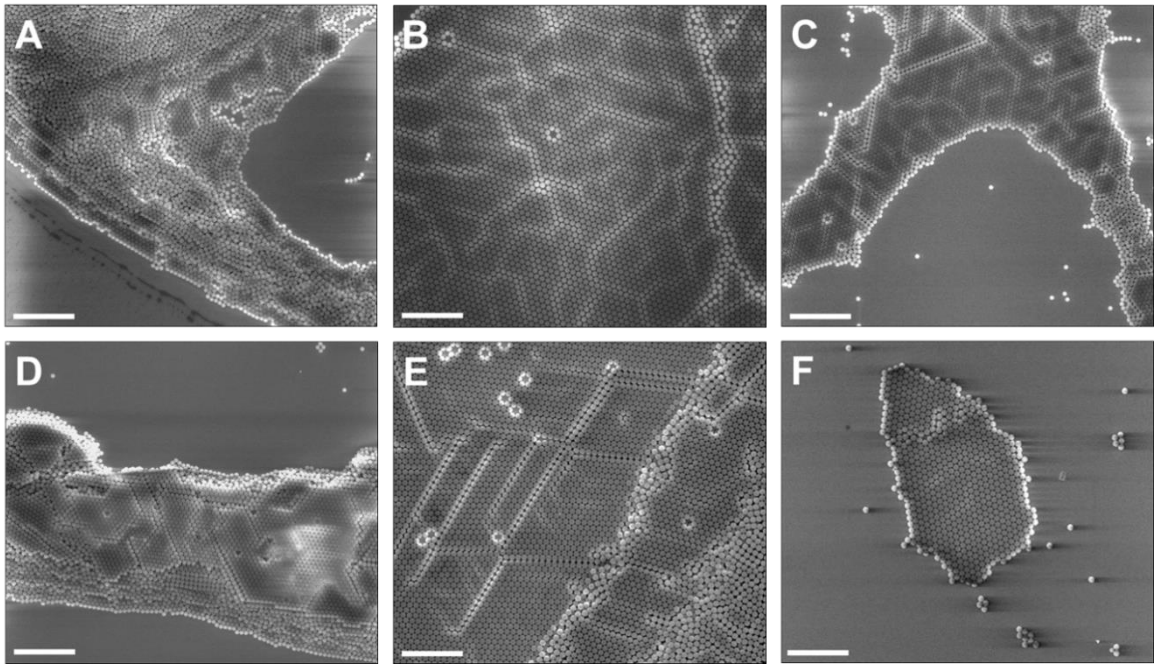

Figure 4.1. Effects of solvent concentration and dilution factor on self-assembly of hexagonal close packing of polystyrene nanospheres. SEM images of hexagonally close-packed (HCP) 505 nm polystyrene nanosphere templates on glass surfaces with varying water: ethanol volume ratios and dilution factors. A-D are ~0.5% w/v (1:5 dilution factor) with water: ethanol volume ratios of: A) 1:3 (25% H_2O), B) 1:1 (50% H_2O), C) 3:1 (75% H_2O), and D) 1:0 (100% H_2O). E and F both have water: ethanol ratios of 1:1 (50% H_2O) with dilution factors of: E) 1:3 (~0.9% w/v) and F) 1:7 (~0.4% w/v). Scale bars = 5 μm.

templates of the same size. Similar increases in template density were observed for other nanosphere diameters with the factor decreasing slightly for sizes much larger than 505 nm (i.e., >3 μm). While this method does not form a complete HCP monolayer across the entire surface as can be achieved with dip coating processes, it is a less time-consuming technique that can be highly useful for increasing the density of structures over a large area and investigating plasmonic coupling between structures.[29]

4.2.2 Effects of Etching Modification on Nanosphere Templates

In order to utilize the HCP templates for the fabrication of ordered nanocrescent arrays, the interparticle distances (measured from the outer edges of neighboring nanospheres) between the close-packed nanospheres had to be increased. This was accomplished by shrinking the polystyrene templates via oxygen plasma etching (Fig. 4.2).[27] Size reduction of the templates increases the interparticle distance which allows space for angled metal deposition, an essential step in nanocrescent fabrication, to be accomplished.[26] The etching step is also beneficial because the fabrication of different size plasmonic structures using nanosphere template lithography is limited by the size of available nanosphere templates. Uniform size reduction of the nanospheres provides a means to control the final template diameters and ultimately the size of the nanostructures for both study and tuning of the optical properties over a more comprehensive size range. This technique can be further utilized to produce templates with consistent size or interparticle distance while controllably altering the other variable to probe interparticle coupling and other optical responses of arrayed nanoparticles (Fig. 4.3).

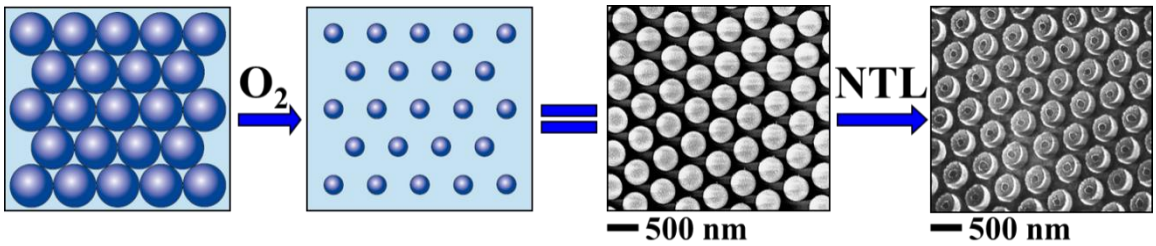

Figure 4.2. Schematic of nanosphere template size reduction and array fabrication. Polystyrene nanosphere templates are hexagonally close packed via self-assembly and then etched using oxygen plasma, allowing template diameter reduction while maintaining array organization. SEM images are of etched HCP nanosphere templates and the resulting nanocrescent array fabricated using nanosphere template lithography.

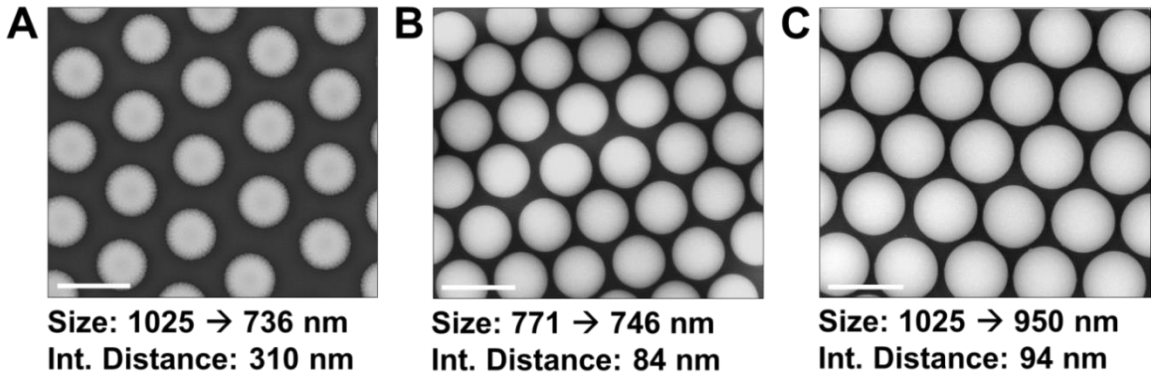

Figure 4.3. SEM images of hexagonally close packed polystyrene nanosphere templates demonstrating similar size (A, B) or interparticle distance (B, C) after oxygen plasma etching. Initial and final template diameters indicated below images achieved with etching conditions of: A) 100 W for 210 s, B) 75 W for 120 s, and C) 75 W for 120 s. Scale bars = 1 μm.

4.2.3 Nonlinear Template Etch Rate

In order to control the final template size, I investigated the shrinking rate of polystyrene nanospheres with various initial diameters (d_o). In these studies, I observed several unique characteristics of template etching. First, the etch rate of the nanosphere increases as the diameter is reduced, leading to a nonlinear relationship between the nanosphere diameter and etch time (Fig. 4.4).[27] This trend was observed for all nanosphere sizes at both power settings investigated, 75 W and 100 W, but is always more pronounced for the higher power. While the relationship is nonlinear, it is reproducible for nanospheres with the same initial diameter. That is, nanospheres from the same stock solution can be reproducibly reduced to a target diameter to produce a specific size of nanocrescent. This trend can be used to determine the etch time required to achieve specific final nanosphere diameters. However, the nonlinear relationship does increase the margin of error for achieving small target diameters because smaller diameters require longer etch times where the final shrinking rate is much faster than the initial rate (Fig. 4.4). Since the final nanosphere diameter and interparticle spacing are related, the variable etch rate impacts experiments dependent on control of interparticle distances as well. As a result, the etch rate variability has to be taken into account whether investigating templates with the same final diameter and different interparticle distances or a series of templates with similar spacing and nanospheres spanning a range of diameters.

4.2.4 Polystyrene Nanosphere Roughening- “Spiky Beads”

A second interesting observation during the template etch process was a roughening of the polystyrene surface when the nanospheres shrink to roughly half of the initial

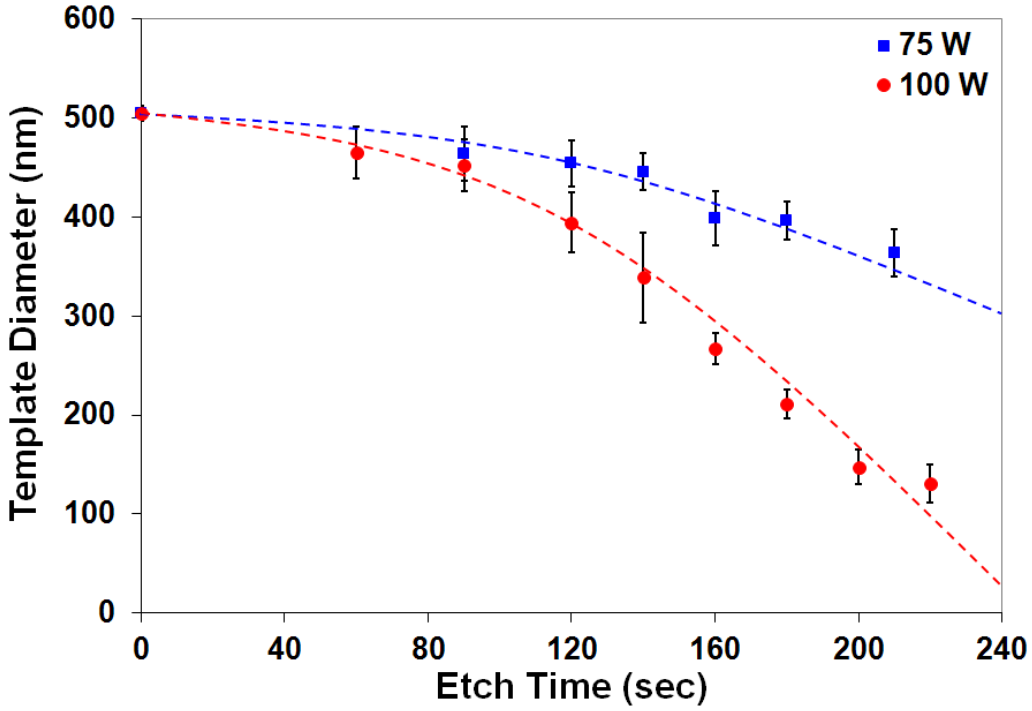

Figure 4.4. Etch rates of polystyrene nanospheres. Final template diameters for 505 nm polystyrene nanospheres shrunk at 75 W (blue squares) and 100 W (red circles) for varying lengths of time. Dashed curves are guides for distinction of variations in etch rates.

diameter (Fig. 4.5). Etching the templates past this point (i.e., very long etch times) resulted in spiky structures. These "spiky beads" have large interparticle spacings and very rough surfaces that could possibly be useful as surface enhanced spectroscopy substrates similar to the rough nanorod assemblies recently developed by Van Duyne and co-workers.[30] Experiments involving the deposition of very thin metal films onto highly roughened nanospheres, which mimic the rough nanorod assemblies, and investigation of the resulting optical properties are underway.

I observed the greatest surface roughening deformation of the nanospheres when templates were etched for long times at high power settings. Roughened nanospheres can also be seen in close examination of images published by other researchers who utilize the etching technique, but the effects were insignificant and the origin is not discussed.[24, 27, 28] In order to investigate the "spiky bead" effect, multiple HCP templates with d_o = 505 nm were etched for various lengths of time using a gas flow rate of 10 sccm O_2 and notable differences were observed at the two different power settings investigated, 100 W and 75 W. After long etch times (≥ 120 s) at 100 W, the polystyrene nanospheres had been reduced to a diameter of ~300 nm and began to show signs of inhomogeneous surface etching yielding "spiky beads" (Fig. 4.5C-F). After a 220 s etch at 100 W, the nanospheres were almost completely etched away (Fig. 4.5F). The roughening effect was not observed at 75 W until reaching etch times greater than 210 s, almost twice that of the transition point for 100 W (Fig. 4.5L). The difference in etch time required to begin roughening the nanosphere surfaces as well as the differences in amount of deformation are due not only to the power used but also the nonlinear etch rates. At 100 W, the nanospheres reach the critical size for roughening much faster than at 75 W and at 220 s

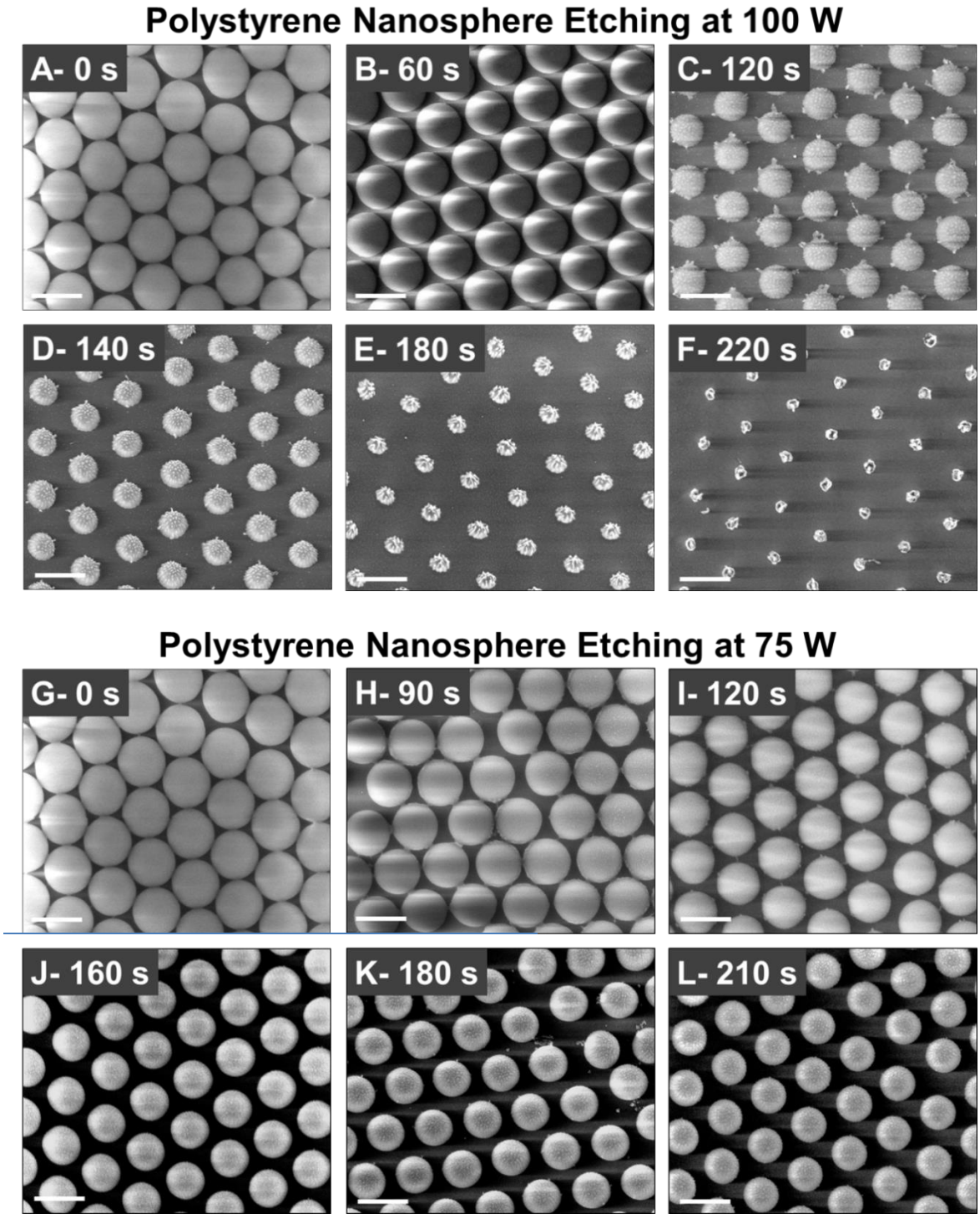

Figure 4.5. Nanosphere deformation resulting from long etch lengths. SEM images of hexagonally close packed 505 nm polystyrene nanosphere templates after oxygen plasma etching at 100 W (A-F) and 75 W (G-L) for time indicated in label. Scale bars = 500 nm.

the templates are almost completely destroyed while the sample etched at 75 W is barely beginning to roughen at that time point.

The "spiky bead" effect has been observed in both isolated and array etched nanosphere templates and attributed to effects of the oxygen plasma. However, the cause behind this nonuniform etching of the polystyrene nanospheres is still unknown. One potential hypothesis is that different crystalline domains with different etch rates are present in the nanospheres, causing nonuniform etching and surface roughening. In order to probe this possibility, Raman spectra of unetched nanospheres were compared to nanospheres etched for various lengths of time, including templates etched to less than half the original diameter (Fig. 4.6). If specific regions of the polystyrene nanospheres have a higher etch resistance to the oxygen plasma due to a specific stereochemistry, then spectral differences (specifically, peak shifts or differences in peak height ratios) should be observed as the lengths of the etch times increased and deformation occurred.

Polystyrene microspheres with d_o = 3 μm were hexagonally close packed on square glass coverslips following the same self-assembly procedure described in Chapter 2. The templates were etched in pairs for 9, 18, 27, and 36 min at 100 W power and 10 sccm flow rate. The long etch times were chosen to include templates etched to less than half the original diameter. After etching, the coverslips were placed on a confocal Raman microscope where a single microsphere was trapped and analyzed to obtain a Raman spectrum. This process was repeated for three microspheres on each coverslip including a nonetched sample for control. No significant spectral differences were observed, indicating that different crystalline domains of lower melting temperature are most likely not the cause of the surface roughening (Fig. 4.6). It was also determined that any

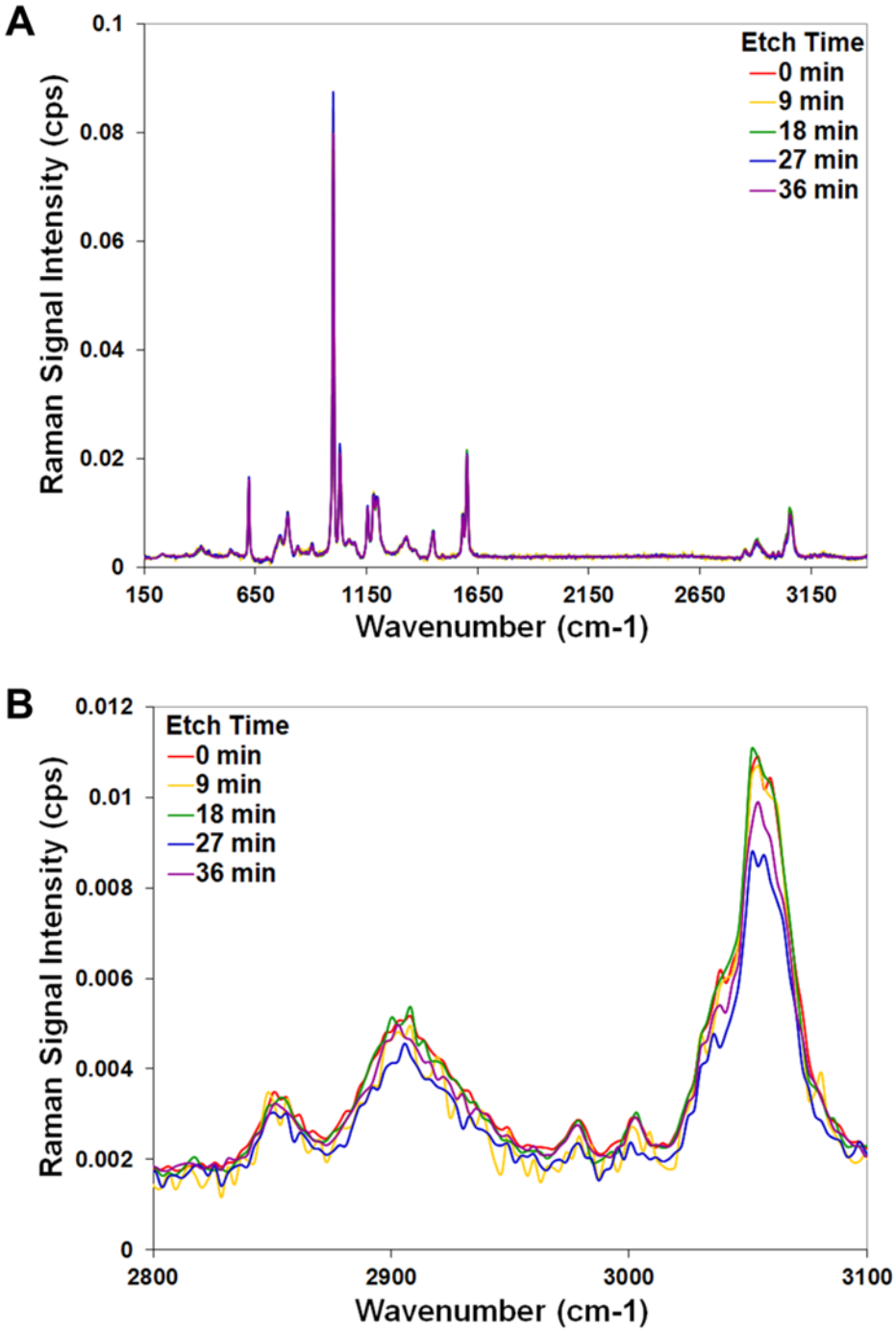

Figure 4.6. Comparison of Raman spectra for 3 µm polystyrene nanospheres etched for varying lengths of time. A) Full range of spectra obtained from individually trapped nanospheres etched for 0, 9, 18, 27, and 36 min. B) Closer view of spectral region (2800-3100 cm^{-1}) where peak intensities seem to show differences in A.

gradients or inhomogeneities present in the O_2 plasma are not at a small enough scale to produce the fine structures on the surface of the spiky beads resulting from the dry etch.

4.3 Results and Discussion

4.3.1 Spectral Differences between Isolated, Aggregated, and Arrayed Gold Nanocrescents

Despite surface roughening, the etching process was successful for the initial goal of increasing interparticle distances in order to fabricate nanocrescents from close-packed templates. When the etching technique was combined with NTL, gold nanocrescent (AuNC) arrays were successfully fabricated (Fig. 4.2). These nanostructures were compared to similarly sized isolated and aggregated gold nanocrescents fabricated using NTL without the additional etching step for differences in physical structure and optical response. As long as the nanospheres were not shrunk to less than half of the original diameter, ordered nanocrescent arrays could be fabricated through a simple modification of one fabrication step without impacting the structural integrity or plasmonic behavior of the nanocrescents. However, significant alterations to the physical structures of nanocrescents fabricated from over-etched nanospheres resulting from the deformation of the templates were observed and led to substantial changes in LSPR optical response.

4.3.2 Properties of Isolated Gold Nanocrescents

The isolated AuNC sample was fabricated from 348 nm diameter template nanospheres and produced dispersed nanocrescents with final diameters of 450 nm. Extinction spectra for this sample exhibit typical LSPR behavior for isolated AuNCs and are shown in Figure 4.7A. Four polarization-dependent plasmon resonance modes can be

Figure 4.7. Optical and structural properties of isolated (A/E), aggregated (B/F), and arrayed (C/G, D/H) gold nanocrescents. Extinction spectra and corresponding SEM images (scale bars = 500 nm) of AuNCs with diameters of: A/E) 450 nm, B/F) 325 nm, C/G) 410 nm, and D/H) 400 nm. AuNC arrays were fabricated from 505 nm beads etched at 100 W for 120 s (C/G) and 160 s (D/H). Long and short axis electric field polarization designated in E by red and blue arrows, respectively. Numbered labels in spectra correspond to distinct resonance modes described in text: 1- LA-D, 2- SA-D, 3- LA-Q, 4- OOP-D, 5- additional LA-D for aggregated nanocrescents, and 6- new SA resonance mode for distorted nanocrescents. Black arrows in B and D also indicate previously unobserved spectral peaks.

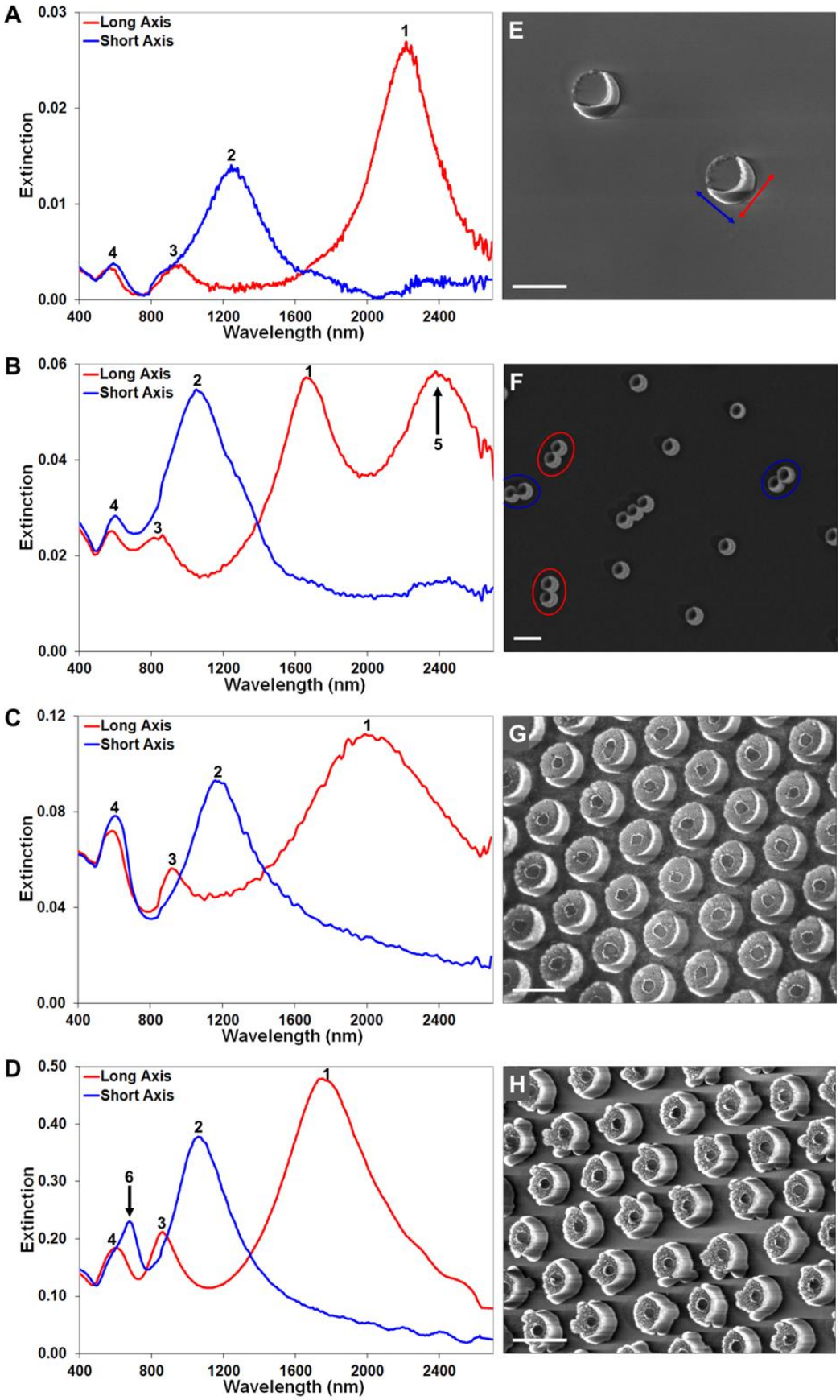
A
B
C
D
E
F
G
H
Long Axis
Short Axis
Extinction
Wavelength (nm)
0.00
0.01
0.02
0.03
0.04
0.06
0.08
0.10
0.12
0.20
0.30
0.40
0.50
400
800
1200
1600
2000
2400
1
2
3
4
5
6

induced in the structure, resulting in four distinct spectral peaks.[31] These are the long axis dipole (LA-D), short axis dipole (SA-D), long axis quadrupole (LA-Q), and out-of-plane dipole (OOP-D) resonance modes (labeled 1-4, respectively, in Fig. 4.7A). The LA-D is induced when the electric field of incident light is polarized across the long axis of the nanocrescent (red spectrum) and the highest amplitude spectral peak in the near IR (2230 nm) corresponds to this resonance mode. This polarization orientation also induces a higher order quadrupole mode represented by the lower amplitude peak (960 nm) in the red spectrum. The SA-D is induced when the electric field is polarized orthogonal to the long axis orientation (blue spectrum) and the second highest amplitude spectral peak (1250 nm) corresponds to this mode. The final peak located in the visible range (580 nm) corresponds to the OOP-D resonance mode. This peak shows a lack of polarization dependence for either polarization angle, producing similar peaks for either electric field orientation in the visible range.

4.3.3 Properties of Aggregated Gold Nanocrescents

The extinction spectra for AuNCs fabricated from unetched, but aggregated templates had a very noticeable difference from the spectra for isolated nanocrescents. The 243 nm diameter nanospheres used as templates produced 325 nm diameter AuNCs with the four expected peaks observed at blue-shifted wavelengths compared to the isolated 450 nm diameter AuNCs due to the smaller final size (Fig. 4.7A and B). However, an additional peak in the near-infrared spectral range appeared for electric field polarization along the long axis of the structure (indicated by black arrow in Fig. 4.7B).

Scanning electron microscope (SEM) images reveal that the template for this sample included aggregated nanospheres, resulting in a significant number of joined,

dimer nanocrescent structures after fabrication. Due to the angled metal deposition, the clustering only affects templates that have aggregated in a particular alignment with respect to the metal source. When the aggregation axis is parallel to the metal source, broken structures are fabricated due to the inability of metal to be deposited between templates in contact (blue outlines, Fig. 4.7F). When the aggregation axis of the nanospheres is perpendicular to the metal source, dimer nanocrescents with junctions occurring along the long axis of the structures are fabricated (red outlines, Fig. 4.7F). These connected structures behave like nanocrescents that are approximately two times larger in the long axis dimension than the isolated structures in the sample. The physical connection of the aggregated structures combined with the polarization dependence of the new, near-IR peak support the conclusion that the additional peak is a distinct long axis resonance mode for the larger dimer nanostructures and not the result of interparticle coupling. All other structural features of the nanocrescent (e.g., tip radius and backbone width) maintain the same dimensions as the isolated structures and short axis polarized spectra for aggregated structures are identical to spectra for isolated structures.

4.3.4 Properties of Arrayed Gold Nanocrescents

The spectra in Figure 4.7C are representative of the optical response of an AuNC array fabricated from etched nanospheres. The template was etched at 100 W for a short length of time (120 s) and produced nanospheres with reasonably smooth, spherical surfaces. The diameter decreased from 505 nm to 395 nm and resulted in 410 nm diameter nanocrescents. The smaller difference between the final nanosphere and nanocrescent diameters for this template compared to the isolated template is due to the thinner backbones of nanocrescents in the array resulting from the smaller interparticle

distance which restricted metal deposition. This thinner backbone appears to be the only structural difference between the array and isolated AuNCs (compare Fig. 4.7E and G), indicating that this method can be successfully used to fabricate arrays and investigate the relationship between nanocrescent diameter and interparticle distance.

The four resonance modes discussed previously for isolated nanocrescents were also induced in the arrayed nanocrescents and corresponding peaks are present in the extinction spectra (Fig. 4.7C). All four resonance modes were induced at wavelengths that follow the linear dependence of resonance frequency on AuNC diameter (Fig. 3.5D) with a LA-D at 2030 nm, SA-D at 1190 nm, LA-Q at 920 nm, and OOP-D at 610 nm and demonstrate polarization dependence.

Notable differences between the extinction spectra of the arrayed, isolated, and aggregated AuNCs, however, provide insight into the effects of the array organization and resulting plasmonic coupling. First, the peak amplitudes for the array samples are quadruple that of similar size isolated nanocrescents. This is to be expected with the increased number of structures on the substrate, but the resulting extinction efficiency of the nanocrescent, calculated using the method outlined by Bukasov and Shumaker-Parry and LA-D peak intensities, actually decreases from 2.4 to 0.5 when compared to isolated structures.[32] This decrease may be explained by the results of Kinnan and Chumanov which indicate that there is an optimal interparticle distance for a particular nanostructure size in order to achieve maximum extinction for plasmonic nanostructure arrays.[21] In general, this optimal interparticle distance is slightly larger than the size of the nanostructure due to retardation effects such as dephasing of plasmon oscillations that can occur between neighboring structures with small interparticle distances. For the 410

nm AuNC array, the interparticle distance is only one-fifth the size of the structure at 87 nm, which could result in significant dephasing and the decreased extinction efficiency of the array. However, the findings of Kinnan and Chumanov refer to coupled resonance modes. Although the LA-D resonance mode is not specifically a coupled resonance mode, with such a low ratio of interparticle distance to nanocrescent diameter for this AuNC array, dephasing effects could still cause a decrease in array extinction efficiency for this mode.

The second notable difference between the array and isolated spectra was a significant broadening of the two dipole peaks in the array spectra compared to corresponding peaks in the isolated spectra. The LA-D and SA-D resonance peaks were broader by factors of 2.7 and 1.5, respectively, when comparing the full-width half-maximum (FWHM) of the peaks in units of eV (Table 4.1). This peak broadening follows predicted and observed trends for decreasing interparticle distances and has also been attributed to retardation effects.[33, 34]

Finally, a significant difference between AuNCs fabricated from arrayed and aggregated templates supports the conclusion that an additional long axis resonance mode can be induced in dimer nanostructures due to the increased length of the structure. The additional low energy peak observed in the spectra for aggregated nanocrescents is notably absent in the spectra for arrayed nanocrescents (Fig. 4.7B and C). The absence of this peak in the array spectra confirms that the previously unobserved resonance mode is not due to interaction of overlapping fields of structures located extremely close to each other, but to structures with an elongated long axis.

The final set of spectra in Figure 4.7 was also obtained from an etched template

Table 4.1. Comparison of Isolated and Arrayed AuNC Optical Properties

Long Axis Dipole Resonance Mode

Diameter (nm)	Interparticle Distance (nm)	λ_{max} (nm)	Extinction Value	Extinction Efficiency	FWHM (eV)
450[a]	1272 ± 282	2230	0.027	7.88	0.097
410[b]	87 ± 6	2030 (2035)[c]	0.112	0.46	0.261
400[b]	83 ± 17	1760 (2000)[c]	0.486	1.99	0.202

Short Axis Dipole Resonance Mode

Diameter (nm)	Interparticle Distance (nm)	λ_{max} (nm)	Extinction Value	Extinction Efficiency	FWHM (eV)
450[a]	1272 ± 282	1250	0.015	4.22	0.278
410[b]	87 ± 6	1190 (1215)[c]	0.093	0.38	0.423
400[b]	83 ± 17	1060 (1200)[c]	0.378	1.55	0.398

[a]Isolated template.
[b]Arrayed template.
[c]Predicted isolated template AuNC resonance wavelength, calculated from linear dependence of λ_{max} on nanocrescent size, in parentheses for comparison of peak shifting due to array organization.[35]

fabrication resulting in an organized array and showed very interesting spectral differences from the other AuNC samples (Fig. 4.7D). The nanosphere templates for this sample were etched for 160 s and shrunk from 505 nm to 267 nm for a final nanocrescent diameter of 400 nm. This sample has a much larger difference between the final nanosphere and nanocrescent size than the previous array. While there was enough space between the shrunken polystyrene templates for metal deposition, this nanosphere array was over-etched during the shrinking process, resulting in less spherically-shaped templates. As can be seen in the SEM image, the nanocrescents fabricated from these templates were nonuniform and had distorted shapes with very wide backbones which increased the final overall diameter of the nanocrescent (Fig. 4.7H). In general, these structures were less similar in shape to their nearest neighbors than nanocrescents made from nanospheres etched for less time in either isolated or array form. Yet their non-uniformity still produced the four distinct plasmon resonance peaks with the highest amplitude of any sample, almost five times greater than the previous array (Fig. 4.7B) and roughly twenty times higher than the isolated AuNCs (Fig. 4.7A, Table 4.1). However, the resonance wavelength of each plasmon resonance mode for this array is blue-shifted compared to isolated AuNCs of the same size with a LA-D at 1760 nm, SA-D at 1060 nm, LA-Q at 870 nm, and OOP-D at 620 nm.[21, 33, 34] The plasmon resonance peaks of this less ideal array also demonstrate broadening in comparison to the isolated template, but surprisingly result in a slight narrowing of each peak compared to the previous array sample even though the nanocrescent diameters and interparticle distances are very similar for the two arrays.[33, 34] This narrowing is especially remarkable as additional peak broadening due to the nonuniformity of the nanocrescents would be

expected. Also surprisingly, the distorted structures maintained polarization dependence.

The preservation of polarization dependent behavior with less than ideal structures is interesting and led to an unexpected spectral difference. A new peak (indicated by black arrow in Fig. 4.7D) can be seen to the right of the out-of-plane plasmon resonance peak. This new peak is noticeably sharp and was observed in the visible region (680 nm) with short axis polarization for all HCP template samples prepared using long etch times (≥ 140 s) and resulting in distorted nanocrescents. The new peak is completely absent with long axis polarization but increases in amplitude as the polarization angle is changed for short axis excitation. Initially thought to be a sharpening and shifting of the out-of-plane peak, this new peak may actually correspond to another distinct plasmon resonance mode; possibly the short axis quadrupole (SA-Q) resonance mode which has not previously been observed in open, large tip gap (tip-to-tip distance) nanocrescents. The organization of the array may allow coupling of SA-Q resonance modes between AuNCs which can increase the amplitude of the corresponding LSPR peak that is typically absent or indifferentiable in extinction spectra for plasmonic nanocrescents. A similar peak amplitude increase was previously observed by Malynych and Chumanov for a weak quadrupole plasmon resonance mode in silver nanoparticles that was strengthened after organization of the structures into a two-dimensional array.[35] Alternatively, the previously unobserved resonance peak may be due to a new plasmon resonance mode present within the structure as a result of the distorted shape as compared to other nanocrescents that have been studied. As the out-of-plane peak is still present in the spectrum and can be seen as a shoulder to the left of the new peak, the assignment of this resonance mode to the new peak has been eliminated. The wavelength of the new peak

does not overlap any other known plasmon resonance modes for short axis polarization, further indicating that the new peak represents an additional, unique nanocrescent resonance mode.

4.4 Conclusions

Hexagonal close packing of polystyrene nanosphere templates for fabrication of plasmonic nanocrescents provides a way to prepare ordered arrays of these structures. Reduction of nanosphere template size via oxygen etching means that a broad range of nanostructure sizes and interparticle distances can be compared from a limited number of template nanospheres with different initial diameters. Plasmonic nanostructures of similar diameter with different spacing or different diameters with the same spacing can be easily fabricated and studied to better understand interparticle coupling effects and control the optical near field behavior in order to optimize extinction efficiencies and enhancements for spectroscopy and microscopy applications.

Comparison of the extinction spectra of AuNC arrays fabricated from etched templates to isolated AuNCs indicate that organized nanocrescents with predictable and tunable resonances can be successfully fabricated using this method. Additional comparison of these templates with aggregated AuNCs revealed two previously unobserved plasmon resonance modes. The mid-infrared peak observed in the spectra for aggregated structures suggests that the LSPR wavelengths of nanocrescents can be extended into the infrared spectral range and an additional peak in the visible range observed for imperfect structure arrays indicates the possibility of a higher order resonance mode for short axis excitation. Simulations are being done in order to better understand the behavior of these unique arrangements; in particular, to confirm the

assignment of a short axis quadrupole mode to the newly observed plasmon resonance peak for distorted nanocrescent structures. These calculations will also help clarify the interaction of optical near fields for neighboring nanocrescents as well as the correlation between diameter and interparticle spacing of the structures.

4.5 References

1. Alvarez-Puebla, R.; Liz-Marzán, L. M.; García de Abajo, F. J. Light Concentration at the Nanometer Scale. *J. Phys. Chem. Lett.* **2010,** *1,* 2428-2434.

2. Banik, M.; Nag, A.; El-Khoury, P. Z.; Rodriguez Perez, A.; Guarrotxena, N.; Bazan, G. C.; Apkarian, V. A. Surface-Enhanced Raman Scattering of a Single Nanodumbbell: Dibenzyldithio-Linked Silver Nanospheres. *J. Phys. Chem. C.* **2012,** *116,* 10415-10423.

3. Fabris, L. Bottom-up Optimization of SERS Hot-Spots. *Chem. Commun.* **2012,** *48,* 9346-9348.

4. Li, M.; Cushing, S. K.; Liang, H.; Suri, S.; Ma, D.; Wu, N. Plasmonic Nanorice Antenna on Triangle Nanoarray for Surface-Enhanced Raman Scattering Detection of Hepatitis B Virus DNA. *Anal. Chem.* **2013,** *85,* 2072-2078.

5. Abb, M.; Wang, Y.; Papasimakis, N.; de Groot, C. H.; Muskens, O. L. Surface-Enhanced Infrared Spectroscopy Using Metal Oxide Plasmonic Antenna Arrays. *Nano Lett.* **2013,** *14,* 346-352.

6. Pazos-Perez, N.; Wagner, C. S.; Romo-Herrera, J. M.; Liz-Marzán, L. M.; García de Abajo, F. J.; Wittemann, A.; Fery, A.; Alvarez-Puebla, R. A. Organized Plasmonic Clusters with High Coordination Number and Extraordinary Enhancement in Surface-Enhanced Raman Scattering (SERS). *Angew. Chem. Int. Ed.* **2012,** *51,* 12688-12693.

7. Mogilevsky, A.; Jelinek, R. Gold Nanoparticle Self-Assembly in Two-Component Lipid Langmuir Monolayers. *Langmuir.* **2011,** *27,* 1260-1268.

8. Sardar, R.; Heap, T. B.; Shumaker-Parry, J. S. Versatile Solid Phase Synthesis of Gold Nanoparticle Dimers Using an Asymmetric Functionalization Approach. *J. Am. Chem. Soc.* **2007,** *129,* 5356-5357.

9. Heuer-Jungemann, A.; Kirkwood, R.; El-Sagheer, A. H.; Brown, T.; Kanaras, A. G. Copper-Free Click Chemistry as an Emerging Tool for the Programmed Ligation of DNA-Functionalised Gold Nanoparticles. *Nanoscale.* **2013,** *5,* 7209-7212.

10. Sardar, R.; Shumaker-Parry, J. S. Asymmetrically Functionalized Gold Nanoparticles Organized in One-Dimensional Chains. *Nano Lett.* **2008,** *8,* 731-736.

11. Gao, B.; Rozin, M. J.; Tao, A. R. Plasmonic Nanocomposites: Polymer-Guided Strategies for Assembling Metal Nanoparticles. *Nanoscale.* **2013,** *5,* 5677-5691.

12. Zhao, Y.; Xu, L.; Liz-Marzán, L. M.; Kuang, H.; Ma, W.; Asenjo-García, A.; García de Abajo, F. J.; Kotov, N. A.; Wang, L.; Xu, C. Alternating Plasmonic

Nanoparticle Heterochains Made by Polymerase Chain Reaction and Their Optical Properties. *J. Phys. Chem. Lett.* **2013,** *4,* 641-647.

13. Gwinner, M. C.; Koroknay, E.; Fu, L.; Patoka, P.; Kandulski, W.; Giersig, M.; Giessen, H. Periodic Large-Area Metallic Split-Ring Resonator Metamaterial Fabrication Based on Shadow Nanosphere Lithography. *Small.* **2009,** *5,* 400-406.

14. Retsch, M.; Tamm, M.; Bocchio, N.; Horn, N.; Förch, R.; Jonas, U.; Kreiter, M. Parallel Preparation of Densely Packed Arrays of 150-nm Gold-Nanocrescent Resonators in Three Dimensions. *Small.* **2009,** *5,* 2105-2110.

15. Hanarp, P.; Sutherland, D. S.; Gold, J.; Kasemo, B. Control of Nanoparticle Film Structure for Colloidal Lithography. *Colloids Surf., A.* **2003,** *214,* 23-36.

16. Choi, S. -W.; Cheong, I. W.; Kim, J. -H.; Xia, Y. Preparation of Uniform Microspheres Using a Simple Fluidic Device and Their Crystallization into Close-Packed Lattices. *Small.* **2009,** *5,* 454-459.

17. Li, X.; Wang, T.; Zhang, J.; Yan, X.; Zhang, X.; Zhu, D.; Li, W.; Zhang, X.; Yang, B. Modulating Two-Dimensional Non-Close-Packed Colloidal Crystal Arrays by Deformable Soft Lithography. *Langmuir.* **2009,** *26,* 2930-2936.

18. Schweikart, A.; Pazos-Perez, N.; Alvarez-Puebla, R. A.; Fery, A. Controlling Inter-Nanoparticle Coupling by Wrinkle-Assisted Assembly. *Soft Matter.* **2011,** *7,* 4093-4100.

19. Saavedra, H.; Mullen, T. J.; Zhang, P.; Dewey, D.; Claridge, S.; Weiss, P. Hybrid Strategies in Nanolithography. *Rep. Prog. Phys.* **2010,** *73,* 036501.

20. Hanarp, P.; Käll, M.; Sutherland, D. S. Optical Properties of Short Range Ordered Arrays of Nanometer Gold Disks Prepared by Colloidal Lithography. *J. Phys. Chem. B.* **2003,** *107,* 5768-5772.

21. Kinnan, M. K.; Chumanov, G. Plasmon Coupling in Two-Dimensional Arrays of Silver Nanoparticles: II. Effect of the Particle Size and Interparticle Distance. *J. Phys. Chem. C.* **2010,** *114,* 7496-7501.

22. Zhao, L.; Kelly, K. L.; Schatz, G. C. The Extinction Spectra of Silver Nanoparticle Arrays: Influence of Array Structure on Plasmon Resonance Wavelength and Width. *J. Phys. Chem. B.* **2003,** *107,* 7343-7350.

23. Evanoff, D. D.; Chumanov, G. Synthesis and Optical Properties of Silver Nanoparticles and Arrays. *Chem. Phys. Chem.* **2005,** *6,* 1221-1231.

24. Vogel, N.; Fischer, J.; Mohammadi, R.; Retsch, M.; Butt, H. -J.; Landfester, K.; Weiss, C. K.; Kreiter, M. Plasmon Hybridization in Stacked Double Crescents Arrays Fabricated by Colloidal Lithography. *Nano Lett.* **2011,** *11,* 446-454.

25. Hulteen, J. C.; Treichel, D. A.; Smith, M. T.; Duval, M. L.; Jensen, T. R.; Van Duyne, R. P. Nanosphere Lithography: Size-Tunable Silver Nanoparticle and Surface Cluster Arrays. *J. Phys. Chem. B.* **1999,** *103,* 3854-3863.

26. Shumaker-Parry, J. S.; Rochholz, H.; Kreiter, M. Fabrication of Crescent-Shaped Optical Antennas. *Adv. Mater.* **2005,** *17,* 2131-2134.

27. Haginoya, C.; Ishibashi, M.; Koike, K. Nanostructure Array Fabrication with a Size-Controllable Natural Lithography. *Appl. Phys. Lett.* **1997,** *71,* 2934-2936.

28. Vogel, N.; Goerres, S.; Landfester, K.; Weiss, C. K. A Convenient Method to Produce Close- and Non-close-Packed Monolayers using Direct Assembly at the Air–Water Interface and Subsequent Plasma-Induced Size Reduction. *Macromol. Chem. Phys.* **2011,** *212,* 1719-1734.

29. Dimitrov, A. S.; Nagayama, K. Continuous Convective Assembling of Fine Particles into Two-Dimensional Arrays on Solid Surfaces. *Langmuir.* **1996,** *12,* 1303-1311.

30. Greeneltch, N. G.; Blaber, M. G.; Henry, A. -I.; Schatz, G. C.; Van Duyne, R. P. Immobilized Nanorod Assemblies: Fabrication and Understanding of Large Area Surface-Enhanced Raman Spectroscopy Substrates. *Anal. Chem.* **2013,** *85,* 2297-2303.

31. Cooper, C. T.; Rodriguez, M.; Blair, S.; Shumaker-Parry, J. S. Polarization Anisotropy of Multiple Localized Plasmon Resonance Modes in Noble Metal Nanocrescents. *J. Phys. Chem. C.* **2014,** *118,* 1167-1173.

32. Bukasov, R.; Shumaker-Parry, J. S. Highly Tunable Infrared Extinction Properties of Gold Nanocrescents. *Nano Lett.* **2007,** *7,* 1113-1118.

33. Chumanov, G.; Sokolov, K.; Cotton, T. M. Unusual Extinction Spectra of Nanometer-Sized Silver Particles Arranged in Two-Dimensional Arrays. *J. Phys. Chem. B.* **1996,** *100,* 5166-5168.

34. Haynes, C. L.; McFarland, A. D.; Zhao, L.; Van Duyne, R. P.; Schatz, G. C.; Gunnarsson, L.; Prikulis, J.; Kasemo, B.; Käll, M. Nanoparticle Optics: The Importance of Radiative Dipole Coupling in Two-Dimensional Nanoparticle Arrays. *J. Phys. Chem. B.* **2003,** *107,* 7337-7342.

35. Malynych, S.; Chumanov, G. Light-Induced Coherent Interactions between Silver Nanoparticles in Two-Dimensional Arrays. *J. Am. Chem. Soc.* **2003,** *125,* 2896-2898.

CHAPTER 5

LOCALIZED SURFACE PLASMON RESONANCES OF GOLD AND SILVER NANOCRESCENTS IN THE INFRARED SPECTRAL RANGE

5.1 Introduction

The localized surface plasmon resonance (LSPR) behavior of noble metal nanostructures leads to spatial localization of electromagnetic fields,[1-6] enhanced spectroscopy signals,[7-9] and increased resolution in microscopy techniques.[10-12] A large majority of plasmonic nanostructures exhibit plasmon resonances in the visible to near-infrared (400-1200 nm) spectral range and are utilized in applications such as surface enhanced Raman spectroscopy (SERS)[13-15] with excitation wavelengths in that range or photovoltaics for enhancement of light absorption in the visible region.[16, 17] In contrast, fewer investigations have focused on plasmonic effects in the broad infrared region despite the potential for enhancing the sensitivity of infrared-based spectroscopy measurements, impacting thermal imaging methods, and improving photovoltaic systems by manipulating the scattering and absorption of light across a broader spectral range.[18-20]

One reason for the limited exploration of plasmonic behavior in the infrared region is simply the lack of IR-active plasmonic nanostructures. A few materials approaches have been successful in extending the plasmon resonances of small metal nanoparticles to the infrared range.[20-24] For example, Enders *et al.* utilized submonolayer coverage of gold

seed nanoparticles on Si attenuated total reflection (ATR) crystal substrates to grow gold-island films with plasmonic resonances in the mid-infrared range.[21] However, island films lack structural specificity and therefore control over near field behavior. More commonly, access to the infrared spectral region is achieved by utilizing interparticle interactions resulting from ordered nanoparticle arrangements to produce coupled LSPR modes at red-shifted wavelengths compared to the plasmon resonances of the isolated particles. For example, Le *et al.* observed broadband absorption across a large region of the infrared spectral range for close-packed nanoshell arrays which exhibit superradiant behavior in close proximity.[22] However, requirements and substrate preparation for coupling plasmonic modes can be challenging and the IR plasmon resonance disappears with increasing interparticle distance (i.e., individual particle behavior dominates with the loss of plasmon coupling).

A more easily controlled method for fabricating IR-active plasmonic nanostructures is to simply increase the dimensions of the individual structures. The relationship between nanostructure size and resulting LSPR wavelength has been demonstrated for several shapes including spheres,[25, 26] rods,[27, 28] triangles,[29] and crescents.[30] As the size of the nanostructure increases, the LSPR wavelength red-shifts to lower energies. Theoretically, plasmon resonances in the infrared spectral range should thus be observed for larger metal nanostructures as long as the structural dimensions are smaller than the free-space wavelength of incident light. However, this constraint becomes problematic when trying to control structural features to manipulate the local field behavior on a size scale regime that is smaller than what can be easily achieved by micron-scale fabrication methods, especially in terms of achievable aspect ratios with incorporation of nanoscale

features and specific shape configurations. Also, as plasmonic structures are scaled up in size, they lose their localized behavior and, depending on the free-space wavelength of the incident light, LSPR cannot be induced within the visible to infrared spectral window. The critical dimensions for coupling with specific frequencies of light are most likely different for each shape and determine whether the localized surface plasmon resonances induced in the nanostructure can be extended into the infrared region. One structure that maintains nanoscale behavior even as the length extends into the micron range is the nanorod.[27, 31] Because of the high aspect ratio (microscale length: nanoscale width), plasmonic nanorods support LSPR responses that extend out into the infrared region. This extension increases the spectral range and broadens the potential utility of the particles for IR applications.[32, 33] Nanorods (or nanowires) fabricated using electron-beam lithography have demonstrated plasmon resonances in the mid-IR region but with a limited range of coupling with incident illumination.[34] This shifts the applicable LSPR wavelength, but limits the opportunities for simultaneous signal enhancement over a broad range of wavelengths available from plasmon coupling in ordered nanostructure arrays.

Nanocrescents (NCs) exhibit plasmonic behavior similar to nanorods with plasmon resonance modes in the infrared. Bending and narrowing the long nanorod structure into a crescent shape increases the asymmetry, allowing for the induction of additional, higher order modes and a higher confinement of electron density to very small dimensions (tips) for large enhancement of local electric fields. The behavior of the NC is unique as the diameter of the structure can be extended into the micron range while the width, thickness, and tip radius remain on the nanoscale dimension, producing high aspect

ratios.[35, 36] I investigated the optical behavior of NCs with diameters up to 3 μm that exhibited LSPR wavelengths beyond 8 μm. Not only do NCs support plasmon resonances spanning an extended wavelength range into the infrared region, but the structures also maintain polarization-dependent plasmon resonances as well. This polarization anisotropy allows for the selective excitation of specific plasmon resonance modes over a visible to infrared range in a single nanostructure.

Large diameter NCs with plasmon resonances in the mid-infrared spectral region are currently being investigated as substrates for surface-enhanced sum frequency generation (SFG) spectroscopy. Preliminary results from these experiments show modest signal enhancement resulting from incident light coupling with nanocrescent plasmon resonance modes which can be increased by further optimization of the structure and increased coupling, or greater overlap, between the wavelengths of incident light and plasmon resonance modes.

5.2 Experimental Procedures

5.2.1 Sum Frequency Generation Spectroscopy

Large diameter silver nanocrescents (AgNCs) with infrared frequencies were investigated as surface enhancing substrates for sum frequency generation (SFG) spectroscopy. Sum frequency refers to the process of two input photons generating a single output photon with energy equal to the sum of the incoming photons. As a nonlinear technique, SFG has a high intensity requirement for output photon generation that can be overcome when successfully coupled to an appropriately tuned, field enhancing plasmonic resonance. Overlap of the wavelength of the infrared laser with the LSPR wavelength of a nanocrescent enables probing of mid-infrared molecular

vibrations. Silver nanocrescents with diameters of 2.05 μm exhibited a broad long axis dipole resonance mode at 6680 nm which was used to enhance the intensity of a low power (<5 mW) infrared laser at 6.2 μm and probe the carbonyl stretch of 4-mercaptobenzoic acid (Fig. 5.1B).

The schematic for the SFG microscope setup is shown in Figure 5.1A.[37] The energies of the two different input photons from the optical parametric oscillator (OPO) light source are visible (632 nm) and infrared (6.2 μm). The incident light paths include a series of lenses and mirrors that collimate and focus the two beams on the sample surface as well as band-pass filters that eliminate light of undesired wavelengths generated by the OPO. A 4-mercaptobenzoic acid functionalized AgNC sample was illuminated in reflection mode using a 0.65 NA objective lens with the SFG and local oscillator (LO) signals collected by a photomultiplier tube.

5.3 Results and Discussion

5.3.1 Calculations for Polarization-Dependent Mid-IR Plasmon Resonance Modes

Previous studies of gold and silver nanocrescents (AuNCs and AgNCs, respectively) have focused on structures with small aspect ratios and diameters less than 500 nm.[6, 30, 38-40] Calculated extinction spectra and near field distributions for large diameter AuNCs (>500 nm) predict that crescent-shaped plasmonic structures will continue to support localized plasmonic resonances, maintain polarization dependent LSPR behavior, and have mode-dependent near field enhancement distributions similar to smaller nanocrescents (Fig. 5.2).[6] The optical response of 1.10 μm diameter plasmonic AuNCs calculated using finite-difference time-domain (FDTD) methods is shown in the

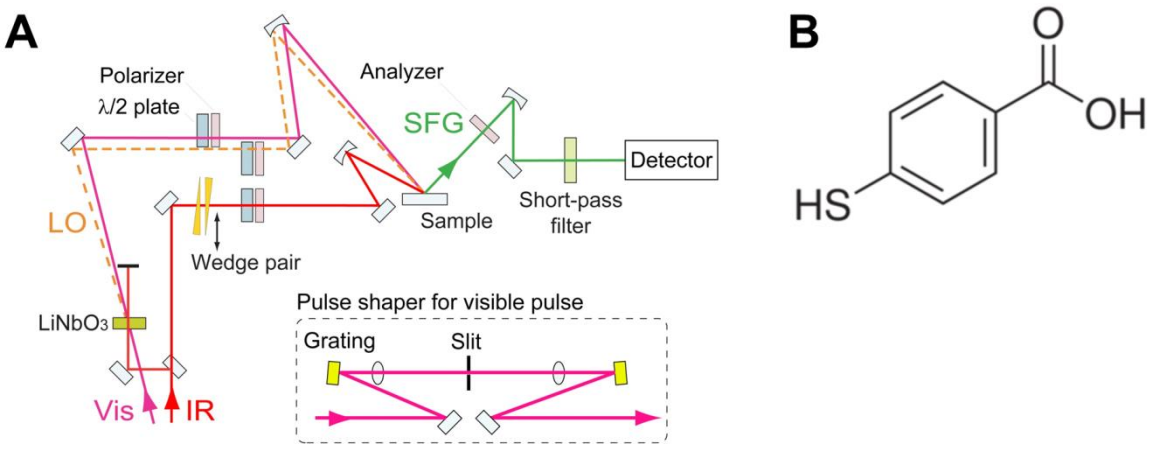

Figure 5.1. Experimental design for surface-enhanced sum frequency generation (SFG) spectroscopy. A) Schematic of experimental setup; LO- local oscillator.[37] Silver nanocrescents were used to enhance the infrared laser intensity at the sample surface for greater efficiency of the nonlinear optical process. B) Structure of 4-mercaptobenzoic acid.

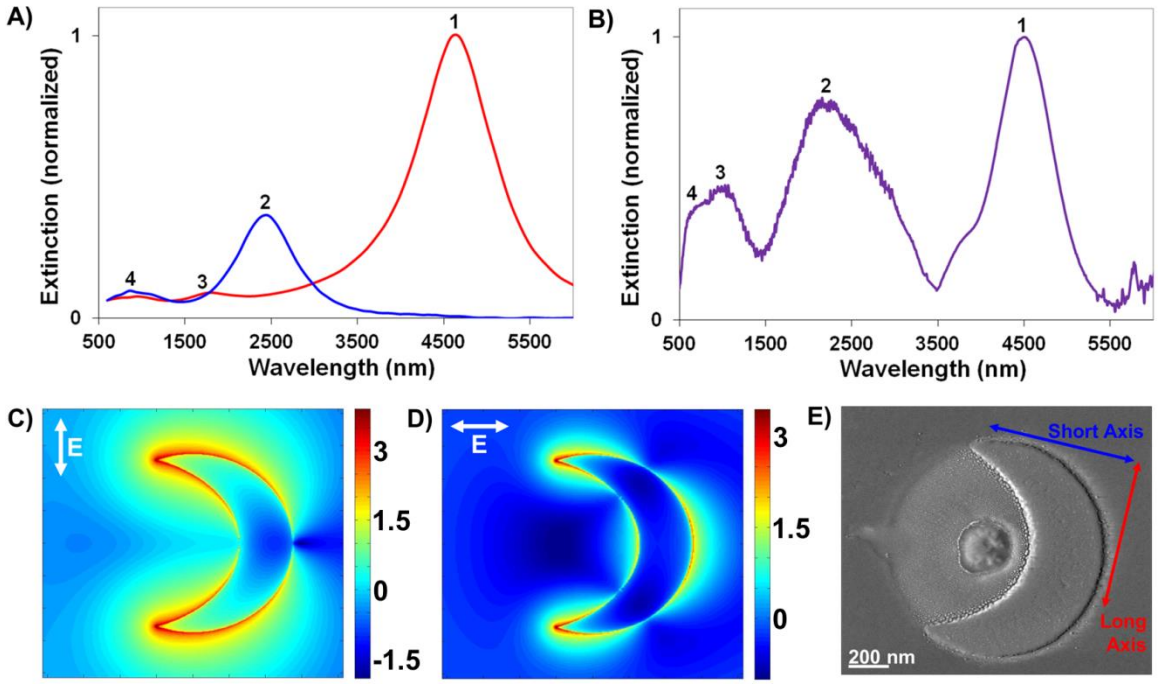

Figure 5.2. Calculated and experimental extinction spectra of large diameter AuNCs. A) Calculated extinction spectra for 1.10 μm diameter AuNCs with electric field polarized across the long axis (red) and the short axis (blue). B) Unpolarized extinction spectra of same size AuNCs measured by using both UV-Vis-NIR and FTIR instruments. The normalized spectra obtained from the two instruments were combined at the wavelength position of 2950 nm. NC resonance modes and corresponding peaks in (A) and (B) labeled as: 1) LA-D, 2) SA-D, 3) LA-Q, and 4) OOP-D, corresponding to descriptions in text. C, D) Calculated near field enhancement (I/I_o) of 1.10 μm diameter AuNC for LA-D (C) and SA-D (D) resonance modes. White arrows indicate polarization of electric field and intensity scales are logarithmic. E) Electron micrograph of 1.10 μm AuNC. Orientation of long and short axis polarization with respect to NC structure illustrated with red and blue arrows, respectively.

simulated spectra in Figure 5.2A. Four unique LSPR modes are identified and labeled in the spectra. Each of the plasmon resonance modes can be selectively induced by controlling the wavelength of incident light and polarization of the electric field with respect to the orientation of the NC structure (Fig. 5.2E).[6] In the calculated spectra, the lowest energy peak in the infrared region (4670 nm) corresponds to a dipole mode induced when the incident electric field is polarized across the long axis (LA) of the structure. The simulation of the near field distribution for this long axis dipole (LA-D) mode shows the highest calculated enhancement for any of the NC resonance modes (Fig. 5.2C). Polarization across this axis also induces a long axis quadrupole (LA-Q) resonance mode with a corresponding low amplitude peak located in the near-infrared region (1790 nm). Rotating the electric field polarization to induce an electron density oscillation across the short axis (SA) of the NC (orthogonal to LA polarization) produces a short axis dipole (SA-D) mode with the corresponding extinction peak located in the near-infrared region (2470 nm). The calculated near field for this resonance mode shows a more delocalized near field distribution with slightly smaller maximum field enhancement (Fig. 5.2D). The final plasmon peak in the visible range of both extinction spectra (710 nm) corresponds to a largely polarization-independent, out-of-plane dipole (OOP-D) resonance mode. The charge density oscillation for this mode is perpendicular to the plane in which the other three plasmon resonances occur. The wavelength of this resonance may be tuned by changing the thickness of the NC, but because all structures discussed in this chapter are 50 nm thick, the OOP-D spectral peak is always located in the visible range.

5.3.2 Experimental Verification of Mid-IR Plasmon Resonance Modes

In order to investigate this predicted extension of nanocrescent plasmon resonances into the mid-infrared spectral range, I fabricated large diameter nanocrescents using polystyrene microsphere templates in the nanosphere template lithography (NTL) fabrication process. Briefly, the fabrication process involves angled metal deposition with respect to the substrate covered with dispersed spherical polystyrene templates followed by a perpendicular plasma etch that produces crescent-shaped structures.[41] A representative large AuNC comparable in size to the model used in the simulation is shown in Figure 5.2E. Ensemble-based UV-Vis-NIR and IR extinction spectroscopy measurements were normalized and combined in order to characterize the optical properties of the NC structures (Fig. 5.2B). The unpolarized extinction spectrum obtained experimentally for the 1.10 μm diameter AuNC exhibits LSPR behavior similar to the predicted optical response and shows that large diameter NCs support LSPR modes in the mid-infrared region. The peaks corresponding to the four distinct resonance modes span a broad spectral range from the visible well into the infrared with a LA-D resonance peak at 4580 nm, SA-D at 2280 nm, LA-Q at 1050 nm, and OOP-D at 720 nm. This broad optical range is due to the structural feature dimensions which are on both the microscale and the nanoscale with an NC diameter of 1.10 μm, thickness of 50 nm, backbone width of 365 nm, and tip radius of 32 nm. Even though the length dimension (diameter) of the structure is extended past the nanoscale regime, localized plasmons are supported due to the nanoscale dimensions of the structural features which result in higher aspect ratios. As a result of the scaling up of the structure, the wavelengths of the different plasmon

resonance modes are red-shifted into the mid-infrared spectral region.

While these larger NCs demonstrate plasmonic behavior that extends into the mid-infrared spectral region, the plasmon resonance wavelengths are still not as red-shifted as those reported for very long nanorods with $\lambda_{res} \approx 10$ μm for lengths of 2.55 μm.[34] I explored the limits of the localized, nanoscale plasmonic behavior of both gold and silver NCs by probing the optical response of larger diameter NCs. This was accomplished by implementing the NTL fabrication procedure with larger microsphere templates. This resulted in AuNCs and AgNCs with final diameters ranging from 1.10-3.25 μm. The optical response of these NCs show that the structures continue to exhibit localized plasmon resonances with the longer wavelength dipole resonances red-shifted as far as 11.1 μm. The extinction spectra for AuNCs with diameters of 2.05 μm and 3.25 μm and AgNCs with diameters of 2.00 μm and 3.13 μm are shown in Figure 5.3. These large diameter nanocrescents all have backbone widths less than 700 nm, tip radii less than 100 nm, and thicknesses of 50 nm, maintaining these nanoscale dimensions as the diameter and resultant aspect ratio increased. For the smaller diameter (~2 μm) AuNCs and AgNCs, LSPR peaks corresponding to the long and short axis dipole resonance modes have red-shifted far from the visible-NIR boundary (Fig. 5.3A, C). The SA-D and LA-D plasmon resonance wavelengths for both AuNCs and AgNCs are located in the mid-infrared range at ~3810 nm and ~7580 nm, respectively. The peaks are red-shifted even further for the ~3 μm diameter structures (Fig. 5.3B, D). The single peak in each spectrum corresponds to the SA-D resonance mode which now appears further into the mid-IR at ~5760 nm.

All plasmon peak assignments discussed so far are based on simulations and

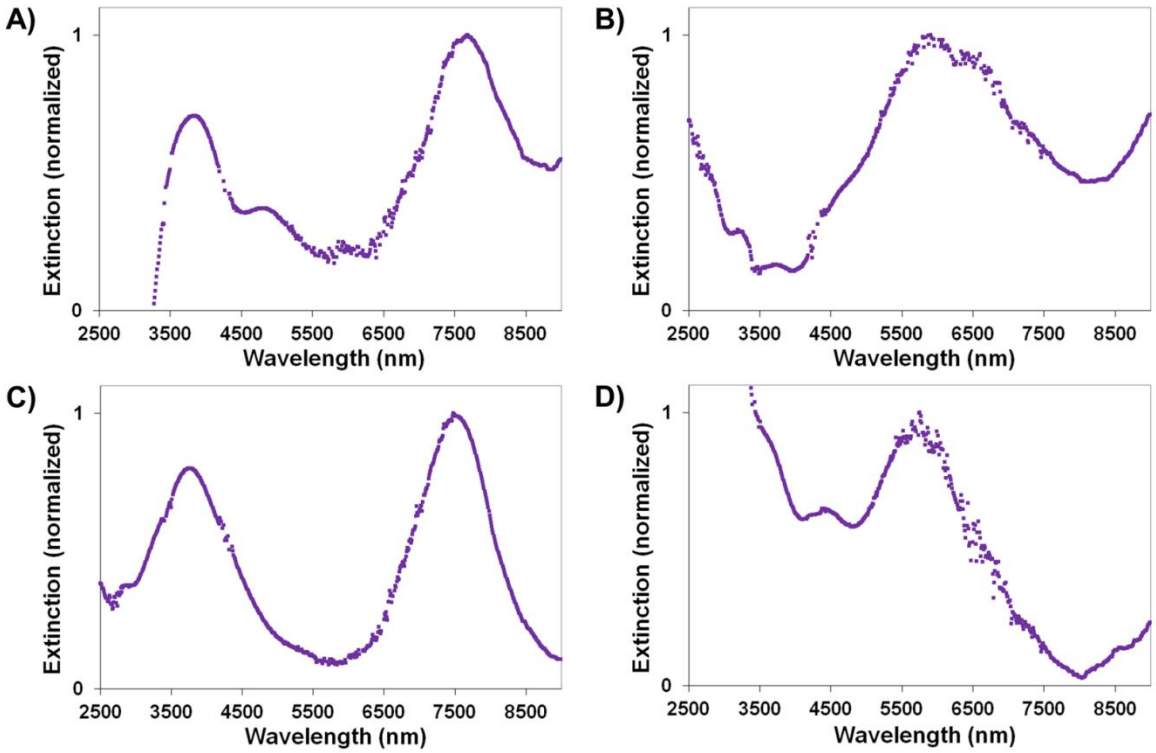

Figure 5.3. Unpolarized FTIR extinction spectra of large diameter AuNCs and AgNCs. A) Two μm diameter AuNCs, B) 3.25 μm diameter AuNCs, C) 2.00 μm diameter AgNCs, and D) 3.13 μm diameter AgNCs. The optical transparency of CaF_2 substrates decreases substantially approaching 10500 nm; the wavelength range of the extinction spectra is therefore limited to 2500-9000 nm to show the peaks of interest with minimal spectral artifacts.

previous observations of LSPR behavior for the NC structure. The resonance wavelengths follow the linear trends of each plasmon resonance mode that exhibit wavelength dependence on NC diameter (Fig. 5.4).[6, 30, 36] We can use these trends not only for peak assignments, but also to predict the wavelengths of the LA-D peaks for the ~3 μm diameter NCs. The LA-D plasmon resonance modes for both AuNCs and AgNCs are induced at a wavelength beyond the optical window of the CaF_2 substrate that was used specifically for its transparency over an extensive optical range. By using the linear relationship of the LSPR wavelength and NC diameter shown in Figure 5.4, I calculated that the LA-D resonances for the 3.25 μm diameter AuNCs and 3.13 μm diameter AgNCs should occur at 11.1 μm and 10.8 μm, respectively (Table 5.1).

The relationships between the LSPR wavelengths of different modes and nanocrescent diameters shown in Figure 5.4 demonstrate the observed plasmon resonances which, for the LA-D and SA-D plasmon modes, extend well into the mid-infrared spectral region. The observed linear dependence of the plasmon resonance spectral position on NC diameter for both Au and Ag illustrates the predictable and tunable nature of the plasmonic response of the NC structures.

5.3.3 Polarization Dependence of Mid-IR Plasmon Resonance Modes

The structural asymmetry of the NC leads to polarization anisotropy, which is also maintained as the size of the structure is increased and can be used to target a broad range of wavelengths as well as control the electric near field distribution. I observed the polarization anisotropy of large diameter NCs as demonstrated in polarized extinction spectra with behavior similar to that observed for much smaller NCs (Fig. 5.5).[6] In Figure

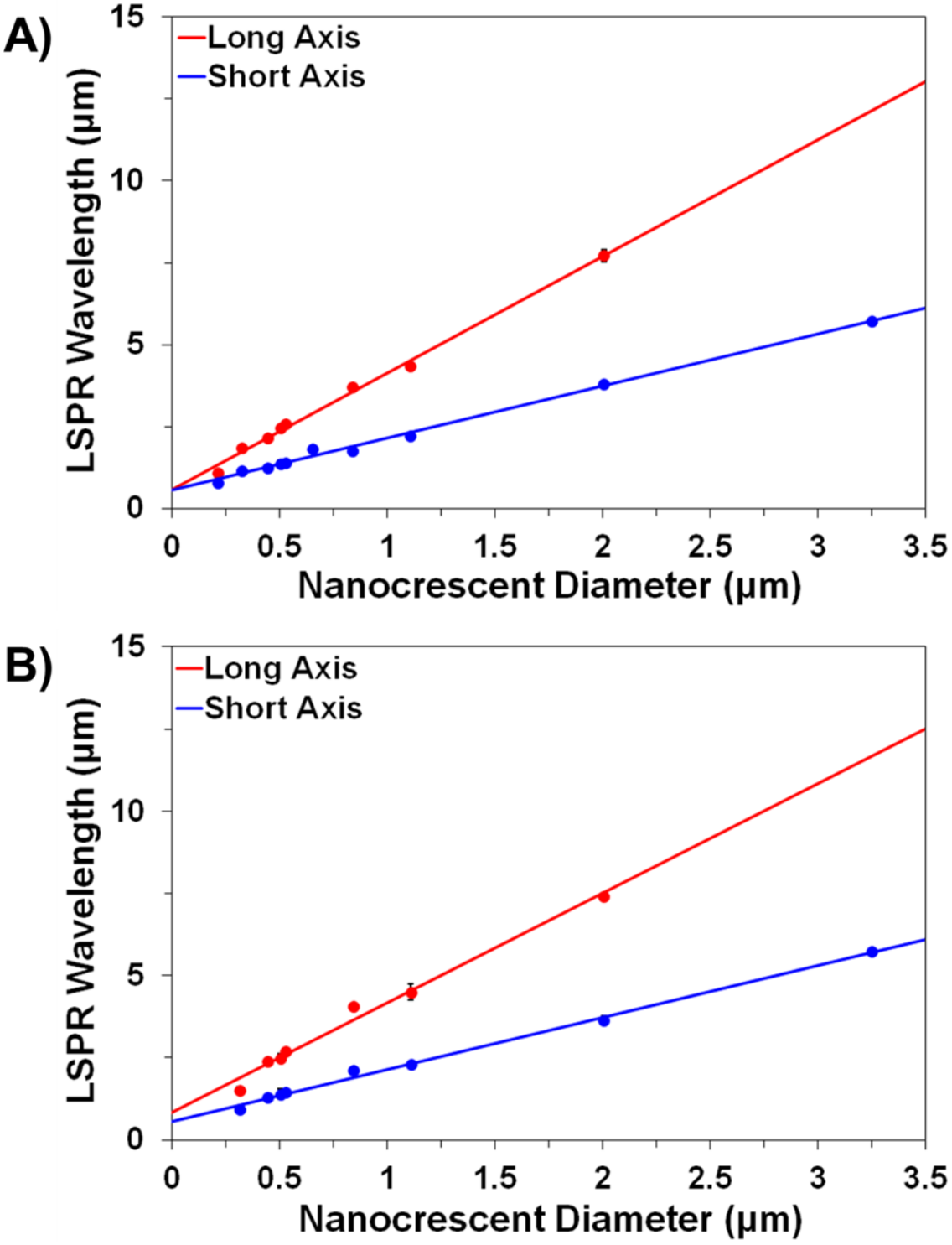

Figure 5.4. Relationship of plasmon resonance wavelength and nanocrescent diameter. Polarization-dependent plasmon resonance modes for AuNCs (A) and AgNCs (B) over a broad size range demonstrate a high degree of LSPR wavelength tunability.

Table 5.1. LSPR Wavelengths of Long and Short Axis Dipole Resonance Modes of Large Diameter Gold and Silver Nanocrescents

Metal	Final NC Diameter (μm)	Backbone Width (nm)	Tip Radius (nm)	λ_{max} SA Dipole (μm)	λ_{max} LA Dipole (μm)
Au	1.10	365	50	2.28	4.58
Au	1.40	400	42	3.07	5.41
Au	2.05	470	45	3.84	7.68
Au	3.25	674	75	5.77	11.13[a]
Ag	1.10	330	50	2.41	4.47
Ag	2.00	425	30	3.78	7.48
Ag	2.01	470	55	3.88	6.87
Ag	3.13	650	43	5.75	10.82[a]

[a]Values calculated using linear relationship of nanocrescent diameter and plasmon resonance wavelength based on measured trends shown in Fig. 5.4.

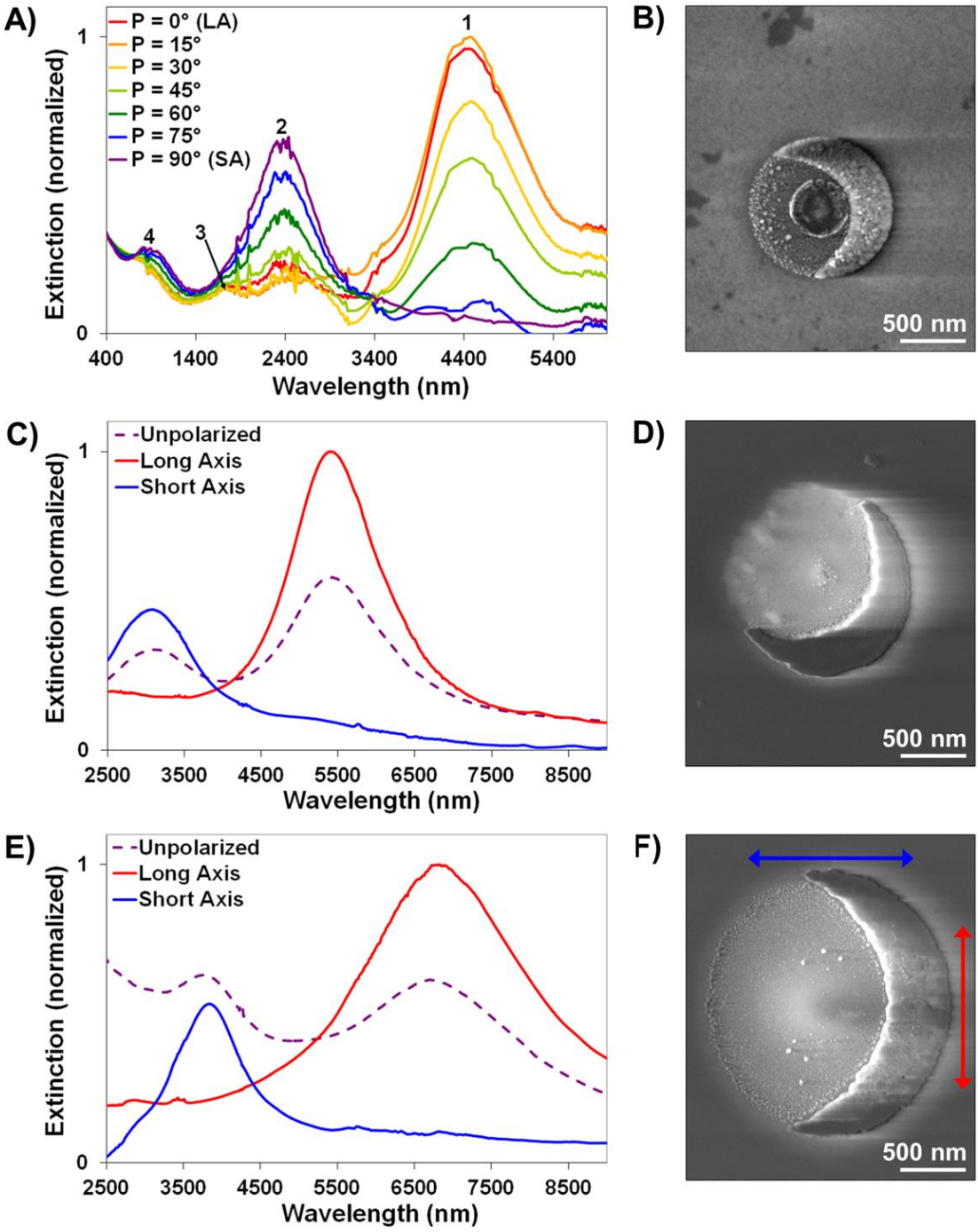

Figure 5.5. Extinction spectra and scanning electron microscopy images of large diameter AgNCs and AuNCs. Spectra of 1.10 μm final diameter AgNCs (A) measured at various polarization angles (P) demonstrating polarization anisotropy of the LSPR response of the plasmonic structure shown in B. Polarized extinction spectra with selectively induced long axis (red) and short axis (blue) dipole resonance modes and SEM images of 1.40 μm final diameter AuNCs (C and D, respectively) and 2.01 μm final diameter AgNCs (E and F, respectively). Arrows in F indicate polarization of electric field for LA (red) and SA (blue) resonance modes corresponding to colors in spectra.

5.5A, the extinction spectra of 1.10 μm diameter AgNCs are shown for several polarization angles. As the angle is increased from 0° (LA polarization) to 90° (SA polarization), distinct plasmon resonance modes observed over a visible to infrared spectral range are selectively induced. The characteristic anisotropic LSPR behavior is further established for large diameter NCs of both metals in the polarized spectra for 1.40 μm AuNCs and 2.01 μm AgNCs (Fig. 5.5B and C).

5.3.4 Aspect Ratios of Plasmonic Nanostructures

Large diameter plasmonic NCs have comparable structure lengths and LSPR wavelengths to nanorods, but with lower aspect ratios (length/width).[34] The effective length (L_{eff}) of the NCs can be estimated by calculating the circumference of the NC and subtracting the missing length (i.e., the distance between the two tips). For these open NC structures, the average gap angle is 90° so the effective length can be easily calculated by multiplying the final circumference measurement by a correction factor of 0.75 ((360°-90°)/360°). For 1.10 μm diameter AuNCs, this results in an L_{eff} of 2.63 μm, comparable in length to the 2.55 μm long gold nanorods.[34] However, the resulting aspect ratio (L_{eff}/backbone width) and LA-D resonance wavelength for this size AuNC of 7.2 and 4.58 μm, respectively, are lower than the nanorod values of 42.5 and ~10 μm, respectively. In order to target plasmon resonance wavelengths in the same range, the AuNC diameter needs to be increased to 3.25 μm with an L_{eff} of 7.65 μm, aspect ratio of 11.4, and calculated LA-D resonance wavelength of 11.1 μm. From this comparison, we can predict that even longer LSPR wavelengths can be reached with plasmonic NCs by continued increase of the diameter (length) and reduction of the backbone width. This will provide much higher aspect ratios.

5.3.5 Surface-Enhanced Spectroscopy Using Mid-IR Plasmon Resonances

The application of nanocrescents as surface enhancing substrates was investigated using sum frequency generation (SFG) spectroscopy. The wavelength of the LA-D resonance mode of AgNCs was tuned to overlap with the wavelength of one input photon as well as a targeted molecular vibration. The extinction spectrum of 2.05 μm diameter AgNCs produced a broad resonance peak centered at 6680 nm (Fig. 5.6A). This plasmon resonance mode was used to enhance the intensity of a 6.2 μm infrared beam used in the SFG spectroscopy setup and overlapped with the carbonyl stretch of 4-mercaptobenzoic acid at ~6 μm. The SFG spectrum in Figure 5.6B demonstrates the successful plasmonic enhancement of the input photon energy with a signal enhancement factor of 1.6. Coupling the wavelength of the laser to a tuned plasmonic resonance increased the intensity of the input photons and reduced the high intensity requirement of SFG.

5.4 Conclusion

The extension of multiple polarization-dependent localized surface plasmon resonance modes in AuNCs and AgNCs into the infrared spectral region has been demonstrated for large, micron size structures with LSPR wavelengths observed experimentally at ~8 μm and predicted up to 11.1 μm. Not only do NCs support plasmonic resonances over a broad visible to infrared range, but the structures maintain polarization dependence for truly selective control over light-structure interactions in specific spectral regions. Tailoring of the optical response could be further utilized to control the spatial distribution of the near field. A single nanocrescent optical antenna can be selectively tuned to exhibit multiple plasmon resonances at distinct wavelengths and

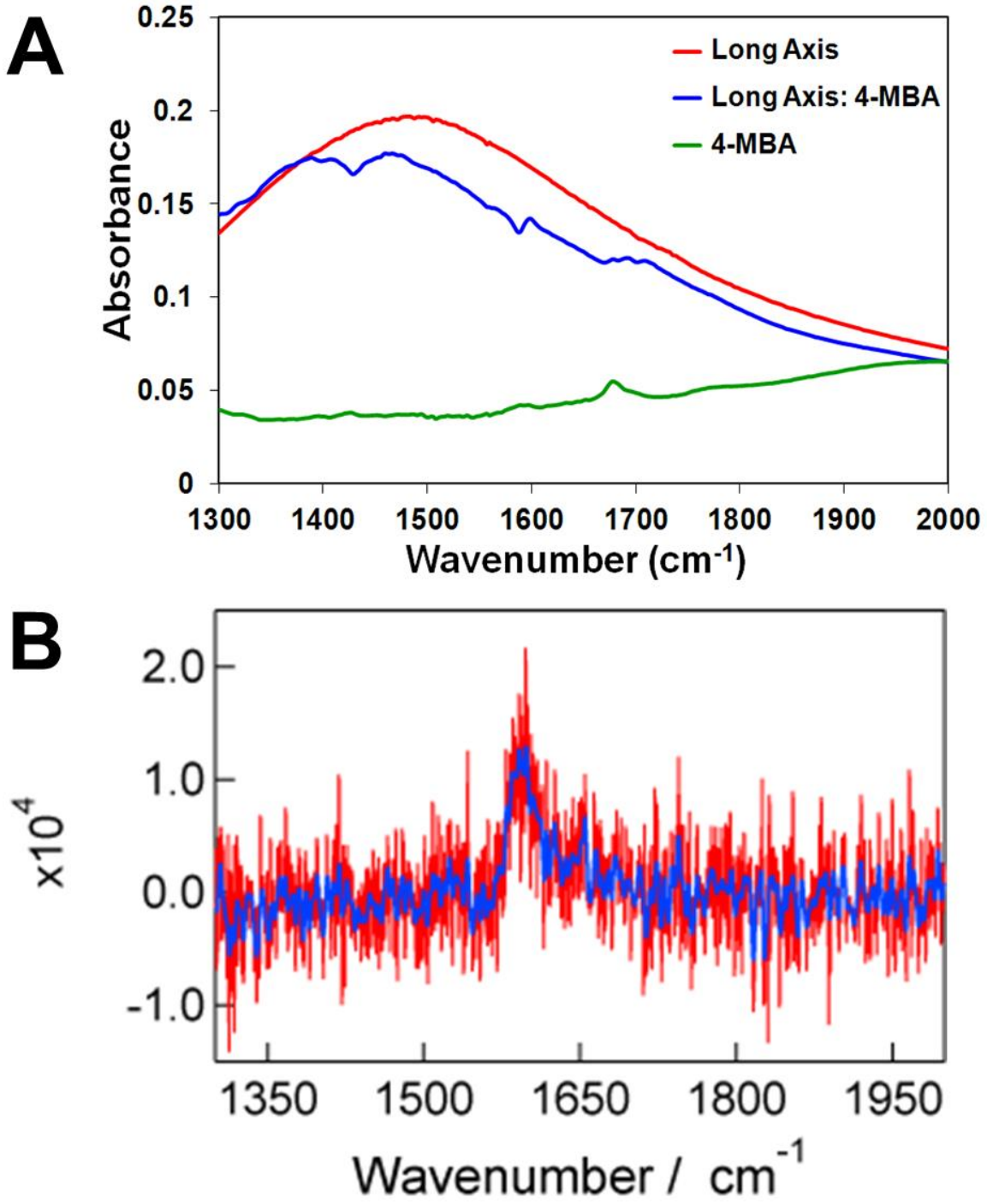

Figure 5.6. Plasmonic enhancement of mid-infrared sum frequency generation signal. A) FTIR absorbance spectrum (red) of 2.05 μm diameter AgNCs with broad LA-D resonance mode at 6680 nm (~1500 cm^{-1}). The absorption spectra of 4-mercaptobenzoic acid (4-MBA) and 4-MBA-functionalized AgNCs are shown in green and blue, respectively. B) Sum frequency generation spectrum of enhanced signal from 4-MBA carbonyl stretch at ~1600 cm^{-1} (red). Blue spectrum obtained after application of noise reduction algorithm.

the extension into the IR increases the applicable range of plasmonic NCs for manipulation of radiation and spectroscopic signal enhancement for applications such as surface enhanced infrared absorption spectroscopy (SEIRA) and sum frequency generation (SFG).

The critical size and wavelength at which the nanocrescent structure no longer supports LSPR behavior is beyond the capability of the current experimental setup and further investigations into the maximum size for continued LSPR behavior of these structures will continue using substrates with wider ranging optical windows.

5.5 References

1. Alvarez-Puebla, R.; Liz-Marzán, L. M.; García de Abajo, F. J. Light Concentration at the Nanometer Scale. *J. Phys. Chem. Lett.* **2010,** *1,* 2428-2434.

2. Duan, H.; Fernández-Domínguez, A. I.; Bosman, M.; Maier, S. A.; Yang, J. K. W. Nanoplasmonics: Classical down to the Nanometer Scale. *Nano Lett.* **2012,** *12,* 1683-1689.

3. Li, M.; Cushing, S., K.; Zhang, J.; Lankford, J.; Aguilar, Z. P.; Ma, D.; Wu, N. Shape-Dependent Surface-Enhanced Raman Scattering in Gold-Raman-Probe-Silica Sandwiched Nanoparticles for Biocompatible Applications. *Nanotechnology*. **2012,** *23,* 115501.

4. Cai, Y.; Li, Y.; Nordlander, P.; Cremer, P. S. Fabrication of Elliptical Nanorings with Highly Tunable and Multiple Plasmonic Resonances. *Nano Lett.* **2012,** *12,* 4881-4888.

5. Bochenkov, V. E.; Sutherland, D. S. From Rings to Crescents: A Novel Fabrication Technique Uncovers the Transition Details. *Nano Lett.* **2013,** *13,* 1216-1220.

6. Cooper, C. T.; Rodriguez, M.; Blair, S.; Shumaker-Parry, J. S. Polarization Anisotropy of Multiple Localized Plasmon Resonance Modes in Noble Metal Nanocrescents. *J. Phys. Chem. C.* **2014,** *118,* 1167-1173.

7. Le Ru, E. C.; Meyer, M.; Etchegoin, P. G. Proof of Single-Molecule Sensitivity in Surface Enhanced Raman Scattering (SERS) by Means of a Two-Analyte Technique. *J. Phys. Chem. B.* **2006,** *110,* 1944-1948.

8. Banik, M.; Nag, A.; El-Khoury, P. Z.; Rodriguez Perez, A.; Guarrotxena, N.; Bazan, G. C.; Apkarian, V. A. Surface-Enhanced Raman Scattering of a Single Nanodumbbell: Dibenzyldithio-Linked Silver Nanospheres. *J. Phys. Chem. C.* **2012,** *116,* 10415-10423.

9. Aouani, H.; Rahmani, M.; Šípová, H.; Torres, V.; Hegnerová, K.; Beruete, M.; Homola, J.; Hong, M.; Navarro-Cía, M.; Maier, S. A. Plasmonic Nanoantennas for Multispectral Surface-Enhanced Spectroscopies. *J. Phys. Chem. C.* **2013,** *117,* 18620-18626.

10. Willets, K. A. Super-Resolution Imaging of Interactions Between Molecules and Plasmonic Nanostructures. *Phys. Chem. Chem. Phys.* **2013,** *15,* 5345-5354.

11. Rang, M.; Jones, A.; Zhou, F.; Li, Z. -Y.; Wiley, B.; Xia, Y.; Raschke, M. Optical Near-Field Mapping of Plasmonic Nanoprisms. *Nano Lett.* **2008,** *8,* 3357-3363.

12. Berweger, S.; Atkin, J. M.; Olmon, R. L.; Raschke, M. B. Adiabatic Tip-Plasmon Focusing for Nano-Raman Spectroscopy. *J. Phys. Chem. Lett.* **2010,** *1,* 3427-3432.

13. Fontana, J.; Livenere, J.; Bezares, F. J.; Caldwell, J. D.; Rendell, R.; Ratna, B. R. Large Surface-Enhanced Raman Scattering from Self-Assembled Gold Nanosphere Monolayers. *Appl. Phys. Lett.* **2013,** *102,* 201606.

14. Aroca, R. F.; Alvarez-Puebla, R. A.; Pieczonka, N.; Sanchez-Cortez, S.; Garcia-Ramos, J. V. Surface-Enhanced Raman Scattering on Colloidal Nanostructures. *Adv. Colloid Interface Sci.* **2005,** *116,* 45-61.

15. Johansson, P.; Xu, H.; Käll, M. Surface-Enhanced Raman Scattering and Fluorescence Near Metal Nanoparticles. *Phys. Rev. B.* **2005,** *72,* 035427.

16. Jonsson, G. E.; Fredriksson, H.; Sellappan, R.; Chakarov, D. Nanostructures for Enhanced Light Absorption in Solar Energy Devices. *Int. J. Photoenergy*. **2011,** 939807.

17. Mammo, E. D.; Marques-Hueso, J.; Richards, B. S. In *Nanoplasmonics for Photovoltaic Applications*, Proceedings of the International Society for Optics and Photonics (SPIE), Photonics for Solar Energy Systems IV, 84381M (June 1, 2012); doi:10.1117/12.922646.

18. Stanley, R. Plasmonics in the Mid-Infrared. *Nat. Photon.* **2012,** *6,* 409-411.

19. Coe, J. V.; Rodriguez, K. R.; Teeters-Kennedy, S.; Cilwa, K.; Heer, J.; Tian, H.; Williams, S. M. Metal Films with Arrays of Tiny Holes: Spectroscopy with Infrared Plasmonic Scaffolding. *J. Phys. Chem. C.* **2007,** *111,* 17459-17472.

20. Biswas, A.; Eilers, H.; Hidden, F.; Aktas, O. C.; Kiran, C. V. S. Large Broadband Visible to Infrared Plasmonic Absorption from Ag Nanoparticles with a Fractal Structure Embedded in a Teflon AF® Matrix. *Appl. Phys. Lett.* **2006,** *88,* 013103.

21. Enders, D.; Nagao, T.; Pucci, A.; Nakayama, T.; Aono, M. Surface-Enhanced ATR-IR Spectroscopy with Interface-Grown Plasmonic Gold-Island Films Near the Percolation Threshold. *Phys. Chem. Chem. Phys.* **2011,** *13,* 4935-4941.

22. Le, F.; Brandl, D. W.; Urzhumov, Y. A.; Wang, H.; Kundu, J.; Halas, N. J.; Aizpurua, J.; Nordlander, P. Metallic Nanoparticle Arrays: A Common Substrate for Both Surface-Enhanced Raman Scattering and Surface-Enhanced Infrared Absorption. *ACS Nano.* **2008,** *2,* 707-718.

23. Blanchard, R.; Boriskina, S. V.; Genevet, P.; Kats, M. A.; Tetienne, J.-P.; Yu, N.; Scully, M. O.; Dal Negro, L.; Capasso, F. Multi-Wavelength Mid-Infrared Plasmonic Antennas with Single Nanoscale Focal Point. *Opt. Express.* **2011,** *19,* 22113-22124.

24. Wang, T.; Nguyen, V. H.; Buchenauer, A.; Schnakenberg, U.; Taubner, T. Surface Enhanced Infrared Spectroscopy with Gold Strip Gratings. *Opt. Express.* **2013,** *21,* 9005-9010.

25. Link, S.; El-Sayed, M. A. Size and Temperature Dependence of the Plasmon Absorption of Colloidal Gold Nanoparticles. *J. Phys. Chem. B.* **1999,** *103,* 4212-4217.

26. Burda, C.; Chen, X.; Narayanan, R.; El-Sayed, M. A. Chemistry and Properties of Nanocrystals of Different Shapes. *Chem. Rev.* **2005,** *105,* 1025-1102.

27. Aksu, S.; Yanik, A. A.; Adato, R.; Artar, A.; Huang, M.; Altug, H. High-Throughput Nanofabrication of Infrared Plasmonic Nanoantenna Arrays for Vibrational Nanospectroscopy. *Nano Lett.* **2010,** *10,* 2511-2518.

28. Weber, D.; Albella, P.; Alonso-González, P.; Neubrech, F.; Gui, H.; Nagao, T.; Hillenbrand, R.; Aizpurua, J.; Pucci, A. Longitudinal and Transverse Coupling in Infrared Gold Nanoantenna Arrays: Long Range Versus Short Range Interaction Regimes. *Opt. Express.* **2011,** *19,* 15047-15061.

29. Haes, A. J.; Zou, S.; Schatz, G. C.; Van Duyne, R. P. Nanoscale Optical Biosensor: Short Range Distance Dependence of the Localized Surface Plasmon Resonance of Noble Metal Nanoparticles. *J. Phys. Chem. B.* **2004,** *108,* 6961-6968.

30. Bukasov, R.; Shumaker-Parry, J. S. Highly Tunable Infrared Extinction Properties of Gold Nanocrescents. *Nano Lett.* **2007,** *7,* 1113-1118.

31. Neubrech, F.; Pucci, A.; Cornelius, T. W.; Karim, S.; García-Etxarri, A.; Aizpurua, J. Resonant Plasmonic and Vibrational Coupling in a Tailored Nanoantenna for Infrared Detection. *Phys. Rev. Lett.* **2008,** *101,* 157403.

32. Hu, H.; Duan, H.; Yang, J. K. W.; Shen, Z. X. Plasmon-Modulated Photoluminescence of Individual Gold Nanostructures. *ACS Nano.* **2012,** *6,* 10147-10155.

33. Kelly, K. L.; Coronado, E.; Zhao, L. L.; Schatz, G. C. The Optical Properties of Metal Nanoparticles: The Influence of Size, Shape, and Dielectric Environment. *J. Phys. Chem. B.* **2002,** *107,* 668-677.

34. Neubrech, F.; Weber, D.; Lovrincic, R.; Pucci, A.; Lopes, M.; Toury, T.; De La Chapelle, M. L. Resonances of Individual Lithographic Gold Nanowires in the Infrared. *Appl. Phys. Lett.* **2008,** *93,* 163105.

35. Cooper, C. T.; Rodriguez, M.; Blair, S.; Shumaker-Parry, J. S. Polarization-Dependent Mid-IR Localized Plasmon Resonances of Gold and Silver Nanocrescents. *Nanoscale.* **2014.** (Submitted).

36. Bukasov, R.; Shumaker-Parry, J. S. Silver Nanocrescents with Infrared Plasmonic Properties as Tunable Substrates for Surface Enhanced Infrared Absorption Spectroscopy. *Anal. Chem.* **2009,** *81,* 4531-4535.

37. Han, Y.; Raghunathan, V.; Feng, R. -R.; Maekawa, H.; Chung, C. -Y.; Feng, Y.; Potma, E. O.; Ge, N. -H. Mapping Molecular Orientation with Phase Sensitive Vibrationally Resonant Sum-Frequency Generation Microscopy. *J. Phys. Chem. B.* **2013,** *117,* 6149-6156.

38. Fischer, J.; Vogel, N.; Mohammadi, R.; Butt, H. -J.; Landfester, K.; Weiss, C. K.; Kreiter, M. Plasmon Hybridization and Strong Near-Field Enhancements in Opposing Nanocrescent Dimers with Tunable Resonances. *Nanoscale.* **2011,** *3,* 4788-4797.

39. Bukasov, R.; Ali, T. A.; Nordlander, P.; Shumaker-Parry, J. S. Probing the Plasmonic Near-Field of Gold Nanocrescent Antennas. *ACS Nano.* **2010,** *4,* 6639-6650.

40. Unger, A.; Rietzler, U.; Berger, R.; Kreiter, M. Sensitivity of Crescent-Shaped Metal Nanoparticles to Attachment of Dielectric Colloids. *Nano Lett.* **2009,** *9,* 2311-2315.

41. Shumaker-Parry, J. S.; Rochholz, H.; Kreiter, M. Fabrication of Crescent-Shaped Optical Antennas. *Adv. Mater.* **2005,** *17,* 2131-2134.

CHAPTER 6

CONCLUSION AND FUTURE WORK

6.1 Conclusion

The optical properties of plasmonic gold and silver nanocrescents over a broad size range have been investigated for application as surface enhanced spectroscopy and microscopy substrates. The multimodality, tunability of LSPR wavelengths, high enhancement factor, and polarization anisotropy of the structure combine to make the nanocrescent an ideal substrate for optical applications across a broad spectral range.

The organization of nanosphere templates for higher densities and specific arrangement of nanostructures has improved the fabrication process. Control over the templating process provides a way to more systematically investigate optical properties of plasmonic crescents and their correlation with the physical structure. For example, close packing of templates followed by oxygen plasma size reduction allows for investigation of similar size structures with varying interparticle distances and vice versa. This technique was used to fabricate nanocrescent arrays with higher throughput and greater control over surface density. The capability to organize structures has implications for investigating interparticle interactions such as plasmonic coupling.

Noble metal nanocrescents have demonstrated multiple polarization-dependent plasmon resonance modes. Each mode corresponds to a unique electron oscillation across a specific axis of the structure that can be selectively induced by controlling the

polarization of the incident electric field. This feature allows for far field manipulation of electric near field distribution across the particle surface and can be used to reduce probe volumes to nanoscale dimensions. The anisotropy of the nanocrescent has been calculated using finite-element methods and established across a visible to infrared spectral range with polarized extinction spectra. The selective induction of long axis dipole and quadrupole resonance modes as well as a short axis dipole resonance mode has been shown from 500 nm up to 8 μm with the addition of two previously unobserved polarization-dependent resonance modes. The unique near field distributions resulting from these various resonance modes can be used to localize electric near fields which provides knowledge about the location of analyte molecules and increases the specificity of techniques with high spatial resolution.

Both gold and silver nanocrescents have exhibited polarization-dependent plasmon resonance modes that extend into the mid-infrared spectral range. The asymmetry and high aspect ratio of the crescent structure allow for higher order resonance modes and continued nanoscale LSPR behavior at microscale dimensions. This is a significant and highly advantageous characteristic as few nanostructures maintain IR-active plasmonic behavior for extension into the infrared region. Plasmonic nanoparticles that continue to demonstrate plasmonic properties can be utilized to improve techniques such as infrared absorption spectroscopy, thermal imaging, and nonlinear optical processes.

6.2 Future Work

The incorporation of plasmonic nanocrescents as surface enhancing substrates into analytical techniques has just begun. Preliminary results for enhancement of nonlinear optical microscopy and spectroscopy techniques confirm that these structures can

successfully improve analytical signals, but these processes can be optimized to a greater degree. Further perfection of the fabrication process and template patterning leading to more well-defined near field localization as well as continued broadening of applicable plasmon resonance wavelength ranges will improve the resolution and sensitivity that can be achieved using these structures as enhancing substrates.